https://ntrs.nasa.gov/search.jsp?R=19830005116 2020-03-21T05:06:37+00:00Z

NASA
CR
3622
c.1

LOAN COPY: RETURN TO AFWL
TECHNICAL LIBRARY, KIRTLAND

0062187

TECH LIBRARY KAFB, NM

NASA Contractor Report 3622

Turbulence Effect on Crossflow Around a Circular Cylinder at Subcritical Reynolds Numbers

Willy Z. Sadeh and Daniel B. Saharon

GRANT NSG-3127
NOVEMBER 1982

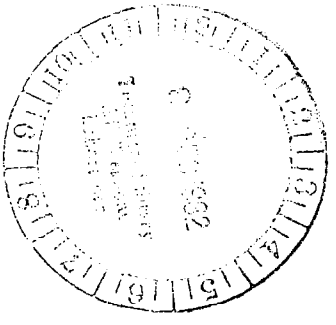

NASA

NASA Contractor Report 3622

Turbulence Effect on Crossflow Around a Circular Cylinder at Subcritical Reynolds Numbers

Willy Z. Sadeh and Daniel B. Saharon
Colorado State University
Fort Collins, Colorado

Prepared for
Lewis Research Center
under Grant NSG-3127

National Aeronautics
and Space Administration

**Scientific and Technical
Information Branch**

1982

TECH LIBRARY KAFB, NM
0062187

TABLE OF CONTENTS

TURBULENCE EFFECT ON CROSSFLOW AROUND A CIRCULAR CYLINDER AT SUBCRITICAL REYNOLDS NUMBERS

by Willy Z. Sadeh[1] and Daniel B. Saharon[2]
Colorado State University, Fort Collins, Colorado

SUMMARY

An investigation of the effect of freestream turbulence on the flow around a smooth circular cylinder at subcritical Reynolds numbers from 5.2×10^4 to 2.09×10^5 was conducted. Measurements show that the interaction of incident turbulence with the initial laminar boundary layer: (1) modifies the characteristics of the mean surface pressure distribution; (2) induces an aft shift in the separation point ranging from 5 to 50° beyond the laminar separation angle of 80°; and, (3) reduces the mean drag coefficient to values between 97 and 46% of its nearly constant laminar counterpart. The extent of these changes depends on the particular Reynolds number-background turbulence combination. These results demonstrate that a boundary-layer flow similar to that found in critical, supercritical and/or transcritical flow regimes is induced by turbulence at subcritical Reynolds numbers and, hence, the effect of turbulence is equivalent to an effective increase in the Reynolds number. The change in the nature and properties of the boundary layer in the subcritical regime, consequent upon the penetration of turbulence into it, is in agreement with the model proposed by the vorticity-amplification theory.

---

[1]Professor of Engineering and Fluid Mechanics, Department of Civil Engineering
[2]Research Assistant, ibid.

1. INTRODUCTION

The effect of freestream turbulence in crossflow about a circular cylinder in delaying the separation and in reducing its drag at subcritical Reynolds numbers has long been recognized. This effect was first reported by Fage & Warsap in 1929 (ref. 1) and by Fage & Falkner in 1931 (ref. 2) in their pioneering experimental investigations and subsequently was verified in numerous other studies (see, e.g., ref. 3). Fage & Warsap (ref. 1) found that the drag coefficient of a smooth circular cylinder decreases when freestream turbulence is superimposed by means of an upwind square-mesh rope netting. They further found out that the reduction in the drag coefficient at a given Reynolds number was higher as the rope netting was positioned closer to the circular cylinder. Soon thereafter, Fage & Falkner (ref. 2), using a similar experimental setup in the same wind tunnel and at the same subcritical Reynolds numbers, reproduced the drag reduction reported in ref. 1 and found, in addition, that turbulence in the incident stream effects a delay in the separation angle.

No information on the intensity and properties of the incident turbulence, and on the surface roughness of the circular cylinder are given in these two papers. Moreover, no explanation concerning the mechanism responsible for the interaction of the oncoming turbulence with the cylinder boundary layer and the resulting separation delay and drag reduction was proposed in either study. To date, as a matter of fact, a theory that addresses the role of freestream turbulence in affecting the separation on and the drag coefficient of a circular cylinder at subcritical Reynolds numbers has yet to be advanced. The objective of the present investigation was to demonstrate that the vorticity-amplification theory offers a satisfactory explanation and proposes a suitable physical model for these effects of freestream turbulence. This theory is not reviewed here since the background literature is readily accessible (refs. 4,5,6). A summary of its basic physical ideas is, however, given below in order to point out the guidelines applied in conducting this investigation.

The vorticity-amplification theory suggests that freestream turbulence, no matter how small initially, experiences significant amplification as it is conveyed by the mean flow toward the stagnation zone of a circular cylinder. This turbulence amplification is governed by the stretching and accompanying streamwise biased tilting of cross-vortex tubes which are induced by the flow divergence around the circular cylinder. The volume and angular momentum of each cross-vortex tube are conserved throughout its stretching and tilting provided that viscous dissipation is neglected.

As a result, the scale of the tube decreases, its angular velocity (or vorticity) increases, the streamwise turbulent velocity amplifies and turbulent kinetic energy accumulates within each stretched cross-vortex tube. A fundamental tenet of the vorticity-amplification theory is that the amplification occurs at scales larger than the neutral scale of the stagnation flow. At scales smaller than this neutral scale, the turbulence dissipates more rapidly than it amplifies due to the viscous action.

The emergence of a coherent substructure near the stagnation zone of the body is the outcome of the stretching process and the preferred amplification of turbulence. This coherent substructure consists of a regular array of standing cross-vortex tubes of approximately equal scales distributed spanwise and with their cores outside the circular cylinder boundary layer (ref. 6). Turbulent kinetic energy accumulates within the cells of this organized substructure which represents, in fact, an array of energy-containing eddies. Most of the turbulence amplification transpires at a most amplified scale characteristic of this coherent substructure which is generally greater than but commensurate with the thickness of the boundary layer. Discrete vortices (or eddies) are continuously drawn out from this coherent substructure and swept downstream by the mean flow around the body. These highly energetic eddies penetrate into the prevailing boundary layer, energize it and render it partially or even fully turbulent if it was initially laminar (ref. 6) or enhance the turbulence within it. In the case of an initial laminar boundary layer on a smooth circular cylinder at subcritical Reynolds numbers, the change in its nature necessarily fosters retardation of the separation and reduction of the drag.

This investigation focused on examining the effectiveness of freestream turbulence in modifying the surface pressure distribution, in delaying the separation on and in diminishing the drag coefficient of a smooth circular cylinder in crossflow at subcritical cylinder-diameter Reynolds numbers ranging from about 5.2×10^4 to 2.09×10^5. In order to assess the extent to which the pressure distribution, the separation angle and drag coefficient are affected by freestream turbulence, they were first measured in smooth (or laminar) incident flow. Freestream turbulence susceptible to experiencing amplification owing to the stretching mechanism was subsequently produced in a controlled fashion using an appropriate turbulence-generating grid. Finally, both the separation angle and the drag coefficient were determined from the surface pressure distribution for a variety of turbulent incident flow conditions.

2. EXPERIMENTAL ARRANGEMENT

2.1 Wind Tunnel

The experimental investigation reported herein was conducted in a low-speed closed-circuit single-return wind tunnel at the Fluid Dynamics and Diffusion Laboratory, Colorado State University. This wind tunnel has a 183 cm (6 ft) square cross section, a test section 27 m (88 ft) long and a contraction ratio of 9:1. The side panels and parts of the ceiling of the test section are made of high quality tempered glass and/or Plexiglas to facilitate flow visualization. Stable airspeeds up to about 36 m/s (120 ft/s) are generated by a 4-blade propeller driven by a 400 hp DC motor. Continuous variation of the airspeed is achieved by adjusting the pitch of the propeller blades and/or its motor speed. The freestream velocities corresponding to the cylinder-diameter Reynolds-number range of interest were adjustable with a resolution better than 5%. At the same time, the wind-tunnel turbulence intensity in an empty test section was about 0.4 to 0.45% within this freestream velocity range. The wind tunnel is equipped with a computer-operated triaxial motorized traversing mechanism that was used to position any measuring probe with a resolution of about 6.4 μm (0.25 mils).

2.2 Circular Cylinder

A circular cylinder 15.88 cm (6-1/4 in) in diameter D and 183 cm (6 ft) long made of light aluminum alloy was used. This cylinder was machined from a seamless pipe and consisted of three sections, one 51 cm (20 in) long and two each 66 cm (26 in) in length. In assembling these three sections together, all the joints were tightly sealed with silicone grease. After joining the three sections, the cylinder was rounded to within 0.50 mm (20 mils) and, subsequently, it was sandblasted, polished and, finally, coated with dead-black lacquer (3M Co., Nextel Velvet Coating, Series 101-C10). A uniform coating was ensured by wet spraying the paint while rotating the cylinder at constant rpm by means of a lathe. After the film dried, the cylinder was buffed to produce a smooth surface with a grainless finish of high luster. The final thickness of the coating was about 76 μm (3 mils) with an average roughness height $k = 2.5$ μm (0.1 mils) according to the specifications supplied by the manufacturer. An extremely smooth surface with a relative surface roughness k/D of about 1.6×10^{-5} was thus obtained. A sketch of the circular cylinder, in which the two systems of coordinates used-viz., Cartesian and polar- are shown, is displayed in Fig. 2.1. Note that the origin of the Cartesian system of coordinates is at the cylinder stagnation point while that of the polar system of coordinates is at the

cylinder center. The blockage coefficient, which is given by the ratio of the cylinder diameter D to the height h (or width) of the wind-tunnel square cross section D/h, was 0.087. This is also the cylinder diameter-to-span ratio (or slenderness) D/S of this cylinder since its span (or length) S was equal to the height (or width) of the wind-tunnel cross section.

The diameter of the circular cylinder was selected in order to secure a relatively thick stagnation-point laminar boundary layer at the subcritical Reynolds numbers of interest. In this case, the thickness δ_ℓ of the laminar boundary layer at the cylinder stagnation point is given by (ref. 5)

$$\delta_\ell = 1.2D/Re^{\frac{1}{2}} , \qquad (2.1)$$

in which Re designates the cylinder-diameter Reynolds number based on the freestream velocity. Within the subcritical Reynolds-number range from 5.2×10^4 to 2.09×10^5, the thickness of the stagnation-point laminar boundary layer varies from about 0.84 to 0.42 mm (33 to 16 mils). Thickening of the theoretical laminar boundary layer along the cylinder circumference was estimated by means of the Blasius power-series method (ref. 7, pp. 168-173) up to a peripheral angle $\theta = 80°$ (measured from the cylinder stagnation point). The thickness of the theoretical laminar boundary layer at this angle ranges from 1.38 to 0.69 mm (55 to 27 mils) with increasing Reynolds numbers from 5.2×10^4 to 2.09×10^5.

A total of 130 pressure taps 1.6 mm (1/16 in) in diameter were drilled along the midsection of the cylinder that extended over a length of 86.40 cm (34 in), viz, from z = 43.20 to 43.20 cm. They were positioned as follows: (a) on the upwind face along the cylinder axis in the planes z = 0, ±7.60, ±15.20, ±22.80, ±30.40 and ±43.20 cm (0, ±3, ±6, ±9, ±12 and ±17 in); (b) along the cylinder circumference at intervals of 5° from $\theta = 0$ to 30°, of 10° from $\theta = 40$ to 100° and of 20° from $\theta = 120$ to 180° in the planes z = 0, ±7.60, ±15.20, +30.40 and +43.20 cm (0, ±3, ±6, +12 and +17 in). Their distribution is portrayed in Fig. 2.1. Plastic Tygon tubing 1.6 mm (1/16 in) I.D. was utilized to connect the pressure ports to a scanning valve.

The cylinder was installed across the wind-tunnel width 23 m (75 ft) downstream of the test-section entrance with its axis 61 cm (2 ft) above the wind-tunnel floor (at 1/3 of the height of the wind-tunnel cross section). This positioning of the cylinder was selected to facilitate its mounting and the flow probing. At this station, the cylinder was exposed to uniform crossflow since the thickness of

the boundary layer along the wind-tunnel floor varied from about 38 to 28 cm (15 to 11 in) within the Reynolds-number range of interest.

The cylinder was mounted by means of collars attached to two supporting endplates (or flanges) as shown in Fig. 2.1 which, in turn, were fastened to the wind-tunnel walls. Each endplate-collar assembly was 9.2 cm (3.62 in) wide. Gaps between the supporting flanges and the wind-tunnel walls were tightly sealed with tape to prevent leakage of high pressure air from the stagnation zone into the near wake. All the pressure tubes were ducted through several holes in one of the end plate-collar assembly. These holes were sealed without constricting the tubes passing through them. The cylinder could be continuously rotated inside its collar by means of a manually operated rotation compound. Angular positioning of any pressure tap was possible with an accuracy of 0.5°.

2.3 Turbulence-Generating Grid

Production of freestream turbulence (or vorticity) in a controlled manner was achieved using a mobile, special purpose turbulence-generating grid. This grid consisted of 24 vertical finely polished aluminum rods that spanned the height of the wind-tunnel cross section. Each rod was 1.27 cm (1/2 in) in diameter d and the mesh M (center-to-center interval between two rods) was adjustable. A mesh M = 6.35 cm (2-1/2 in) was used in this experiment and, hence, the open spacing between two rods was 5 cm (2 in). In terms of the cylinder diameter D, the mesh and the open spacing were 0.40 and 0.31D, respectively.

This mesh was selected in order to obtain a grid geometric solidity within the stable range. The geometric solidity (or blockage) σ is defined as the ratio of the projected solid area of the grid to its total area. Then the solidity of the present grid reduces to the ratio of the rod diameter to the mesh-i.e., $\sigma = d/M$-and its value was 0.20. This solidity is much below the unstable range which generally occurs for solidities greater than about 0.34 to 0.37 (refs. 8 (pp. 530-532),9,10). Reasonable lateral homogeneity in both mean velocity and streamwise turbulence intensity was obtained as a result of this stable solidity (ref. 11).

The vertical orientation of the rods was chosen specifically to produce vorticity primarily in the direction perpendicular to the axis of the cylinder (y-direction) with turbulent velocity fluctuations in the streamwise direction (x-direction). This cross vorticity and its associated streamwise turbulent velocity are those components of

a general three-dimensional field most susceptible to undergoing amplification due to stretching in this flow situation. Anisotropic turbulence was thus deliberately generated in order to exploit the stretching mechanism of this crossflow about a cylinder.

The rod diameter was selected in order to ensure production of turbulence at scales much larger than the neutral scale of this stagnation flow about a circular cylinder in view of the selective amplification of turbulence at these scales. For this stagnation flow, the neutral wavelength λ_0 is given by (ref. 5)

$$\lambda_0 = \pi D/Re^{\frac{1}{2}} , \qquad (2.2)$$

and it decreases from 2.19 to 1.09 mm (0.09 to 0.04 in) with increasing cylinder-diameter Reynolds number from 5.2×10^4 to 2.09×10^5. Within this range of the cylinder-diameter Reynolds number, the Reynolds number of each rod of the grid, based on the rod diameter and the freestream velocity upwind of the grid, varied from 4000 to 17000. The Strouhal number S is about 0.21 at these rod Reynolds numbers (ref. 12). Most of the turbulent energy was consequently concentrated at a Strouhal scale $\lambda_s = d/S$ of about 60.50 mm (2.38 in) estimated under the frozen-pattern assumption (ref. 13). It should be noted that the Strouhal scale is independent of the velocity when the Strouhal number remains constant with increasing rod Reynolds number as in this case. Turbulence was thus mainly produced at a scale about 28 to 56 times larger than the neutral scale depending upon the particular cylinder-diameter Reynolds number. The turbulence-generating grid therefore met the necessary criteria for producing the desired freestream turbulence.

This experiment was carried out with the turbulence-generating grid installed at three different distances upwind of the cylinder stagnation point, viz., at x_g = 63.50, 111.13 and 158.75 cm (25, 43-3/4, and 62-1/2 in). A schematic diagram of the experimental arrangement including all important dimensions, the turbulence-generating grid and the system of coordinates is displayed in Fig. 2.2. In addition, a still photograph of the test section showing the circular cylinder and the turbulence-generating grid mounted at a distance of 158.75 cm upstream of the cylinder is given in Fig. 2.3.

3. EXPERIMENTAL TECHNIQUE

3.1 Separation Line Visualization

Visualization of the separation line on the cylinder was conducted using a dry-surface coating method specifically developed for this purpose. This method is not restricted to any particular Reynolds-number range and it can be used for either laminar or turbulent incident flow. Furthermore, it supplies a clear permanent record of good photographic quality since the signature of the separation line is not affected by the removal of the airflow. This dry-surface coating technique relies on the color reaction of a pH indicator contained in a thin film with a suitable gas released into the recirculating flow within the cylinder wake. The outcome of this reaction is the formation of two sharply contrasting colored sections on the cylinder surface demarcated by a narrow transition band of several millimeters width whose centerline approximates the location of the separation line. In this experiment, Congo Red indicator and ammonia gas were employed. Then the coatings of the separated and attached flow regions became deep red and plain blue, respectively. The transition band between these two colored sections never exceeded a width of about 7 mm (276 mils) corresponding to an arc of 5°. Separation angles indicated by this visualization technique were within ±4% of their counterpart reduced from the mean wall pressure distribution. All the details of this dry-surface coating method including its reliability testing are described in ref. 14.

Color 16 mm movies were shot at a speed of 24 fps (frames per second) utilizing a Bolex H-16 SBM reflex camera with a governor-controlled spring motor (Paillard, S.A.). High-speed color reversal films (Kodak Ektachrome EF 7242) with exposure indexes of ASA 80 (20 DIN) in daylight and ASA 125 (22 DIN) for Tungsten lighting (3200 K) were employed. Lighting was supplied by floodlights and spotlights (Berkey Photo, Inc.) of fixed and variable focus equipped with built-in barn doors for generating light sheets. The composition and intensity of the lighting were adjusted in each flow situation to produce the needed illumination.

3.2 Freestream Conditions

In order to provide a standard in presenting the results for both smooth and turbulent incident flows, the cylinder-diameter Reynolds number is defined herein in terms of a reference freestream velocity U_∞. The latter is the uniform velocity upstream of the cylinder and upwind of the turbulence-generating grid when it is present. This

experimental investigation was carried out at subcritical cylinder-diameter Reynolds numbers ranging from 5.2×10^4 to 2.09×10^5 (air at 20°C (68°F), kinematic viscosity $\nu = 1.48 \times 10^{-5}$ m^2/s (1.59×10^{-4} ft^2/s)) as earlier mentioned. The uniform freestream velocity corresponding to this Reynolds-number range varied from 4.9 to 19.5 m/s (16 to 64 ft/s).

Continuous monitoring of the uniform freestream velocity was accomplished using a Pitot-static tube of modified Prandtl type 3.2 mm (1/8 in) in outside diameter with an impact orifice 0.80 mm (1/32 in) (United Sensor and Control Corp., Model PAC-12-KL). This Pitot-static tube, called hereinafter the reference tube, was installed along the wind-tunnel centerline 11.52 m (37.80 ft, 72.5D) upwind of the cylinder, as indicated in Fig. 2.2, and 1.22 m (4 ft) above the floor. The Reynolds number of this Pitot-static tube (based on its outside radius (1.6 mm (1/16 in)) varied from about 500 to 2100 within the experimental freestream velocity range. No viscous correction was thus necessary since its Reynolds numbers were much larger than 10 (ref. 15). The reading of the reference Pitot-static tube was further unaffected by the superimposed turbulence in the case of turbulent incident flow since it was positioned upstream of the turbulence-generating grid. There, the effect of prevailing turbulence, whose intensity was of the order of 0.4 to 0.45% (see Sect. 2.1), is completely negligible (refs. 16,17).

An electronic pressure meter (MKS Instruments Inc., MKS Baratron Type 77 with Type 77H Series Pressure Heads) was used to measure the dynamic pressure. This pressure meter is a differential micromanometer with an overall range of 30 mm Hg divided into eight ranges for higher accuracy and its resolution is 0.5 μm Hg. Its full scale DC output voltage for each range is 100 mV. This DC output voltage is linearly proportional to the pressure reading within 1 to 3 mV. It was measured by means of a digital integrating voltmeter (Dymec, Model 2401C) with a resolution of 1 μV. In conducting this pressure measurement an integration time of 30 s was utilized. The averaging time was monitored by means of an electronic counter (Hewlett-Packard Co., Model 522B).

The stream temperature was continuously monitored by means of a shielded copper-constantan thermocouple located in the same plane as the Pitot-static tube as shown in Fig. 2.2. A digital temperature indicator (Doric Scientific Div., Trendicator Model 415A) was used to measure the thermocouple output with a resolution of 0.056°C (0.1°F). In addition, the turbulence intensity of the freestream flow was continuously monitored by means of a hot-wire anemometer installed in the same plane as the Pitot-static tube.

3.3 Surface Pressure

A survey of the uniformity in the stagnation pressure along the span of the cylinder midsection was first carried out in order to check the flow two-dimensionality. To this end, the stagnation pressure was monitored in smooth incident flow in plane $\theta = 0°$ at 11 pressure taps along the span of the cylinder midsection, i.e., over a distance extending from $z = 43.20$ to -43.20 cm which amounts to 47% of the cylinder span (183 cm). Measurement of the surface (or wall) pressure distribution in smooth and turbulent incident flows (i.e., without and with the turbulence-generating grid installed upstream of the cylinder) was conducted over half the cylinder circumference in the mid-plane $z = 0$ in view of its symmetric distribution. The surface static pressure was monitored in smooth incident flow at 18 pressure ports distributed from $\theta = 0$ to 180° without rotating the cylinder. Measurement of the surface mean static pressure in turbulent incident flow included five additional stations in the interval 100 to 140° in order to provide greater resolution in that region where separation was expected. The survey at these additional stations was performed by rotating the cylinder. Sequential selection of each pressure orifice was achieved by means of a scanning valve and the wall pressure was measured using a measurement system identical to that utilized to monitor the reference Pitot-static tube (an electronic pressure meter, an integrating digital voltmeter and an electronic counter, see Sect. 3.2).

In conducting the surface pressure measurements in turbulent incident flow, the objective was to learn the effect of the oncoming amplified turbulence upon the mean pressure distribution and, hence, upon the separation. Consequently, the local fluctuating pressure was not monitored. An averaging time of 30 s was nevertheless applied in measuring the mean pressure. This averaging time was determined based on recovering the flow stagnation pressure at the stagnation-point pressure tap (at $\theta = 0°$). Furthermore, the measurements were repeated several times and average values were deduced.

The surface pressure coefficient is given by

$$C_p = [p(\theta) - p_\infty]/\tfrac{1}{2}\rho U_\infty^2 \ , \qquad (3.1)$$

in which $p(\theta)$ is the measured surface static pressure at any azimuthal angle θ, p_∞ and U_∞ denote the freestream static pressure and uniform velocity, respectively, and ρ stands for the density of air in consistent units. Both freestream static pressure and uniform velocity were measured by the reference Pitot-static tube (see Sect. 3.2).

The foregoing relation was used in computing the pressure coefficient in smooth incident flow. Its use in a turbulent incident flow is, on the other hand, hampered by the presence of the turbulence-generating grid between the reference Pitot-static tube and the cylinder. The grid produces losses that are readily expressed in terms of the difference in the stream static pressure Δp_∞ across it. Then the surface mean pressure coefficient in turbulent incident flow C_p' was computed, as described in App. I, according to the relationship

$$C_p' = C_p + \Delta p_\infty / \tfrac{1}{2}\rho U_\infty^2, \tag{3.2}$$

in which C_p is given by Eq. (3.1) and $\Delta p_\infty = p_\infty - p_\infty'$, where p_∞' denotes the freestream static pressure downstream of the grid.

The difference in the static pressure across the grid Δp_∞ was measured by means of two identical Pitot-static tubes in the absence of the cylinder. One was the reference tube while the second probe was located downstream of the grid exactly at the stagnation point of the cylinder but in its absence. The turbulence intensity at this position never exceeded 4.5% for all three grid positions at the freestream velocities of interest. No turbulence correction was applied to the reading of the downstream Pitot-static tube since it amounts to less than 1% at this level of turbulence (refs. 16,17).

The form (or pressure) drag of the cylinder was estimated based on the measured wall pressure. Within the subcritical Reynolds-number range of interest, the friction drag (skin friction) is completely negligible since it amounts to less than 2% of the total drag (refs. 2,18,19). Then the sectional cylinder drag coefficient was computed for both smooth and turbulent incident flows by integrating the measured pressure distribution according to the relationship

$$C_D = \int_0^\pi C_p \cos\theta \, d\theta \ , \tag{3.3}$$

where C_p is given by either Eq. (3.1) or (3.2) depending upon the nature of the oncoming flow. A modified trapezoidal rule for unequal intervals determined by the spacing of the pressure taps was used to numerically evaluate the drag coefficient.

3.4 Blockage Correction

The blockage effect (wall interference effect) was accounted for in reducing the data collected in smooth incident flow. It is apparent that the correction method advanced by Allen & Vincenti (ref. 20) is thus far the best available and the most widely used despite its inherent limitations (refs. 21,22,23). This correction method was advanced for an airfoil placed on the centerline of a wind tunnel in compressible flow, but it also applies at low speed (for the flow of an incompressible fluid). This method is particularly suited for correcting the drag coefficient of a circular cylinder when the blockage coefficient is smaller than 0.10 (ref. 22) and even it can be applied when the cylinder axis is not exactly located on the wind-tunnel centerline (ref. 23). For these reasons and for the sake of facilitating comparison with other germane results, the Allen-Vincenti correction technique was adopted herein.

The correction formulas for the freestream velocity and the drag coefficient are expressed at low velocity (i.e., in a flow of an incompressible fluid) in terms of their measured counterparts (U_∞ and C_D) and the blockage coefficient (D/h) by the relationships (ref. 20, Eqs. (94); see App. II)

$$U_\infty^*/U_\infty = 1 + 0.25C_D(D/h) + 0.82(D/h)^2 \ , \qquad (3.4)$$

and

$$C_D^*/C_D = 1 - 0.50C_D(D/h) - 2.467(D/h)^2 \ , \qquad (3.5)$$

in which the asterisk denotes corrected values and the measured drag coefficient C_D is given by Eq. (3.3). It follows that the correction for the Reynolds number is then exactly the same as for the freestream velocity expressed by Eq. (3.4), i.e., $Re^*/Re = U_\infty^*/U_\infty$.

The corrected pressure coefficient C_p^* was computed according to the relation (ref. 21; see App. II)

$$(C_p^* - 1)/(C_p - 1) = (U_\infty^*/U_\infty)^{-2} \ , \qquad (3.6)$$

where the freestream velocity ratio is given by Eq. (3.4). This equation is obtained under the condition that the difference between the wall static pressure $p(\theta)$ and the flow stagnation pressure p_o is the same in both the unrestricted and constrained streams, i.e., $p^*(\theta) - p_o^* = p(\theta) - p_o$. As a result, this correction for the pressure

coefficient depends solely on the correction for the freestream velocity.

It is important to stress that not all possible interference effects are accounted for by this blockage correction. The latter is more dependable when the drag coefficient is almost constant with varying Reynolds number (ref. 21) such as in the present smooth incident flow. Consequently, the blockage correction was consistently applied solely to the data obtained in smooth incident flow. In reducing the data obtained in turbulent incident flow, the blockage correction was not applied in view of the drastic variation in the drag coefficient with changing Reynolds number.

Another semiempirical correction scheme for a body in a smooth incident stream at low velocity proposed by Maskell (ref. 24) deserves attention in the light of its relative popularity. This method was initially developed for a sharp-edged bluff body where the origin of the wake is independent of the wind-tunnel constraint (i.e., for a bluff body with sharp-edge separation) and uniform base pressure. The wind-tunnel wall interference is represented in this method by a simple increase in the velocity of the unrestricted stream in view of the underlying assumption of invariance under constraint of the pressure distribution on the body. Then the corrected values of the pressure and drag coefficients, the base pressure parameter, the freestream velocity and the Reynolds number are related to their measured counterparts by the expression (ref. 24, Eq. (17))

$$(C_p^*-1)/C_p-1) = C_D^*/C_D = k^{*2}/k^2 = (U_\infty^*/U_\infty)^{-2} = (\overset{*}{Re}/Re)^{-2}, \quad (3.7)$$

in which the corrected values are also denoted by the asterisk. In the foregoing relationship, the base pressure parameter $k^2 = 1 - C_{pb}$, where C_{pb} designates the base pressure coefficient. The corrected base pressure parameter $k^{*2} = 1 - C_{pb}^*$ is further approximated by successive iterations according to the formula (ref. 24, Eq. (16))

$$k_n^{*2} = k^2 \left[1 + \frac{C_D \, D/h}{k_{n-1}^{*2} - 1} \right]^{-1}, \quad (3.8)$$

where k_n^{*2} is the nth approximation to the base pressure parameter and when the zeroth approximation is the measured base pressure parameter k^2.

The Maskell method of correcting the drag coefficient was satisfactorily substantiated for blockage coefficients up to 0.045 (ref. 25) but it was used even for a blockage coefficient of 0.20 (ref. 26). On the other hand, this approach apparently leads to erroneous correction for the pressure coefficient and, consequently, an empirical modification was proposed to this end in Ref. 25. It is further important to point out that slight variations of the Maskell technique have been applied to correct the drag coefficient for a variety of bluff bodies without meeting the essential conditions of sharp-edge separation and uniform base pressure (refs. 23,26), despite the admonition of its own proponent (ref. 24). In that vein, the Maskell method was applied in the present study to selected cases in smooth incident flow in order to illustrate the disparities that can occur in the values of the various corrected flow parameters when different correction methods are used.

4. FLOW ESTABLISHMENT

The investigation of the pressure distribution along the cylinder surface was conducted in smooth and turbulent incident flows at exactly the same five subcritical Reynolds numbers. Smooth (or laminar) incident flow is the approaching crossflow in the absence of a turbulence-generating grid upwind of the cylinder while turbulent incident flow is the oncoming crossflow in the presence of a turbulence-generating grid. As previously mentioned, the Reynolds number was based on the cylinder diameter and the uniform freestream velocity upstream of the cylinder and/or the turbulence-generating grid. The five cylinder-diameter Reynolds numbers Re and their corresponding freestream velocities U_∞, which are listed in Table A.III.1 in App. III, are: $5.2\text{x}10^4$, $9.4\text{x}10^4$, $1.25\text{x}10^5$, $1.67\text{x}10^5$, $2.09\text{x}10^5$ and 4.9, 8.8, 11.7, 15.6, 19.5 m/s (16, 28.8, 38.4, 51.2, 64 ft/s), respectively.

The results obtained in smooth incident flow are presented in their corrected form according to the Allen-Vincenti method unless otherwise mentioned. The corrected cylinder-diameter Reynolds numbers $R\overset{*}{e}$ and uniform freestream velocities U_∞^*, which are also tabulated in Table A.III.1, App. III, are: $5.4\text{x}10^4$, $9.7\text{x}10^4$, $1.29\text{x}10^5$, $1.72\text{x}10^5$, $2.14\text{x}10^5$ and 5, 9, 12, 16, 20 m/s (16.5, 29.6, 39.5, 52.6, 65.7 ft/s), respectively. In addition, the thickness of the laminar boundary layer at stagnation point δ_ℓ (see Eq. (2.1)) and the neutral scale λ_0 (vid., Eq. (2.2)) corresponding to these five Reynolds numbers (uncorrected) are given in Table A.III.2, App. III, for convenience. Their dimensionless values defined in terms of the cylinder radius R-viz., $\tilde{\delta}_\ell = \delta_\ell/R$ and $\tilde{\lambda}_0 = \lambda_0/R$-are also summarized there.

The correction for the uniform freestream velocity and Reynolds number was always smaller than 3%. Higher corrected values, amounting from 5.8 to 7.1% with increasing freestream velocity, were consistently obtained when the Maskell correction method was applied. As a result, the corrected uniform freestream velocities and Reynolds numbers computed by means of the Maskell scheme were 3.3 to 4.5% larger than their counterparts calculated according to the Allen-Vincenti method. The corrected freestream velocities and Reynolds numbers obtained by the Maskell scheme, along with the ratio of the corrected freestream velocity computed by Maskell scheme to its counterpart obtained by Allen-Vincenti method $U_{\infty M}^*/U_\infty^*$, are given in Table A.III.3, App. III, for the sake of illustrating their overestimation with respect to their values computed by the Allen-Vincenti method.

Cartesian and polar coordinates, which are shown in Fig. 2.1, are used in presenting the results. The latter coordinates are employed in reporting the surface pressure distribution and for pointing out particular azimuthal positions of interest along the cylinder circumference. Dimensionless Cartesian coordinates are defined in terms of the cylinder radius R (7.94 cm) by

$$\tilde{x},\ \tilde{y},\ \tilde{z} = x/R,\ y/R,\ z/R\ . \qquad (4.1)$$

A prerequisite in carrying out this investigation was to ensure that the oncoming freestream turbulence was the sole factor affecting the separation and the drag coefficient. In order to meet this goal it was imperative: (1) to minimize the effect of the surface roughness; (2) to assess the flow two-dimensionality; and, (3) to alleviate leakage of high pressure air from the stagnation zone into the near wake through the cylinder end gaps. The last two conditions were checked in smooth incident flow.

Surface roughness induces an increase in the separation angle and an associated decrease in the drag coefficient. The relative surface roughness of the cylinder used was $1.6\text{x}10^{-5}$ (see Sect. 2.2) which is one of the lowest reported (ref. 27). In the light of this extremely fine relative surface roughness, one can assume that this cylinder was in practice perfectly smooth.

Inspection of the flow two-dimensionality was confined, to the cylinder midsection which extended from $\tilde{z} = 5.44$ to -5.44 as shown in Fig. 2.1. Reasonable two-dimensional flow was expected since the effective slenderness (diameter-to-span ratio) of this cylinder was 0.087 (see Sect. 2.2). The criterion in ascertaining the flow two-dimensionality was a spanwise variation of the stagnation pressure coefficient C_{po} (C_p at $\theta = 0°$) not larger than 1%. This condition was fulfilled over the entire Reynolds-number range. For example, at a Reynolds number of $9.7\text{x}10^4$ the maximum spanwise variation of the stagnation pressure coefficient along the cylinder midsection span amounted to 0.7%. Thus, the flow along the cylinder midsection was satisfactorily two-dimensional.

Prevention of leakage of high pressure air from the stagnation zone into the near wake was achieved by successively sealing all potential pathways through the cylinder end gaps until no further change in the base pressure coefficient was detected. The base pressure is taken herein, as commonly done (ref. 28), as the surface pressure at the base point $\theta_b = 180°$ notwithstanding that the surface pressure within the base region (i.e., the separated flow region

or the wake region) generally exhibits a slight variation. One can define the base pressure by an average of the surface pressure over the entire base region or over a selected arc around $\theta = 180°$ in order to account for its variation. Such an average base pressure leads to an underestimation in the drag coefficient (ref. 29) and, hence, it is advisable not to use it. Tests for the leakage were conducted at all five Reynolds numbers and in every case the sealing caused the base pressure to level off. For instance, at a Reynolds number of 1.29×10^5 the base pressure leveled off at an absolute value about 8.5% larger than its initial value, e.g., the sealing reduced the base pressure coefficient from -0.767 to -0.832. Similar leveling of the base pressure was obtained at the other Reynolds numbers and, therefore, the leakage was adequately controlled. In conclusion, *the flow conditions were deemed adequate for conducting the desired experimental investigation.*

5. RESULTS IN SMOOTH INCIDENT FLOW

5.1. Surface Pressure Distribution

The surface pressure distribution was measured in smooth incident flow in order to establish a reference against which to assess the effect of turbulence. The turbulence intensity of the smooth incident flow varied from 0.56 to 0.42% with increasing Reynolds number (corrected) from 5.4×10^4 to 2.14×10^5 and, thus, its level was of the same magnitude as that in an empty test section (0.4 to 0.45%, see Sect. 2.1).

The distribution of the corrected (Allen-Vincenti method) pressure coefficient C_p^* with increasing azimuthal angle θ over half of the cylinder at each of the five subcritical Reynolds numbers is shown in a polar form in Fig. 5.1 and in conventional form in Figs. 5.2 and 5.3. Positive and negative pressure coefficients are represented in the polar plots by inward and outward pointing arrows, respectively. For the sake of illustration, the pressure coefficient distribution computed according to potential flow theory-i.e., a cylinder in uniform flow, $C_p = 1 - 4\sin^2\theta$ (ref. 30)-is depicted in Fig. 5.1(a). The measured pressure coefficients (C_p) and their corrected values according to both Allen-Vincenti (C_p^*) and Maskell (C_{pM}^*) methods, along with the corresponding ratios of the latter to the former (C_p^*/C_p and C_{pM}^*/C_p), are given at all the five Reynolds numbers in Table A.IV.1 in App. IV. In addition, the ratios of the corrected values obtained by the Maskell scheme to those obtained by the Allen-Vincenti method (C_{pM}^*/C_p^*) are also tabulated in this table. The correction in the pressure coefficient varies with the azimuthal angle. It amounted from 0.1 to about 6% with increasing peripheral angle from 5 to 25°. The largest correction of about -26 to -28% was consistently found at 40°. Within azimuthal angles from 80 to 180° the correction was about -11%. Corrections larger than even twice those were invariably obtained by means of the Maskell scheme. It is thus apparent that the Maskell method overestimates the blockage effect for a bluff body.

The minimum pressure coefficient C_{pm}^* was constantly monitored at an azimuthal angle of about 70° while the base region (i.e., the region of nearly constant pressure) started at an azimuthal angle of about 80° at all five subcritical Reynolds numbers. These features are clearly exhibited by the distributions of the pressure coefficient portrayed in Figs. 5.1 to 5.3. Note that the angular position of minimum pressure is marked off in Figs. 5.2 and 5.3

by θ_m. Within the base region, the change in the pressure coefficient with respect to the base pressure coefficient C_{pb} (C_p at $\theta_b = 180°$) amounted from -4 to about +5.6%. Similar pressure distributions are reported in refs. 7 (p. 21), 19 & 31 at comparable subcritical Reynolds numbers. A minimum pressure near 70° is reported in refs. 7 (p. 21) & 31 at a Reynolds number of 1.9×10^5 while at a Reynolds number of 10^5 a minimum in the pressure at about 65° is reported in ref. 19. Inspection of the pressure coefficient distributions given in these three references reveals that the base region always starts at an angle of about 80°.

5.2 Laminar Separation Angle

The separation angle θ_s was estimated based on the distribution of the pressure coefficient since the skin friction was not measured. Recall that the friction drag is about 2% of the total drag within this Reynolds-number range (see Sect. 3.3). Although the separation evolves over a relatively narrow finite region, the point at which the skin friction vanishes is considered as the separation angle since it indicates the completion of the boundary layer separation. At the same time, the angle of zero skin friction corresponds to the beginning point of the base region (refs. 2,19). This criterion was applied here and, hence, the angular position where the base region begins was taken as the separation angle. Examination of the pressure coefficient distributions displayed in Figs. 5.2 to 5.3 reveals, according to the foregoing criterion, a laminar (or smooth flow) separation angle θ_s of about 80° at all five subcritical Reynolds numbers. Note that the separation angle is marked off by θ_s in these figures.

This separation angle was further confirmed by the dry-surface coating visualization of the separation line. At all Reynolds numbers, a separation angle of about 80° within ±2° (±2.5%) was consistently indicated by the visualization. A sample of the separation line disclosed by the visualization is shown in the black-and-white still photograph given in Fig. 5.4 which was reproduced from a color movie. The separation line is delineated by the transition band between the deep red separated flow region and the plain blue attached flow region. In the black-and-white still, the red and blue regions are represented by the light and dark areas which are denoted by R and B, respectively. A scale marking off the azimuthal angle at 5° intervals, with its origin at the stagnation point, is incorporated in the still for convenient estimation of the separation angle.

A similar laminar separation angle is reported in the literature for a nominally smooth cylinder at subcritical Reynolds numbers. For instance, a laminar separation point of about 81° is given in ref. 7 (p. 173). Laminar separation angles varying randomly between 73 and 84° are reported in ref. 19 at Reynolds numbers (measured) ranging from $6x10^4$ to $2x10^5$ for a cylinder with a relative surface roughness of $1.33x10^{-5}$. In ref. 32, a laminar separation angle between 80 to 85° is reported for Reynolds numbers (measured) of 10^4 to 10^5. In the oft-cited early investigation of Fage & Falkner (ref. 2), a laminar separation point of about 81° is reported at Reynolds numbers (measured) ranging from $6x10^4$ to $1.06x10^5$ for a cylinder 7.44 cm (2.93 in) in diameter, and of 78° at a Reynolds number of $1.06x10^5$ for a cylinder 14.96 cm (5.89 in) in diameter. On the other hand, extremely large separation angles of 130 and 140° are reported for the latter cylinder at Reynolds numbers (measured) of $2.12x10^5$ and $1.66x10^5$, respectively, in a nominally smooth incident flow. It is suspected that these two large separation angles were induced by some unreported changes in the turbulence level of the incident flow and/or by the cylinder surface roughness. The lack of a better agreement among the various results can be attributed, in all likelihood, to differences in the cylinder surface roughness, the blockage coefficient, the turbulence level of the nominally smooth incident crossflow, the experimental conditions (e.g., the leakage) and procedure. One cannot, unfortunately, estimate these effects due to the want of sufficient information. At the present time, the accepted value of the laminar separation angle in a smooth incident flow at subcritical Reynolds numbers up to $2x10^5$ is apparently about 80° (ref. 28). Thus, *the laminar separation angle of about 80° measured in this experiment is in agreement with its commonly accepted value.*

5.3 Discussion of Pressure Distribution

Comparison of the pressure distribution obtained in this study with those of other investigations is of interest for the purpose of corroboration. To this end, the measured pressure coefficient distributions on a smooth circular cylinder in a smooth incident crossflow at similar subcritical Reynolds numbers reported by Fage & Falkner (ref. 2), Achenbach (ref. 19), Modi & El-Sherbiny (ref. 26), Batham (ref. 33) and Guven et al. (ref. 34) were used. The pressure coefficient distributions were grouped into five classes based on close correspondence of the Reynolds numbers given in these studies to those in the present test, viz., within ±15%. These five groups are outlined in Table 1 below in which the measured and corrected cylinder-diameter Reynolds number (Re and Re^*), the blockage coefficient (D/h), the relative surface roughness (k/D), the cylinder slenderness (D/S) and the freestream turbulence

intensity (Tu_∞) of the approaching nominally smooth flow are listed for each one of these five studies and for the present test. No information concerning the surface roughness is supplied in these papers except by Achenbach (ref. 19). Only the overall appearance of the surface is described in the other studies as 'highly polished' (ref. 2), 'smooth as machined' (ref. 33) or 'smooth to the touch' (ref. 34). In ref. 26 no mention of the surface roughness is made. Data on the freestream turbulence intensity is always provided except by Fage & Falkner (ref. 2). Lack of information is denoted in Table 1 by NR which means not reported. Whenever the reported data was not corrected for the blockage effect, as annotated in Table 1 below by UC (means uncorrected), the Allen-Vincenti correction method was applied for standardization's sake. Information about preventing leakage of high pressure air from the stagnation zone into the near wake is not reported in any of these studies.

TABLE 1. CYLINDER DATA SUMMARY

Source	Ref.	Re ($\times10^{-4}$)	$R\check{e}$	D/h (%)	k/D ($\times10^{5}$)	D/S (%)	Tu_∞ (%)	BC	Fig. No.
Present Test		5.2	5.4	8.7	1.6	8.7	0.56	C	
Modi & El-Sherbiny	26,Fig. 1	5.0	5.2	9.0	NR	12.0	0.07	UC	5.5
Fage & Falkner	2,Tb. III*	6.0	6.1	6.1	NR	6.1	NR	UC	
Present Test		9.4	9.7	8.7	1.6	8.7	0.46	C	
Modi & El-Sherbiny	26,Fig. 1	8.0	8.2	9.0	NR	12.0	0.07	UC	5.6(a)
Fage & Falkner	2,Tb. III*	8.3	8.5	6.1	NR	6.1	NR	UC	
		10.6	10.8	6.1	NR	6.1	NR	UC	5.6(b)
Achenbach	19,Fig. 3	10.0	10.7	16.7	$1^1/_3$	30.0	0.70	UC	
Present Test		12.5	12.9	8.7	1.6	8.7	0.45	C	
Batham	33,Fig. 1	10.9	11.1	5.0	NR	15.0	0.50	C	5.7
Fage & Falkner	2,Tb. III+	10.6	11.1	12.3	NR	12.3	NR	UC	
Present Test		16.7	17.2	8.7	1.6	8.7	0.44	C	5.8
Fage & Falkner	2,Tb. III+	16.6	17.2	12.3	NR	12.3	NR	UC	
Present Test		20.9	21.4	8.7	1.6	8.7	0.42	C	
Fage & Falkner	2,Tb. III+	21.2	21.8	12.3	NR	12.3	NR	UC	5.9
Guven et al.	34,Tb. 4.2	20.7	22.4	17.8	NR	32.4	0.20	C	

Tb. means Table; BC means blockage correction; NR means nonreported; C means corrected; UC means uncorrected; *2.93 in dia. cyl.; +5.89 in dia. cyl.

The distributions of the pressure coefficient C_p^* over half of the cylinder for the cases listed in Table 1 are portrayed in Figs. 5.5 to 5.9 where they are identified according to their Reynolds number $R\check{e}$ and blockage coefficient. The latter is specified in view of its wide range

covered in these investigations, viz., D/h = 0.05 to 0.178. Examination of the pressure coefficient distributions reveals that *the results of the present investigation are basically consistent with those of other studies* except for the distributions measured by Fage & Falkner (ref. 2) at Reynolds numbers of 1.72×10^5 and 2.18×10^5 (vid., Figs. 5.8 & 5.9). Differences among the various distributions of the pressure coefficient are, however, observed at practically the same Reynolds numbers starting for the most part from a peripheral angle of about 60°.

In order to underscore the essential features of these differences, the variations of the pressure coefficients with increasing Reynolds number was examined at several selected azimuthal angles. To this end, the variations of: (1) the pressure coefficient in the favorable pressure gradient region at $\theta = 30°$; (2) the pressure coefficient at $\theta = 70°$, which generally corresponds to the point of minimum pressure coefficient; and, (3) the base pressure coefficient C_{pb} (C_p at $\theta = 180°$) obtained in the present test and in the other five studies are displayed as a function of increasing Reynolds number in Fig. 5.10. For consistency's sake, the blockage coefficient for each case is given in this figure. The largest scattering is exhibited at any Reynolds number by the pressure coefficient at $\theta = 70°$ even when the blockage coefficient is practically the same. For instance, a difference of about 24% is found between the results of Fage & Falkner (ref. 2, D/h = 0.061) and Batham (ref. 33, D/h = 0.05) at a same Reynolds number of about 11.1×10^4. Larger discrepancies and opposite trends are observed as the difference among the blockage coefficients becomes greater. The differences between the pressure coefficients at $\theta = 70°$ obtained in the present study and that reported by Guven et al. (ref. 34), on the one hand, and that given by Fage & Falkner (ref. 2), on the other hand, amount to 25 and 55%, respectively, when the attendant blockage coefficients are 0.087, 0.178 and 0.123. Smaller differences are observed for the base pressure coefficient and the smallest differences are found in the favorable pressure gradient region at an angle of 30°. It is interesting to note that the pressure coefficients reported by Fage & Falkner (ref. 2) are the lowest in all cases except for the base pressure coefficients at Reynolds numbers larger than 1.5×10^5 which are greater than all the others. The pressure coefficients obtained in the present investigation at these three azimuthal angles are in good agreement with those reported by Modi & El-Sherbiny (ref. 26) at corresponding blockage coefficients.

5.4 Parameters Affecting the Pressure Distribution

One cannot readily assess the reasons for the differences in the pressure coefficient distributions since they are induced by a variety of causes which act simultaneously. These causes were, as a matter of fact, previously alluded to regarding the observed discrepancies in the laminar separation angle. The cylinder slenderness is not considered herein since its effect on the pressure distribution is, apparently, completely negligible at subcritical Reynolds numbers (refs. 34,35). Leakage of high pressure air from the stagnation zone into near wake through the cylinder end gaps leads to higher pressure (less negative pressure) in the base region. No attempt to assess the contribution of the leakage to the observed differences in the pressure coefficient distributions was undertaken because of nonavailability of data.

Increasing blockage at a given Reynolds number promotes lower positive pressure coefficients and further reduction in the negative pressure coefficients provided that both the surface roughness and freestream turbulence level are unchanged (ref. 23,26,36). A similar effect occurs at constant blockage with increasing Reynolds number all else being the same. Removal of the blockage effect by means of a correction scheme, as the one applied here, is not entirely successful in securing a unique pressure distribution at given Reynolds number. This is distinctly borne out by inspection of the distributions of the corrected pressure coefficient obtained at essentially the same Reynolds numbers but with different blockage coefficients displayed in Figs. 5.5 to 5.10. One thus must consider the relative surface roughness and the freestream turbulence level to better explain the discrepancies encountered in the pressure coefficient distributions.

Higher relative surface roughness induces at subcritical Reynolds numbers, all other factors being the same, a reduction (a more negative) in the minimum pressure coefficient, (refs. 1,27,34). On the other hand, its effect upon the pressure distribution within the base region is not yet clearly established. The pressure coefficient there can be either larger or smaller than that for a smooth cylinder depending on the particular subcritical Reynolds number (refs. 1,27). Freestream turbulence generally affects the pressure distribution in a manner similar to the surface roughness (refs. 1,2,26) provided that its scales are commensurate with the thickness of the prevalent laminar boundary layer (ref. 6). In view of the fact that in most of the cited studies the cylinder surface is only qualitatively classified as being 'highly polished' or 'smooth,' any reasonable estimation of the role played by this factor with

regard to the observed disparities in the pressure distributions is not feasible. Similarly, one cannot assess the effect of the freestream turbulence since no information concerning its scale structure is given and even its intensity is not reported in all the cases (e.g., Fage & Falkner, ref. 2).

When the Reynolds number, the relative surface roughness and the freestream turbulence level are comparable, similar distributions of the corrected pressure coefficient are expected. This is clearly revealed by the pressure coefficient distributions obtained in the present experiment and by Achenbach (ref. 19) which are displayed in Fig. 5.6(b). These pressure distributions were obtained at Reynolds numbers of 9.7×10^4 and 1.07×10^5, relative surface roughnesses of 1.6×10^{-5} and 1.33×10^{-5}, and freestream turbulence intensities of 0.46 and 0.7%, respectively (see Table 1). The pressure coefficients reported in these two cases are practically identical everywhere (within the limits of the experimental error) except in the neighborhood of the minimum pressure and within the adverse pressure gradient region (for $60° < \theta < 80°$) as observed in Fig. 5.6(b). These differences can, in all likelihood, be ascribed to the limitation in the blockage correction. Recall that the blockage coefficient in Achenbach's experiment (ref. 19) was almost twice as great than that in the present study (0.087 v. 0.167, vid., Table 1). The largest disparities in the pressure coefficients are found between the results obtained in the present investigation and those given by Fage & Falkner (ref. 2) within the neighborhood of minimum pressure and the adverse pressure gradient region at Reynolds numbers of 1.72×10^5 and 2.14×10^5 (vid., Figs. 5.8 & 5.9). The different variations of the pressure coefficients given by Fage & Falkner (ref. 2) strongly suggest that they are due to some unreported relative surface roughness and/or freestream turbulence. Recall that extremely large separation angles (140 and 130°) were reported by Fage & Falkner (ref. 2) at these two Reynolds numbers.

5.5 Laminar Drag Coefficient

The sectional laminar drag coefficient $C_{D\ell}$ was computed at each Reynolds number in order to establish a useful datum for judging the extent to which its value is affected by turbulence. Computation of the drag coefficient was accomplished by integrating the measured surface pressure distribution according to Eq. (3.3). This drag coefficient represents solely the form (or pressure) drag which amounts to more than 98% of the total drag within the present subcritical Reynolds-number range, as previously mentioned (refs. 2,18,19).

Variations of the measured and corrected (Allen-Vincenti method) drag coefficients ($C_{D\ell}$ and $C^*_{D\ell}$) with increasing measured and corrected Reynolds number (Re and $R\overset{*}{e}$) are displayed in Figs. 5.11 and 5.12, respectively. The measured drag coefficients ($C_{D\ell}$) and its corrected values obtained by both Allen-Vincenti ($C^*_{D\ell}$) and Maskell ($C^*_{D\ell M}$) schemes, along with the corresponding ratios of the corrected to measured values ($C^*_{D\ell}/C_{D\ell}$ and $C^*_{D\ell M}/C_{D\ell}$), are tabulated in Table A.V.1 in App. V. In addition, the ratios of corrected drag coefficients obtained by Maskell scheme to those computed by Allen-Vincenti method ($C^*_{D\ell M}/C^*_{D\ell}$) are also given in this table. Values of the measured drag coefficient $C_{D\ell}$ ranging from 1.07 to 0.93 were obtained with increasing Reynolds number Re from $5.2\text{x}10^4$ to $2.09\text{x}10^5$, i.e., a decrease in the drag coefficient of about 13% over a fourfold increase in the Reynolds number as shown in Fig. 5.11. The drag coefficients corrected by the Allen-Vincenti method $C^*_{D\ell}$ varied from 1.0 to 0.87 over the corresponding range of the corrected Reynolds number from $5.4\text{x}10^4$ to $2.14\text{x}10^5$ as observed in Fig. 5.12. Thus, the blockage correction amounted to about 6.5%. Larger corrections of 11 to 13% were obtained in applying the Maskell method (see App. V). These results, which exhibit a trend similar to that for the corrected pressure coefficient, further reinforce the conclusion that the Maskell scheme leads to overestimation of the blockage correction for a bluff body.

5.6 Discussion of Drag Coefficient

The drag coefficients found in the present experiment were further compared with those obtained in several other investigations in a nominally smooth incident flow at corresponding subcritical Reynolds number in order to gain a better perspective. In addition to the findings presented in the five studies listed in Table 1, drag coefficients reported by Fage & Warsap (ref. 1), Giedt (ref. 3), Wieselsberger (ref. 37), Schmidt & Wenner (ref. 38), Bursnall & Loftin (ref. 39), Delany & Sorensen (ref. 40) and Polhamus (ref. 41) were employed for this purpose. These drag coefficients were obtained by: (1) integration of the pressure distribution, i.e., form drag (refs. 2, 3, 33, 34, 38 (see ref. 3), and 39); (2) integration of both pressure distribution and skin friction, i.e., total drag (ref. 19); and, (3) measurement of the total drag by means of a force balance (refs. 1,26,37,40,41). The ranges in the values of the drag coefficient and in the corresponding cylinder-diameter Reynolds number given in these twelve selected investigations along with those in the present test are summarized according to their increasing blockage

coefficient (D/h) in Table 2 below. In addition, the relative surface roughness (k/D) and the freestream turbulence (Tu_∞) of the nominally smooth incident flow are listed, whenever reported, in this table. Lack of information is also denoted in this table by NR which means not reported in view of their relevance.

TABLE 2. CYLINDER DRAG COEFFICIENT DATA

PART I. DRAG COEFFICIENT-MEASURED

Source	Ref.	Re ($\times 10^{-4}$)	$C_{D\ell}$	D/h (%)	k/D ($\times 10^5$)	Tu_∞ (%)
Wieselsberger	37, Fig. 1	5.0 -20.0	1.20-1.10	-	NR	NR
Schmidt & Wenner	38, Fig. 6	3.98-17.0	0.97-0.81	-	NR	NR
Bursnall & Loftin	39, Fig. 9	20.0	1.2	2.0	NR	NR
Fage & Falkner	2, Tb. II*	6.0 -10.6	1.19-1.22	6.1	NR	NR
Present Test		5.2 -20.9	1.07-0.93	8.7	1.6	0.56-0.42
Modi & El-Sherbiny	26, Fig. 4	5.0 - 9.0	1.0	9.0	NR	0.07
Giedt	3, Fig. 6	6.9 -21.2	1.18-0.41	11.1	NR	<1.0
Fage & Falkner	2, Tb. II+	10.6 -21.2	1.24-0.52	12.3	NR	NR
Fage & Warsap	1, Fig. 1	4.7 -20.9	1.08-0.54	12.7	NR	NR
Achenbach	19, Fig. 9	4.0 -22.5	1.24-0.78	16.7	$1^1/_3$	0.70
Guven et al.	34, Tb. 4.2	15.5 -20.8	1.31-1.22	17.8	NR	0.20
Modi & El-Sherbiny	26, Fig. 4	5.0 -20.0	1.31-1.33	20.5	NR	0.07

*2.93 in dia. cyl.; +5.89 in dia. cyl.

PART II. DRAG COEFFICIENT-BLOCKAGE CORRECTED

Source	Ref.	Re^* ($\times 10^{-4}$)	$C^*_{D\ell}$	D/h (%)	k/D ($\times 10^5$)	Tu_∞ (%)
Delany & Sorensen	40, Fig. 5*	5.0-10.0	1.1	1.0	NR	NR
Delany & Sorensen	40, Fig. 5+	5.0-20.0	1.0	3.0	NR	NR
Batham	33, Tb. 1	11.1	1.17	5.0	NR	0.50
Present Test		5.4-21.4	1.00-0.87	8.7	1.6	0.56-0.42
Polhamus	41, Fig. 3	12.7-20.0	1.19-1.13	10.0	NR	NR
Guven et al.	34, Tb. 4.2	16.8-22.5	1.06-0.99	17.8	NR	0.20

Tb. means Table; NR means not reported; *2.93 in dia. cyl.; +5.89 in dia. cyl.

The data in Table 2 is tabulated as given in the above investigations, i.e., either measured or corrected for the blockage effect. No attempt was undertaken to apply the blockage correction whenever it was not initially performed. The reason for this was to pinpoint the role played by the blockage in determining the drag since, generally, the latter is higher with increasing blockage coefficient. As a result, Table 2 is divided into two parts. Measured data is summarized for ten different blockage coefficients ranging from 0.020 to 0.205 in Part I while corrected data for six different blockage coefficients varying from 0.010 to 0.178 are tabulated in Part II. The results of the present test are included in both parts. No blockage coefficients are given for the data reported by Wieselsberger (ref. 37) and Schmidt & Wenner (ref. 38) since they were obtained in an open-jet flow wind tunnel and in a partially open stream

from a nozzle, respectively. Information concerning the relative surface roughness is given only by Achenbach (ref. 19) and in the present experiment. Data on the free-stream turbulence intensity is provided in nine out of the seventeen cases as indicated in Table 2. Lack of data is designated in this table, as previously, by NR which means not reported.

The variations of the measured and corrected drag coefficient with increasing Reynolds number for all the cases listed in both parts of Table 2 are displayed in Figs. 5.11 and 5.12, respectively. Each case is identified in these two figures by its blockage coefficient D/h. Inspection of these variations indicates that *the drag coefficient obtained in the present test is generally within the bulk values reported in the other investigations*. For instance, the measured drag coefficients found in the present experiment at Reynolds numbers in the range 5.2×10^4 to 9.4×10^4 are about 7 to 5% larger than those reported by Modi & El-Sherbiny (ref. 26) at comparable blockage coefficient (0.087 v. 0.09) and background freestream turbulence intensity (0.56 to 0.46% v. 0.07%; vid., Fig. 5.11). At Reynolds numbers ranging from about 5×10^4 to 1.3×10^5, the measured drag coefficients obtained herein are within -6 to +3% of their counterparts given by Fage & Warsap (ref. 1) despite the fact that the blockage coefficient in the latter case was about 46% greater than that in the present test (1.123 v. 0.089; vid., Fig. 5.11). In the Reynolds-number range from 1.25×10^5 to 2.09×10^5, the measured drag coefficients found here are from 3 to 11% larger than those reported by Achenbach (ref. 19) at comparable relative surface roughness (1.6×10^{-5} v. 1.33×10^{-5}) and background freestream turbulence intensity (0.45 to 0.42 v. 0.7%) even though the blockage coefficient in the former case amounted to 52% of the latter (0.087 v. 0.167; vid., Fig. 5.11). All these differences in the drag coefficients are, in all likelihood, within the limits of experimental error provided that the role of the blockage is disregarded.

Further scrutiny of the variations of the measured drag coefficients listed in Table 2, Part I, and displayed in Fig. 5.11 reveals significant scattering in the results of the various investigations. All the drag coefficients surveyed within the Reynolds-number range from about 5×10^4 to 2×10^5 are confined between a maximum of 1.33 (ref. 26) and a minimum of 0.41 (ref. 3). Particularly conspicuous is the random variation of the drag coefficient within this range regardless of the corresponding blockage coefficient. As a matter of fact, the values of the drag coefficient are not in clear agreement with their expected increase with higher blockage. For instance, an almost constant drag coefficient of 1.20 and drag coefficients varying between 0.97 to 0.81

are reported by Wieselsberger (ref. 37) and by Schmidt & Wenner (ref. 38), respectively, under conditions of practically no blockage. Moreover, the drag coefficients given by Wieselsberger (ref. 37) at Reynolds numbers larger than $12x10^4$ are greater than those found by Giedt (ref. 3), Fage & Falkner (ref. 2), Fage & Warsap (ref. 1), Achenbach (ref. 19) and in the present experiment at blockage coefficients ranging between 0.087 and 0.167. Drag coefficients found by Modi & El-Sherbiny (ref. 26) at a blockage coefficient of 0.090 are smaller than those reported in the other studies at both lower and higher blockage coefficients. Likewise, the drag coefficient given by Bursnall & Loftin (ref. 39) at a relatively low blockage coefficient of 0.020 is larger than its counterparts at the same Reynolds number and at much higher blockage coefficient found in several other investigations (see Giedt (ref. 3), Fage & Falkner (ref. 2), Fage & Warsap (ref. 1), Achenbach (ref. 19), and the present experiment). This drag coefficient is, in fact, of almost the same magnitude (smaller by about 2%) as that reported by Guven et al. (ref. 34) at a blockage coefficient of 0.178.

The variations of the blockage-corrected drag coefficients $C^*_{D\ell}$ summarized in Table 2, Part II, and portrayed in Fig. 5.12 exhibit disparities similar to those observed for the measured ones. It is apparent that a unique value for the drag coefficient at a given Reynolds number is not obtainable as a result of applying the blockage correction. An identical conclusion was reached previously, as a matter of fact, when the pressure distribution was corrected for the blockage. The corrected drag coefficients examined range between a maximum of 1.19 (ref. 41) and a minimum of 0.87 (present test), i.e., a 27% change. As far as the distribution of the corrected drag coefficient within this range is concerned, it reveals a random variation with the blockage coefficient similar to that observed for the measured one. For instance, the corrected drag coefficients $C^*_{D\ell}$ obtained here at Reynolds numbers Re^* ranging from $5.2x10^4$ to $1.29x10^5$ are within 3% smaller than those given by Delany & Sorensen (ref. 40) at a blockage coefficient of about 1/3 of that in the present study (0.03 v. 0.087) as observed in Fig. 5.12. The corrected drag coefficient reported by Batham (ref. 33) at a blockage coefficient of 0.050 is higher than those found in other studies at blockage coefficients both smaller and larger and, furthermore, is of the same magnitude as those given by Polhamus (ref. 41) at a blockage coefficient twice as large (0.10, vid., Fig. 5.12). Corrected drag coefficients given by Delany & Sorensen (ref. 40) at two relatively low blockage coefficients (0.010 and 0.030) differ by 10% in their values with the larger ones at the smaller blockage coefficient. Both sets of these drag coefficients are smaller

than those reported by Batham (ref. 33) and Polhamus (ref. 41) at higher blockage coefficients (0.050 and 0.10) and, at the same time, larger than those found in the present experiment at a blockage coefficient of 0.087 as observed in Fig. 5.12. Moreover, the values of the corrected drag coefficient reported in ref. 40 at a blockage coefficient of 0.030 are smaller within at most 6% than those given by Guven et al. (ref. 34) at a blockage coefficient of 0.178 for Reynolds numbers greater than 1.6×10^5.

The foregoing brief examination of both the measured and the blockage-corrected drag coefficients indicates that their variations are not consistent with the trend called for by increasing blockage and reveals that the capability of the correction in compensating for the blockage is limited. Other factors that can affect the value of the drag coefficient at any given blockage are the relative surface roughness, the freestream turbulence intensity of the nominally smooth incident flow and the leakage effect, as previously mentioned with regard to the pressure distribution. Larger relative surface roughness and higher freestream turbulence intensity lead to a lower drag coefficient (refs. 1,27). A similar effect is induced by leakage of high pressure air from the stagnation zone into the near wake. The latter depends upon the particular experimental setup and it is more likely to occur when the drag is measured by means of a force balance. Whenever leakage was detected (refs. 1,40) no action to prevent it was taken.

The extent to which the observed scattering in the values of the drag coefficient (measured and corrected) was affected by these three agents cannot, at the present time, be assessed due to the lack of sufficient information (vid., Table 2). One can, however, conjecture that these factors played a role in those cases when unusually low drag coefficients were found at subcritical Reynolds numbers. For instance, the relatively low measured drag coefficients given by Fage & Warsap (ref. 1), Fage & Falkner (ref. 2) and Giedt (ref. 3) at Reynolds numbers greater than 1.2×10^5 and at almost identical blockage coefficients (0.127, 0.123 and 0.111, respectively; 14% variation) can, in all likelihood, be attributed to either unreported surface roughness or to changes in the freestream turbulence or both. Leakage also could have played a role in inducing the low drag coefficients reported by Fage & Warsap (ref. 1) since it was not prevented despite the fact that it was detected.

In carrying out the present investigation, the blockage correction was consistently applied in smooth incident flow to both the pressure coefficient and the drag coefficient. Every effort to reduce the surface roughness and to prevent leakage was further undertaken. In addition, the freestream

leakage was further undertaken. In addition, the freestream turbulence of the smooth incident flow was practically maintained at an intensity equal to that in an empty wind-tunnel test section. The pressure distribution, the separation angle and the drag coefficient measured here in smooth incident flow under these controlled conditions *are generally consistent with results reported in other studies at corresponding subcritical Reynolds numbers* as indicated by the comparison analysis conducted above. Achievement of a better quantitative agreement among the various results is, in practice, precluded as long as differences in the blockage coefficient, surface roughness, freestream turbulence and leakage are present, and in view of the inherent limitation of the blockage correction. In conclusion, *the results obtained in this study in smooth incident flow represent an aceptable reference for gauging the effect of turbulence.*

6. RESULTS IN TURBULENCE INCIDENT FLOW

6.1 Incident Turbulence

Turbulent incident flow was obtained by superimposing freestream turbulence on the smooth flow using a turbulence-generating grid, as previously mentioned. In order to determine the positioning of the cylinder behind the grid, the evolution of the mean velocity defect and axial turbulent velocity downstream of the grid was surveyed in the absence of the cylinder. The turbulent flow behind the grid with the cylinder absent is viewed as the background turbulent flow as far as the cylinder is concerned. Comprehensive hot-wire measurements of the background turbulent flow were conducted over a half-mesh interval off the grid centerline (viz., midmesh centerline) at increasing distances downwind of the grid. These measurements were carried out at three different freestream velocities within the range corresponding to that used in the presence of the cylinder behind the grid, viz., at freestream velocities U_∞ = 4.9, 11.7 and 19.5 m/s which correspond to cylinder-diameter Re = 5.2×10^4, 1.25×10^5 and 2.09×10^5 (see Sec. 4 and App. III). Recall that the freestream velocity is the uniform velocity monitored upwind of the grid. It should further be noted that the grid centerline corresponds to the cylinder stagnation streamline, viz., the x-axis (vid., Fig. 2.2). The results of this investigation of the background turbulent flow are reported elsewhere in ref. 11. However, those results directly pertinent to the positioning of the cylinder downwind of the grid are briefly reviewed herein.

In determining the positioning of the cylinder behind the grid, the following criteria were applied to the background turbulent flow: (1) lateral uniformity in the background mean velocity $\overline{U}_b$, i.e., negligible mean velocity defect; (2) lateral homogeneity in the background axial turbulence intensity; (3) a level of background axial turbulence intensity smaller than 5%; (4) varying level of background axial turbulence intensity at given freestream velocity at that position behind the grid where the cylinder was to be located; and, (5) a turbulence intensity smaller than 10% in the presence of the cylinder at that distance upwind of it where the stretching action starts (i.e., at the front end of the amplification range, ref. 5). Examination of the lateral uniformity in the background mean velocity $\overline{U}_b$ was performed by referring it to the uniform freestream velocity U_∞, i.e., $\overline{U}_b/U_\infty$. Similarly, the background axial turbulence intensity was defined in terms of the uniform freestream velocity by

$$Tu_b = u_b'/U_\infty \ , \qquad (6.1)$$

where u_b' is the rms value $(\overline{u_b^2})^{1/2}$ of the background axial turbulent velocity.

The foregoing first three conditions were reasonably met starting from a distance downstream of the grid of about 9 mesh lengths (9M = 57.15 cm (22-1/2 in), where mesh M = 6.35 cm (2-1/2 in), see Sec. 2.3). For instance, the lateral variation over a half mesh in both the dimensionless background mean velocity and axial turbulence intensity was smaller than 5% at 9.6 mesh lengths (9.6M = 60.96 cm (24 in)) and reduced to less than 2% at 17.4 mesh lengths (17.4M = 110.50 cm (43-1/2 in)) behind the grid. In view of this negligible defect in the mean velocity and the acceptable lateral homogeneity in the axial turbulence intensity, their values along the grid centerline (midmesh centerline) were taken as representative of the background turbulent flow. The background axial turbulence intensity Tu_b along the grid centerline at the two aforementioned distances behind the grid was smaller than about 5 and 3%, respectively, at all freestream velocities of interest.

In order to evaluate the effect of varying background axial turbulence intensity upon the pressure distribution at given cylinder-diameter Reynolds number (or corresponding freestream velocity), positioning of the cylinder at several distances behind the grid was necessary. Based on the variation of the background axial turbulence intensity along the grid centerline, the cylinder was positioned at 10, 17.5 and 25 mesh lengths (10M, 17.5M, 20M = 63.50, 111.13, 158.75 cm (25, 43-3/4, 62-1/2 in)) behind the grid. In terms of the cylinder radius R (7.94 cm), the grid was located at distances of 8, 14 and 20R upwind of the cylinder stagnation point, i.e., at $\tilde{x}_g$ = 8,14, and 20. The positions of the cylinder stagnation point behind the grid are referred to as the test positions while the corresponding grid locations upwind of the cylinder are called the grid positions.

Variations of the background axial turbulence intensity Tu_b with increasing freestream velocity U_∞ and corresponding cylinder-diameter Reynolds number Re at the three cylinder test positions are displayed in Fig. 6.1. The background axial turbulence intensity exhibits an almost slightly linear decrease at the first two test positions (10M, 17.5M) from about 4 to 3.5% and 2.7 to 2.5%, respectively, with increasing freestream velocity (or corresponding cylinder-diameter Reynolds number). At the third test position (25M), it remained at an almost constant level of about 2.1% at all freestream velocities. Simultaneously,

the background axial turbulence intensity diminished with farther test position at given freestream velocity. Thus, *the background turbulence intensity met the required conditions.*

In producing the background turbulence, attention was further paid to obtain at the test positions turbulent energy primarily concentrated at scales smaller than the cylinder diameter and simultaneously larger than the neutral scale of the present stagnation flow. Concentration of turbulent energy at scales smaller than the diameter of the cylinder was sought to ensure its exposure to oncoming turbulent flow. Oncoming flow in which turbulence is mainly present at scales much larger than the diameter of the cylinder is, as a matter of fact, perceived by the latter as smooth incident flow. The need for turbulence at scales greater than the neutral scale of the stagnation flow stems from the fact that this is that particular turbulence that undergoes amplification according to the vorticity-amplification theory.

The scale structure of the background turbulence is characterized by its longitudinal integral scale Λ_b. Computation of the integral scale was accomplished by deducing it from the one-dimensional energy spectrum E(n) (n denotes frequency) of the axial turbulent velocity according to the relationship (ref. 42, p. 65)

$$\Lambda_b = (\bar{U}_b/4\overline{u_b^2})E(0) \ , \qquad (6.2)$$

in which $\bar{U}_b$ and $\overline{u_b^2}$ are the background mean velocity and the mean-square value of background axial turbulent velocity at the test position, respectively. The background mean velocity at the test position is, in practice, equal to the uniform freestream velocity by continuity condition, viz., $\bar{U}_b = U_\infty$, since it was measured in the absence of the cylinder. In the foregoing relationship, E(0) is the value of the energy spectrum at zero frequency (at n = 0) which was obtained by extrapolation. The estimated error in determining the integral scale amounts to about ±5% owing to the inevitable arbitrariness associated with the extrapolation of the energy spectrum to zero frequency.

The dependence of the background turbulence longitudinal integral scale at the test positions upon the freestream velocity was first inspected. To this end, the variations of this integral scale with increasing freestream velocity U_∞ and/or corresponding cylinder-diameter Reynolds number Re are displayed in Fig. 6.2. The integral scale made dimensionless in terms of the grid mesh-viz., Λ_b/M-is shown in this figure. A similarly linear increase with higher

freestream velocity (or corresponding cylinder-diameter Reynolds number) is exhibited by the background turbulence longitudinal integral scale at all three test positions. Recall that the grid mesh was constant.

In order to assess the overall similarity of the turbulence produced by the present grid to that generated by an ordinary square-mesh grid, the evolution of the longitudinal integral scale with downstream distance from the grid was surveyed as reported in ref. 11. The growth of the integral scale with distance behind the grid was reasonably approximated by a straight line. A similar approximately linear increase in the longitudinal integral scale is generally found downstream of an ordinary square-mesh grid of stable solidity (refs. 43,44,45). It should be noted that an exact linear increase implies complete self-preservation. On the other hand, a power-low growth for the integral scale behind a square-mesh grid of unstable solidities of 0.34 and 0.44 is proposed in ref. 9.

As far as the exposure of the cylinder to oncoming turbulent flow is concerned, the ratio of the background turbulence longitudinal integral scale to the cylinder diameter Λ_b/D at the test positions was examined. Variations of this ratio with increaseing freestream velocity U_∞ and/or corresponding cylinder-diameter Reynolds number Re are also portrayed in Fig. 6.2. The integral scale was consistently much smaller than the cylinder diameter at all test positions and freestream velocities. At the same time, the integral scale displayed a similarly linear increase with higher freestream velocity (or corresponding cylinder-diameter Reynolds number) at each test position. The linear increase in the integral scale amounted from 0.208 to 0.261D, 0.168 to 0.216D, and 0.208 to 0.261D as the test position was at 10, 17.5 and 25M, respectively, downstream of the grid. Thus, *background turbulence was supplied at scales that ensure the exposure of the cylinder to oncoming turbulent flow.*

The ratio of the background turbulence longitudinal integral scale to the neutral scale of the stagnation flow Λ_b/λ_o was next scrutinized at each test position to determine as to whether oncoming turbulence was concentrated at scales susceptible to undergoing amplification by stretching. Variations of this ratio with increasing Reynolds number Re are shown in Fig. 6.3. Note that the neutral scale at all five Reynolds numbers of interest is tabulated in this figure for convenience's sake. The background turbulence longitudinal scale was consistently larger than the neutral scale at all three test positions. It ranged from about 8.98 to $25.04\lambda_o$, 12.18 to $31.46\lambda_o$, and 15.07 to $38.05\lambda_o$ as the cylinder test position was farther from the

grid at 10, 17.5 and 25M, respectively. *These results indicate that background turbulence suitable to experiencing amplification by stretching was produced.*

Turbulence approaching a body experiences amplification starting from a certain upwind axial distance whose extent is determined by the stretching action. The axial turbulence intensity, based on the freestream velocity U_∞, at the front end of this amplification range is defined as the critical turbulence intensity as far as the turbulence amplification is concerned. Thus, the critical turbulence intensity Tu_c is given by

$$Tu_c = u'_{min}/U_\infty \ , \qquad (6.3)$$

where u'_{min} is the minimum rms value $(\overline{u^2}_{min})^{\frac{1}{2}}$ attained by the axial turbulence velocity prior to its amplification. The critical turbulence intensity and the axial extent of the amplification range depend upon the test position, i.e., upon the distance between the cylinder and the grid. In order to detect the position of minimum turbulence intensity, the evolution of the rms value of the axial turbulent velocity along the stagnation streamline (x-axis) was monitored by means of a single hot wire for each grid position over the entire Reynolds-number range of interest. Once this upwind position, denoted herein by $\tilde{x}_{min}$, was located, the critical turbulence intensity was computed according to Eq. (6.3).

Variations of the critical turbulence intensity Tu_c with increasing cylinder-diameter Reynolds number Re for the three grid positions are portrayed in Fig. 6.4. The critical turbulence intensity was consistently larger than that of the background turbulence owing to the presence of the cylinder, but yet smaller than 10% as desired. Its level ranged from about 7 to 6.7%, 4.8 to 4.4%, and 3.5 to 2.5% as the grid was positioned at $\tilde{x}_g$ = 8,14 and 20, respectively. A linear decay in the critical turbulence intensity with greater Reynolds number was obtained for each grid position. The upwind axial extent $\tilde{x}_{min}$ of the amplification range was the same at all Reynolds numbers for given grid position and it was larger as the grid was installed farther from the cylinder as indicated in Fig. 6.4. It increased from 1.6 to 2.2 and to 2.5R (12.70, 17.50, 19.84 cm (5, 6.9, 7.8 in)) as the grid was positioned farther from the cylinder at $\tilde{x}_g$ = 8,14 and 20, respectively. It is thus apparent that the stretching mechanism acts over a larger distance upwind

of the cylinder as the critical turbulence intensity is smaller at given Reynolds number.

6.2 Mean Surface Pressure Distribution

The mean surface pressure distribution in turbulent incident flow was measured for each of the three upwind turbulence-generating grid positions ($\tilde{x}_g$ = 8,14,20) at the same five subcritical Reynolds numbers as in smooth incident flow, viz., at Re = $5.2\text{x}10^4$, $9.4\text{x}10^4$, $1.25\text{x}10^5$, $1.67\text{x}10^5$, $2.09\text{x}10^5$. Computation of the surface mean pressure coefficient was accomplished by means of Eq. (3.2). No blockage correction was applied to the freestream velocity, the Reynolds number and the pressure coefficient, as earlier mentioned, in view of the significant change in the cylinder drag coefficient with varying Reynolds number. The measured pressure coefficient C_p' in turbulent incident flow and its ratio to that measured in smooth incident flow C_p'/C_p at each Reynolds number Re and azimuthal angle θ are given in Table A.VI.1 in App. VI. In addition, the grid position $\tilde{x}_g$, the background turbulence intensity Tu_b and the dimensionless background turbulence longitudinal integral scale based on the cylinder diameter Λ_b/D at each test position, the critical turbulence intensity Tu_c and the position upwind of the cylinder where it was detected $\tilde{x}_{min}$ are tabulated in this table for each case. The distributions of the pressure coefficient C_p' in turbulent incident flow with increasing peripheral angle θ over half of the cylinder at the five subcritical Reynolds numbers are shown in Figs. 6.5 to 6.9. Variations of the pressure coefficient for all three upwind grid positions at a single Reynolds number are portrayed in each figure. In addition, the distributions of the pressure coefficient C_p measured (uncorrected) in smooth incident flow at the same Reynolds numbers are depicted in these figures for comparison's sake.

In order to point out the effect of amplified turbulence upon the pressure distribution, it is relevant to examine the changes within its three regions. These three regions are: (1) the favorable pressure gradient region which extends from the stagnation point up to the point of minimum pressure θ_m'; (2) the adverse pressure gradient region which stretches from the point of minimum pressure up to the starting point of the base region θ_s'; and, (3) the base region which extends from the base region starting point to the base point θ_b.

The angular position of minimum pressure was deduced from the measured pressure distribution. In deducing θ'_m, the estimated error amounted to about ±4% in view of the inherent sensitivity associated with the detection of this inflection point and the lack of more data points within its immediate vicinity. The starting point of the base region was taken, as in smooth incident flow, at that peripheral angle where a distinct trend toward a leveling off in the surface pressure was observed. A second condition applied in estimating this angle was a difference up to about 15% between the pressure coefficient at this point and the base pressure coefficient C'_{pb} (C'_p at $\theta_b = 180°$). This criterion was used in view of the slight variation of the surface pressure within this region and the selection of the base pressure coefficient as characteristic of the entire base region (see Sect. 4). The estimated error in approximating θ'_s is about ±2 to 4% considering the relatively arbitrariness in determining the starting point of the levelling off in the surface pressure.

The starting point of the base region θ'_s represents a reasonable approximation of the separation angle since it indicates the point of boundary-layer flow detachment which corresponds to the position of zero mean skin friction (ref. 46). Such a correspondence between the starting point of the base region and the position of zero mean skin friction was found for a relatively rough cylinder (relative surface roughness k/D of $1.1\text{x}10^{-3}$ to $4.5\text{x}10^{-3}$, i.e., about 69 to 281 greater than in the present test) in smooth incident flow at subcritical Reynolds numbers ($1.0\text{x}10^5$, $1.3\text{x}10^5$, $1.7\text{x}10^5$, $2.4\text{x}10^5$) and at higher critical and supercritical Reynolds numbers ($4.3\text{x}10^5$, $6.5\text{x}10^5$, $3.0\text{x}10^6$, ref. 27). It should be noted that the surface roughness generally affects the pressure distribution and the separation in a manner similar to the freestream turbulence. Both the angular positions of the minimum pressure θ'_m and the starting point of the base region (or separation angle) θ'_s are marked off in Figs. 6.5 to 6.9 and listed in Table A.VI.2, App. VI. Note that their counterparts in smooth incident flow, θ_m and θ_s, are given in Table A.VI.3, App. VI, for convenience's sake.

Ideally, the penetration of amplified turbulence into the boundary layer induces lower (more negative) pressure in the favorable and adverse pressure gradient regions and higher (less negative) pressure in the base region. The differentiation between the pressure distributions in turbulent and smooth incident flows in these three regions becomes more pronounced as the grid is closer to the

cylinder-i.e., with higher background and/or critical turbulence intensity-and with increasing Reynolds number. These trends are by and large discerned in Figs. 6.5 and 6.9. In discussing below the changes and trends in the pressure distribution within these three regions, allowance was made for the associated inevitable experimental uncertainty.

6.3 Favorable Pressure Gradient Region

The distributions of the pressure coefficient in turbulent and smooth incident flows within the favorable pressure gradient region started parting company at an azimuthal angle ranging between 20 and 40° depending upon the particular Reynolds number-grid position combination as observed in Figs. 6.5 to 6.9. This differentiation between these two types of pressure coefficient distributions occurs at a smaller angle-viz., closer to the stagnation point-as the Reynolds number is larger. With further increase in the peripheral angle, the pressure coefficient in turbulent incident flow gradually became smaller (more negative) than its counterpart in smooth incident flow till their difference reached a maximum in the neighborhood of the point of minimum pressure. The rate of decrease in the pressure coefficient in turbulent incident flow was consistently greater than that in smooth incident flow. This decrease was steeper at lower Reynolds numbers (5.2×10^4, 9.4×10^4) when the grid was closer to the cylinder. The effect of the grid position diminished with increasing Reynolds number. An identical steep decrease in the pressure coefficient was obtained for all three grid positions at the higher Reynolds number (1.67×10^5, 2.09×10^5) as shown in Figs. 6.8 and 6.9. Thus, *the penetration of turbulence into the boundary layer induces along the front of a cylinder a more favorable pressure graident than in smooth incident flow.*

6.4 Minimum Pressure

A more favorable pressure gradient leads to a lower (more negative) minimum pressure and to a rearward shift in its angular position. Examination of these changes in the minimum pressure is of prime concern in view of its role in determining the development of the adverse pressure gradient region and, consequently, the inception of separation and the base pressure. Variations of the minimum pressure coefficient C'_{pm} in turbulent incident flow for all grid positions and of its counterpart C_{pm} in smooth incident flow with increasing Reynolds number are depicted in Fig. 6.10, while their values are listed in Tables A.VI.2 and A.VI.3, App. VI, respectively. Values of the minimum pressure coefficient in turbulent incident flow were estimated from the

pressure coefficient distributions shown in Figs. 6.5 to 6.9. Whenever no direct measurement was performed at the corresponding angular position, the minimum pressure coefficient was interpolated from the pressure coefficient distributions as annotated in Table A.VI.2, App. VI. Inspection of the variations of the minimum pressure coefficient reveals a distinct opposite behavior in smooth and turbulent incident flows. The minimum pressure coefficient in smooth incident flow was constantly higher (less negative) than in the latter flow and slightly increased (became less negative) with increasing Reynolds number. In turbulent incident flow, on the other hand, the minimum pressure coefficient decreased (became more negative) with increasing Reynolds number for each grid position. The reduction in the minimum pressure coefficient was larger as the grid was closer to the cylinder, i.e., with higher background and/or critical turbulence intensity.

Indication of the degree to which the turbulence reduced the minimum pressure coefficient is supplied by the ratio of the minimum pressure coefficient in turbulent incident flow to its counterpart in smooth incident flow C'_{pm}/C_{pm}. The values of this ratio are tabulated for each case in Table A.VI.2, App. VI. Variations of this ratio with increasing Reynolds number for all three grid positions are portrayed in Fig. 6.11. The decrease in the minimum pressure coefficient in turbulent incident flow C'_{pm} ranged from 1.12 to 2.61 times depending upon the particular Reynolds number-grid position combination. This demonstrates that the minimum pressure coefficient in turbulent incident flow was more negative than in smooth incident flow at all Reynolds numbers and for all grid positions, i.e., always $C'_{pm} < C_{pm}$. It should further be noted that the minimum pressure coefficient attained a constant value of about -2.45 at the highest subcritical Reynolds number of 2.09×10^5 for all three grid positions.

Further examination of the pressure coefficient distributions shown in Figs. 6.5 to 6.9 indicates that the reduction in the minimum pressure coefficient in turbulent incident flow was accompanied, as previously mentioned, by a rearward shift in its angular position. Variations of the angular position of the minimum pressure coefficient in both turbulent and smooth incident flows-viz., θ'_m and θ_m, respectively-with increasing Reynolds number are portrayed in Fig. 6.12. The point of minimum pressure coefficient in smooth incident flow was monitored at an angle of about 70° at all Reynolds numbers (see Sect. 5.1). In turbulent incident flow, on the other hand, the point of minimum pressure coefficient gradually shifted rearward from 70 to a

maximum of 80° with increasing Reynolds number for all grid position. This maximum aft shift occurred at smaller Reynolds numbers when the grid was closer to the cylinder. Thus, the interaction of turbulence with the boundary layer induces at each Reynolds number a finite downstream shift in the angular position of minimum pressure coefficient whose measure depends upon the intensity and scales of the background turbulence.

Reduction in the minimum pressure coefficient and its manifestation at azimuthal angles between 70 and 90° are generally characteristic of pressure distributions on a smooth cylinder in a smooth incident flow at higher critical, supercritical and transcritical Reynolds numbers i.e., at Re > 2-2.5x10^5 (refs. 19,21,31,33,34,47,48,49,50). In a smooth incident flow at these higher Reynolds numbers, the diminution in the minimum pressure and its rearward shifting are accompanied by a lengthening of the adverse pressure gradient region, a shortening of the base region and, ultimately, an aft shift in the separation angle. *One can, therefore, expect a similar behavior at subcritical Reynolds numbers in a turbulent incident flow.*

6.5 Adverse Pressure Gradient Region

The difference between the pressure distributions in turbulent and smooth incident flow is prominent within the adverse pressure gradient region as noticed in Figs. 6.5 to 6.9. Particularly noticeable is the longer streamwise extent of this region in turbulent incident flow. Variations of the angular extent of this region with increasing Reynolds number in turbulent incident flow for all three grid positions and of that in smooth incident flow are depicted in Fig. 6.13. The angular extent was approximated by the arc between the base region starting point and the minimum pressure point, i.e., by $\theta'_{sm} = \theta'_s - \theta'_m$ and $\theta_{sm} = \theta_s - \theta_m$ in turbulent and smooth incident flows, respectively. Their values are summarized in Tables A.VI.2 and A.VI.3, App. VI. This region extended in turbulent incident flow over an arc ranging from 15 to a maximum of 50° with increasing Reynolds number and depending upon the particular grid position. In smooth incident flow, on the other hand, this region stretched at all Reynolds numbers over a constant arc of about 10°.

The variation of the streamwise extent of the adverse pressure gradient region with higher Reynolds number and with closer grid position is, as a matter of fact, similar to that of the minimum pressure point. At each Reynolds number, the adverse pressure gradient region broadened as the grid was closer to the cylinder, i.e., as the intensity

of the background turbulence was higher and its integral scale was smaller. Simultaneously, this region asymptotically attained a maximum extent of 50° with increasing Reynolds number for all grid positions. The attainment of this maximum extent depends, as for the minimum pressure point, upon the Reynolds number-grid position combination. When the grid was closer to the cylinder, it was reached at lower Reynolds numbers as seen in Fig. 6.13. *This widening of the adverse pressure gradient region necessarily leads to a shorter base region* similarly to that found at higher Reynolds number in a smooth incident flow (refs. 19,21,31,33,34,47,48,49,50).

The pressure coefficient in turbulent incident flow was smaller (more negative) throughout the entire adverse pressure gradient region (at Re = 5.2×10^4 and 9.4×10^4 with the grid at $\tilde{x}_g = 20$) or throughout most of it (all the other cases) than its counterpart at corresponding angles and the same Reynolds numbers in smooth incident flow as seen in Figs. 6.5 to 6.9. Note that the corresponding angular positions in the smooth incident flow are already in the base region. Illustration of the decrease in the pressure coefficients in turbulent incident flow with respect to their counterparts in smooth incident flow is provided by their ratios C_p'/C_p tabulated in Table A.VI.1, App. VI. The relatively large negative pressure in the adverse pressure gradient region is consequent upon the prevailing much smaller minimum pressure. At the same time, this large negative pressure is associated with the broadening of this region. As the pressure is more negative, a longer distance is needed to attain the much higher (less negative) base pressure.

Examination of the variation in the pressure coefficient with grid position at given Reynolds number reveals that it was smaller (more negative) as the grid was closer to the cylinder. This trend, however, faded gradually away with increasing Reynolds number. At the highest subcritical Reynolds number of 2.09×10^4, for instance, the pressure distributions for all three grid positions practically collapsed onto a single curve as observed in Fig. 6.9. This indicates that the effect of turbulence upon the lengthening of the adverse pressure gradient is confined within a finite range with higher Reynolds number regardless of the grid position.

Further careful inspection of the pressure coefficient variations reveals the probable existence of a relatively short flat zone around 90 to 100° at Re = 5.2×10^4 and 9.4×10^4 with the grid at $\tilde{x}_g = 8$ and 20, respectively, as observed in Figs. 6.5 and 6.6. Such a short plateau, which

is generally found in the adverse pressure gradient region at higher critical and supercritical Reynolds numbers indicates the occurrence of a short laminar separation bubble followed by transition and reattachment to a turbulent boundary layer and turbulent separation (refs. 47,48,51). One can thus infer that a short laminar separation bubble transpired, in all likelihood, in these two cases. In all the other cases, on the other hand, a flat zone or a distinct drend toward its manifestation were not detected. The absence of a laminar separation bubble signifies realization of direct transition from a laminar to a turbulent boundary layer ahead of separation.

6.6 Base Region

The effect of the penetration of turbulence into the boundary layer is distinctly manifested in the contrast between the characteristics of the base region in turbulent and smooth incident flows. Differences between the base regions include a shorter extent and, in most cases, a less negative (or higher) pressure in turbulent incident flow as observed in Figs. 6.5 to 6.9.

Variations of the angular extent of the base region with increasing Reynolds number in turbulent incident flow for all three grid positions and of that in smooth incident flow are portrayed in Fig. 6.14. This angular extent was estimated by the arc between the base point and the base region starting point (or separation angle), i.e., by $\theta'_{bs} = \theta_b - \theta'_s$ and $\theta_{bs} = \theta_b - \theta_s$ in turbulent and smooth incident flows, respectively. Their values are listed in Tables A.VI.2 and A.VI.3, App. VI. The base region decreased in turbulent incident flow from an arc of 95 to 50° with higher Reynolds number and depending on the grid position consequent upon the corresponding lengthening of the adverse pressure gradient region. In smooth incident flow, on the other hand, the base region extended over a constant arc of about 100° at all Reynolds numbers. The shrinking of the base region was greater at each Reynolds number as the grid was closer to the cylinder and, at the same time, the minimum extent of 50° was attained asymptotically for all grid positions with higher Reynolds number. Hence, the shortening of the base region is constrained within a finite range similarly to the rearward shift of the minimum pressure point and the widening of the adverse pressure gradient region. *The immediate consequence of this shortening of the base region is an aft shift in the separation angle.*

The pressure in the base region was less negative in turbulent incident flow than that in smooth incident flow for almost all Reynolds number-grid position combinations as observed in Figs. 6.5 to 6.9. Only in four cases, viz.,

at the lowest Re = 5.2×10^4 for all three grid positions $\tilde{x}_g$ = 8,14,20 and at Re = 9.4×10^4 with the grid at $\tilde{x}_g$ = 20, the pressure throughout the base region in turbulent incident flow was either about equal to or slightly more negative (up to about 10%) than that in smooth incident flow. One can attribute this more negative pressure to the peculiar behavior of the boundary layer in these four cases which is discussed later. The extent to which the turbulence induced a less negative pressure coefficient within the base region is expressed by the ratio to its counterpart in smooth incident flow C'_p/C_p given in Table A.VI.1, App. VI.

The base pressure C'_{pb}, which characterizes the almost constant pressure within the entire base region, plays a prime role in determining the drag coefficient and, therefore, its change in turbulent incident flow was examined. As a matter of fact, the base pressure coefficient supplies an immediate indication of the drag coefficient since the latter is smaller when the former is less negative and vice versa. The slight change in the pressure in the base region with respect to the base pressure amounted from -4 to roughly +15% depending upon the particular Reynolds number-grid position combination. Variations of the base pressure coefficient C'_{pb} in turbulent incident flow for all grid positions, along with that in smooth incident flow C_{pb}, with increasing Reynolds number are shown in Fig. 6.15. Their values are further summarized in Table A.VI.2 and A.VI.3, App. VI, for convenience's sake. A less negative base pressure coefficient was constantly obtained in turbulent incident flow except in the four cases previously mentioned, which are marked off by a flag in Fig. 6.15.

The base pressure coefficient in both incident flows increased (became less negative) with higher Reynolds number, with a greater increase in turbulent incident flow. This increase amounted in the latter flow to 51, 54 and 55% with increasing Reynolds number from 5.2×10^4 to 2.09×10^5 as the grid was positioned at $\tilde{x}_g$ = 8,14 and 20, respectively. On the other hand, the increase in the base pressure coefficient in smooth incident flow over the same Reynolds-number range was about 21%. It should further be noted that the base pressure coefficient in turbulent incident flow reached an upper limit of about -0.49 for all three grid positions at the same highest subcritical Reynolds number of 2.09×10^5. Recall that the minimum pressure coefficient attained its lowest value (most negative value; vid., Fig. 6.10) for all grid positions at the same Reynolds number.

The absolute value of the ratio of the base pressure coefficient in turbulent incident flow to its counterpart in smooth incident flow C'_{pb}/C_{pb} was next examined in order to point out the increase (less negative values) of the former. Variation of this ratio with increasing Reynolds number for all three grid positions is depicted in Fig. 6.16, while their values are given in Table A.VI.2, App. VI. The absolute value of the base pressure coefficient in turbulent incident flow amounted in most cases-viz., eleven out of fifteen-to about 62 to 92% of its counterpart in smooth incident flow depending upon the particular Reynolds number-grid position combination. *These less negative base pressure coefficients in turbulence incident flow necessarily induce smaller drag coefficients than in smooth incident flow at the same subcritical Reynolds numbers.* In the four cases earlier mentioned, which are indicated by a flag in Fig. 6.16, the base pressure coefficient in turbulent incident flow was, similarly to the pressure in the entire base region, about equal to or slightly more negative than that in smooth incident flow. Specifically, C'_{pb}/C_{pb} = 1.004 and 1.013 at Re = $5.2\text{x}10^4$ and $9.4\text{x}10^4$ with the grid at $\tilde{x}_g$ = 8 and 20, and C'_{pb}/C_{pb} = 1.085 and 1.105 at Re = $5.2\text{x}10^4$ with the grid at $\tilde{x}_g$ = 14 and 20.

The occurrence of a less negative base pressure coefficient in turbulent incident flow is associated with a concurrent diminution in the minimum pressure coefficient (more negative) as revealed by the distributions of the pressure coefficient portrayed in Figs. 6.5 to 6.9. It is thus apparent that the reduction in the minimum pressure, which induces a longer adverse pressure gradient region, an aft shift in the separation angle and a shorter base region, also leads to a less negative base pressure. This is demonstrated by the variation of the base pressure coefficient with decreasing minimum pressure coefficient shown in Fig. 6.17. The simultaneous increase in the base pressure coefficient (less negative) and decrease in the minimum pressure coefficient (more negative) with higher Reynolds number is indicated by an arrow in this figure. It is important to remark that the increase in the base pressure coefficient with decreasing minimum pressure coefficient is described by a unique linear variation for all Reynolds number-grid position combinations. As the minimum pressure coefficient decreased by about 53% (from -1.288 to -2.453), the base pressure coefficient became less negative by about 225% (from -1.090 to -0.484). Another aspect of interest is that the base pressure coefficient attained its smallest negative value as the minimum pressure coefficient reached its largest negative level. The existence of a linear correlation between these two pressure coefficients is of paramount significance in view of their major role in determining the separation angle and the drag coefficient. As the

minimum pressure is more negative and the associated base pressure is less negative, the separation point moves rearward and the drag coefficient becomes smaller.

It is further relevant to note the opposite variations of the base pressure coefficient as function of the minimum pressure coefficient in turbulent and smooth incident flows. To this end, the variation in the latter flow of the base pressure coefficient (C_{pb}) with changing minimum pressure coefficient (C_{pm}) is included in Fig. 6.17. It is also described by a straight line, but the slope is exactly opposite to that in turbulent incident flow. These two pressure coefficients became concurrently less negative in smooth incident flow, while in turbulent incident flow the base pressure coefficient became less negative as the minimum pressure coefficient was more negative. The simultaneous increase of both pressure coefficients in smooth incident flow with higher Reynolds number is also indicated by an arrow in Fig. 6.17. Thus, the penetration of turbulence into the boundary layer modifies completely the effect of minimum pressure upon the base pressure.

6.7 Pressure Rise Coefficient

A coefficient which provides a measure of the effect of turbulence upon the position of separation is the pressure rise across the adverse pressure gradient region (refs. 52, 53). This pressure rise is strongly dependent upon the boundary-layer characteristics and relatively insensitive to blockage, slenderness and end effects (ref. 34). An approximation of this pressure rise coefficient is supplied by the difference between the base and minimum pressure coefficients

$$C'_{pbm} = C'_{pb} - C'_{pm} \quad . \tag{6.4}$$

In computing this pressure rise coefficient, the slight change of the pressure in the base region was neglected and, hence, the pressure at the starting point of the base region was taken equal to the base pressure. Variations with increasing Reynolds number of the pressure rise coefficient C'_{pbm} in turbulent incident flow for all grid positions and of its counterpart C_{pbm} in smooth incident flow are portrayed in Fig. 6.18. At the same time, their values are listed in Table A.VI.2 and A.VI.3, App. VI.

The pressure rise coefficient in smooth incident flow was consistently smaller than that in turbulent incident flow and almost constant over the Reynolds-number range

of interest as seen in Fig. 6.18 (see also Table A.VI.3, App. VI). Its value ranged randomly between 0.164 and 0.191 (viz., a 16% variation) with varying Reynolds number. In turbulent incident flow, on the other hand, the pressure rise coefficient exhibited an almost 10 times increase with higher Reynolds number, viz., from 0.198 to a maximum of about 1.969. Specifically, the increase amounted to about 3.1, 6.2 and 9.7 times with increasing Reynolds number from 5.2×10^4 to 2.09×10^5 as the grid was positioned at $\tilde{x}_g = 8, 14$ and 20, respectively. A greater pressure rise coefficient was obtained at any given Reynolds number as the background turbulence intensity was greater and, at the same time, the integral scale of the background turbulence was smaller at the cylinder test position (viz., as the grid was closer to the cylinder). The pressure rise coefficient attained further asymptotically an upper limit of about 1.96 at the highest present Reynolds number of 2.09×10^5 regardless of the grid position similarly to the asymptotic behavior found for both the minimum and base pressure coefficients (vid., Figs. 6.10 & 6.15). Essentially, the variation of the pressure rise coefficient in turbulent incident flow for each particular Reynolds number-grid position combination is prescribed by the concomitant increase in the base pressure coefficient (less negative) and decrease in the minimum pressure coefficient (more negative).

It is important to notice that the pressure distributions on a nominally smooth cylinder in turbulent incident flow at comparably subcritical Reynolds numbers reported in refs. 26,33 & 54 reveal pressure rise coefficients of about the same magnitude as those obtained in the present experiment. The pressure rise coefficients deduced from the data given in these three studies is also displayed in Fig. 6.18 for comparison sake. Differences among the pressure rise coefficients obtained here and in these three investigations can, in all likelihood, be attributed to the different characteristics of the background turbulence in each case. Turbulence was produced in these three studies in a random fashion by means of ordinary square-mesh biplanar grids without attempting to adequately control the scale distribution of turbulent energy. As a result, both the background turbulence intensity and longitudinal integral scale are generally different from those in the present work. Herein, background turbulence was specifically produced in a controlled fashion by means of a grid consisting of parallel vertical rods with due attention paid to ensure its simultaneous concentration at scales smaller than the cylinder diameter and greater than the neutral scale of the stagnation flow. In order to underscore the differences in the background turbulence, its characteristics-viz., turbulence intensity Tu_b, longitudinal integral scale referred

to cylinder diameter Λ_b/D and to neutral scale of the stagnation flow Λ_b/λ_o-at the test positions in the present experiment and in the foregoing three studies are summarized in Table 3 below. The background turbulence intensity and longitudinal integral scale are reported in these investigations while the neutral scale of the stagnation flow was computed in each case according to Eq. (2.2).

TABLE 3. BACKGROUND TURBULENCE CHARACTERISTICS

Source	Ref.	Re ($\times 10^{-4}$)	Tu_b (%)	Λ_b/D	Λ_b/λ_o
Present Test		5.2-20.9	2.1-4.5	0.124-0.261	9.0-38.0
Mody & El-Sherbiny	26, Fig. 1 (b)	5.0	6.7	0.486	34.60
	(c)		9.2		
Batham	33, Fig. 2	11.1	12.9	0.50	53.02
		23.5			77.15
Surry	54, Fig. 3	3.38	14.7	4.40	257.5
		3.54	10.5	0.36	21.6
		3.62	10.0	4.30	260.4
		4.42	2.5	9.80	605.8

It should be noted that the pressure rise coefficient deduced from the data given in ref. 54 decreased and even became smaller than that in the present smooth incident flow as the background turbulence longitudinal integral scale was greater than the cylinder diameter (i.e., as $\Lambda_b/D > 1$) as observed in Fig. 6.18. As a matter of fact, the pressure distributions reported there (ref. 54, Fig. 3) exhibited in these cases an increasing resemblence to that typical in a smooth incident flow. This result substantiates the need to produce background turbulence at scales smaller than the diameter of the cylinder in order to ensure its exposure to an oncoming turbulent flow. Fulfillment of this condition in the present experiment is indicated by the constantly larger pressure rise coefficient in turbulent incident flow as seen in Fig. 6.18. Even in these four cases in which the base pressure in turbulent incident flow was more negative than that in smooth incident flow (vid., Figs. 6.15 & 6.16), the pressure rise coefficient was greater in the former flow.

The increase in the pressure rise coefficient caused by turbulence is further revealed by the ratio of this coefficient in turbulent incident flow to its counterpart in smooth incident flow C'_{pbm}/C_{pbm}. Variations of this pressure rise coefficients ratio with increasing Reynolds number for each grid position are depicted in Fig. 6.19, while their

values are tabulated in Table A.VI.2, App. VI. This ratio exhibits a similar variation with Reynolds number as the pressure rise coefficient in turbulent incident flow since its counterpart in smooth incident flow was in practice constant. The aspect of interest is that the increase in the pressure rise coefficient in turbulent incident flow with respect to that in smooth incident flow ranged from about 1.2 to a maximum of 11.8 according to each particular Reynolds number-grid position combination. Similarly to the pressure rise coefficient in turbulent incident flow, the maximum increase in the pressure rise coefficients ratio was reached asymptotically at the highest Reynolds number (2.09×10^5) independently of the grid position. The increase in the pressure rise coefficient with higher Reynolds number and its relatively large value (with respect to that in smooth incident flow) further indicates a rearward shift in the separation angle. In fact, as the pressure rise coefficient is greater, a larger aft shift in the separation angle is expected. It should further be noted that the streamwise extent of the base region, and the level of both the base pressure coefficient and the pressure rise coefficient obtained herein are generally of the same magnitude as those for a smooth cylinder in smooth incident flow at higher critical, supercritical and transcritical Reynolds numbers (refs. 19,21,31,33,34,47,48,49,50).

6.8 Turbulent Separation Angle

The separation angle θ_s' was taken at the starting point of the base region which corresponds to the boundary-layer detachment point (the point of zero mean shear stress at the wall), as earlier mentioned. Variation of the separation angle in turbulent incident flow with increasing Reynolds number for all three grid positions is depicted in Fig. 6.20. The laminar separation angle θ_s is also shown in this figure for comparison's sake. Separation angles ranging from about 85 to a maximum of 130° were obtained depending upon the particular Reynolds number-background turbulence combination. The increase in the separation angle is due to the transfer of turbulent momentum to the boundary layer which enables the flow to follow the cylinder contour for a longer distance.

The smallest rearward shift in the separation angle was found in these two cases in which the base pressure was more negative than in smooth incident flow, viz., at $Re = 5.2 \times 10^4$ with the grid at $\tilde{x}_g = 14$ and 20 (vid., Figs. 6.15 and 6.16). In these two cases, which are marked off by a flag in Fig. 6.20, separation angles of roughly 95 and 85°, respectively, were obtained. The maximum turbulent

separation angle of about 130° was attained asymptotically with increasing Reynolds number for all grid positions. This finite upper limit was reached at a lower Reynolds numbers as the grid was closer to the cylinder. For instance, it was obtained at $Re = 1.25 \times 10^5$ when the grid was positioned at $\tilde{x}_g = 8$ and at $Re = 2.09 \times 10^5$ with the grid at $\tilde{x}_g = 20$. A similar asymptotic behavior with increasing Reynolds number was exhibited by the other key characteristics of the pressure distribution, viz., by C'_{pm}, θ'_m, θ'_{sm}, θ'_{bs}, C'_{pb} and C'_{pbm}.

Corroboration of the separation angles deduced from the pressure coefficient distributions was next supplied by the dry-surface coating visualization. The visualization was conducted for a variety of Reynolds number-grid position combinations within the range used during the surface pressure survey. A sample of the separation angle indicated by the visualization is provided by three black-and-white still photographs given in Fig. 6.21. These stills were reproduced from a color movie so that the red separated flow region (the light area) and the blue attached flow region (the dark area) are marked off in the figure by R and B, respectively, as in the smooth indicent flow case. Turbulent separation angles of about 110, 115 and 120° at = 7.5×10^4 and 1.25×10^5 with the grid positioned at $\tilde{x}_g = 8, 14$ and 20, respectively, are distinctly observed in these stills. These separation angles are with about -2% of those obtained from the pressure distribution shown in Fig. 6.20. A similar correspondence within ±4%, at the most, was found for all other Reynolds number-grid position combinations. It is further important to stress that separation angles of about the same magnitude as those obtained here for a smooth cylinder in turbulent incident flow at subcritical Reynolds numbers are found in higher critical, supercritical and transcritical flow regimes for a smooth cylinder in a smooth incident flow (refs. 19,21,31,33,34,47,48,49,50).

Indication of the extent to which the penetration of turbulence into the boundary layer postpones the separation is given by the difference between the separation angles in turbulent and smooth incident flows $\Delta\theta'_s = \theta'_s - \theta_s$, which is also shown in Fig. 6.20 at each Reynolds number-grid position combination. The aft shift in the separation point caused by the turbulence amounted from 5 to 50° since the laminar separation angle was about 80° at all the present subcritical Reynolds numbers. It is, thus, apparent that *one can produce any desired aft shift in the separation point within this range by suitable control of Reynolds number-background turbulence combination.*

The separation point is essentially determined by the extent of the adverse pressure gradient region which, in turn, is governed by the pressure rise and base pressure coefficients. Variations of the angular extent of the adverse pressure gradient region (θ'_{sm}) and of the separation angle (θ'_s) with increasing pressure rise coefficient (C'_{pbm}), and of the separation angle with increasing pressure base coefficient (C'_{pb}) are displayed in Figs. 6.22, 6.23 and 6.24, respectively. The larger is the pressure rise coefficient and the less negative is the base pressure coefficient, the longer is the adverse pressure gradient region and the greater is the separation angle. At the same time, both θ'_{sm} and θ'_s reached asymptotically their maximum values with increasing Reynolds number as these pressure coefficients attained simultaneously their upper bounds. Their increase with higher Reynolds number is indicated by an arrow in these figures. It is next important to note that the variations of both θ'_{sm} and θ'_s are described by single similar curves for all Reynolds number-grid position combinations. The existence of such correlations permits one to determine at any given Reynolds number the extent of the adverse pressure gradient region and the separation angle based on the pressure rise and base pressure coefficients.

The aft shift in the separation angle beyond 90° necessarily causes a narrower wake. When the separation point is on the front of the cylinder ($\theta_s < 90°$), the wake is wider than the cylinder diameter, viz., $d_w > D$, where d_w denotes the wake width. As the separation point moves to the back of the cylinder ($\theta'_s > 90°$), the wake width becomes smaller than the cylinder diameter, viz., $d'_w < D$. Detailed mapping of the wake was not carried out because of time constraints of the present investigation. However, single hot-wire vertical traverses were conducted within the wake at a distance of 0.64D (10 cm (4 in)) downstream of the cylinder in smooth incident flow at a Re = 1.25×10^5 and in turbulent incident flow at the same Reynolds number with the grid at $\tilde{x}_g = 14$. The goal of these measurements was to detect the free-shear layer (or free streamline), according to the free-streamline model for the wake (ref. 21), and, hence, it was restricted to simply monitoring of the mean velocity variation. In this free-streamline model, the pressure on the wake boundary is assumed constant and equal to the base pressure from the separation point up to that point downwind where the wake boundary becomes parallel to the freestream and the pressure recovers to the freestream

value. It should be noted that the results of this survey supply soley a gross approximation of the wake boundary in view of the entrainment across the free-shear layers, the large transverse velocity fluctuations associated with the vortex shedding, and because of adopting the ideal free-streamline model. Nevertheless, they are indicative of the narrowing of the wake induced by the rearward shift of the separation point. A wake width about 33% larger than the cylinder diameter ($d_w \cong 1.33D$) was found in smooth incident flow when the separation angle $\theta_s \cong 80°$. In turbulent incident flow, when the separation angle $\theta_s' \cong 128°$ ($Re = 1.25 \times 10^5$, $\tilde{x}_g = 14$), the wake width reduced to about 86% of the cylinder diameter ($d_w' \cong 0.86D$) and, hence, it amounted to roughly 0.65 of its counterpart in smooth incident flow ($d_w'/d_w = 0.65$).

Simultaneously with the narrowing of the wake, turbulence induces a shorter wake formation region close behind the cylinder (viz., a shorter near wake), weakens the forming vortexes there, promotes the diffusion of the free-shear layers into the wake and, as a result, fosters a less negative base pressure. These strongly interrelated changes in the wake characteristics are caused by the drawing across the wake of fluid from the outer turbulent flow according to the entrainment mechanism proposed in ref. 55. The assumption is made that this mechanism, which was advanced based on data at Reynolds numbers of 10^3 to 10^4, applies to the present higher subcritical Reynolds numbers. Outer fluid entrained periodically along each side of the wake is of vorticity of opposite sign to that of the entraining shear layer since it bears vorticity from the other shear layer across the wake. This periodic entrainment along each side is due to the action of the growing vortex on the other side of the wake axis. The entrained fluid of oppositely-signed vorticity inhibits the increase in the reversed flow within the formation region as it weakens the forming vortex there, and it even cancels some circulation at the cylinder rear surface. As a result, the formation region becomes shorter.

The weakening of the forming vortexes is further enhanced by greater diffusion of the free-shear layers into the interaction region, i.e., into the region of the growing vortex downwind of the formation region. Increase in the turbulence of these layers, which is effected by the outer turbulent flow, is responsible for their stronger diffusion. This greater vorticity diffusion leads to less entrainment into the growing vortex and, hence, to more entrainment within the formation region. As a result, the scale of the formation region and the strength of the forming vortexes

are reduced. The diffusion of the free-shear layers and its effect upon the formation region are furthermore larger with increasing outer (or freestream) turbulence at given Reynolds number (ref. 55). The aspect of prime interest concerning the weakening of the forming vortexes is its effect upon the base pressure. As the strength of the forming vortices diminishes, the base pressure increases (becomes less negative). This is thus the mechanism responsible for the observed increase in the base pressure in turbulent incident flow.

Further examination of the variation of the separation angle with varying base pressure coefficient shown in Fig. 6.24 reveals that the latter increases from about -1.070 to -0.484 as the former shifts rearward from 85 to 130°. In other words, as the separation angle moves on the back of the cylinder and, consequently, the wake narrows, the base pressure becomes less negative. One then can infer that weakening of the forming vortices is more powerful in turbulent incident flow when the wake is narrower than the cylinder diameter. On the other hand, when the wake is wider than or roughly of the same width as the cylinder diameter (viz., at a separation angle smaller than or around 90°) the base pressure coefficient in turbulent incident flow was more negative or about equal to that in smooth incident flow (vid., Figs. 6.15, 6.16 and 6.24). It is suspected that the entrainment in these cases occurred primarily in the wake interaction region without strongly affecting the formation region.

6.9 Turbulent Separation Parameter

The increase in the pressure rise coefficient and the associated aft shift of the separation point are effected by the penetration of turbulence into the boundary layer. In considering the effect of turbulence upon them it is necessary to account for its intensity and scale structure. The latter is of crucial significance since only turbulent energy concentrated at scales greater than the neutral scale of stagnation flow and, at the same time, smaller than the cylinder diameter amplifies and interacts with the cylinder boundary layer.

Examination of the effect of turbulence intensity upon the increase in the pressure rise coefficient and the attendant aft shift of the separation angle was accomplished by introducing a turbulence parameter for each Reynolds number-turbulence situation. This turbulence parameter is given by the product of the square of a characteristic turbulence intensity (based on the freestream velocity) and the Reynolds number, viz., by Tu^2Re, (ref. 8, p. 546). In fact, this turbulence parameter is a measure of the ratio of

turbulent energy production (or turbulent momentum transport) to viscous momentum transport (transport of mean momentum due to the action of viscous stresses). At the same time, this turbulence parameter is the product of a characteristic turbulence intensity and a turbulent Reynolds number Re_t based on the rms value u' of turbulent velocity since $Tu^2Re = TuRe_t$, where $Tu = u'/U_\infty$, $Re_t = u'D/\nu$ and $u' = (\overline{u^2})^{\frac{1}{2}}$.

Variations of the pressure rise coefficient C'_{pbm} and turbulent separation angle θ'_s as function of this turbulence parameter are portrayed in Figs. 6.25 and 6.26, respectively. Their variations with the turbulence parameter expressed in terms of the background turbulence intensity at the test position Tu_b^2Re and the critical turbulence intensity Tu_c^2Re are shown in each figure for each grid position ((a) and (b) in Figs. 6.25 and 6.26). In addition, their changes with these two turbulence parameters at given Reynolds number with varying grid position (or test position) is portrayed in these two figures by dashed curves. The relatively high values of either turbulence parameter-viz., $Tu_b^2Re = 87$ to 256 and $Tu_c^2Re = 64$ to 949, which are tabulated in Table A.VI.2, App. VI-indicate that the flow is dominated by turbulence and that the viscous effects are negligible. Both C'_{pbm} and θ'_s exhibit an almost similar continuous increase with either turbulence parameter for any grid position and at any given Reynolds number reflecting the increasing effect of turbulent momentum transfer to the boundary layer. At the present highest subcritical Reynolds number of 2.09×10^5, both C'_{pbm} and θ'_s attained asymptotically maximum values independently of the grid position. This limiting behavior attests to the finite effect of the amplified turbulence upon the increase in the pressure rise coefficient and the rearward shift of the separation angle.

The issue at stake is to account for the scale structure of the background turbulence in addition to its intensity. To this end, one can use the background turbulence longitudinal integral scale at the test position which is representative of the energy-containing eddies (see Sect. 6.1). The pressure rise across the adverse pressure gradient region is basically a function of the fluid properties (density ρ and dynamic viscosity μ), the rms value of background fluctuating velocity ($u'_b = (\overline{u_b^2})^{\frac{1}{2}}$) and the background turbulence longitudinal integral scale (Λ_b) at

the cylinder test position, the freestream velocity (U_∞), and the cylinder diameter (D). Thus,

$$p_b - p_m = F(\rho, \mu, u_b', \Lambda_b, U_\infty, D), \tag{6.5}$$

where the pressure at separation point is taken equal to the base pressure p_b, as previously mentioned, and p_m denotes the minimum pressure. These variables can readily be grouped in dimensionless terms as following:

$$C_{pbm}' = F\left(\frac{\Lambda_b}{D}, \frac{u_b'}{U_\infty}, \frac{\rho U_\infty D}{\mu}\right), \tag{6.6}$$

where the pressure rise coefficient across the adverse pressure gradient region

$$C_{pbm}' = \frac{p_b - p_m}{\frac{1}{2}\rho U_\infty^2}. \tag{6.7}$$

This functional relationship for the pressure rise coefficient can next be expressed in the form

$$C_{pbm}' = F\left(\frac{\Lambda_b}{\pi D} Tu_b Re^{\frac{1}{2}}\right), \tag{6.8}$$

in order to account for the neutral scale of the stagnation flow $\lambda_o = \pi D/Re^{\frac{1}{2}}$, and where $Tu_b Re^{\frac{1}{2}}$ is exactly the square-root of the turbulence parameter based on the background turbulence intensity earlier introduced. In terms of the neutral scale, the product of these two dimensionless parameters is given by $(\Lambda_b/\lambda_o)Tu_b$. The angular extent of the adverse pressure gradient region θ_{sm}' and the separation angle θ_s' are closely associated with and, as a matter of fact, determined by the pressure rise coefficient. One consequently can assume that they obey the same functional dependence and, hence,

$$\left\{ \begin{matrix} \theta_{sm}' \\ \theta_s' \end{matrix} \right\} = F\left(\frac{\Lambda_b}{\pi D} Tu_b Re^{\frac{1}{2}}\right). \tag{6.9}$$

The product of the two dimensionless parameters accounts at once for the intensity and integral scale of background turbulence at the cylinder test position, the

Reynolds number, the cylinder diameter, the neutral scale of the stagnation flow, and the transfer of turbulent momentum to the boundary layer through the square-root ot the turbulence parameter previously introduced. As a result, one can view the function given by the product of the dimensionless integral scale and the square-root of the turbulent parameter $(\Lambda_b/\pi D)Tu_b Re^{\frac{1}{2}}$ as a turbulent separation parameter or criterion for any given Reynolds number-background turbulence combination.

Variations of the pressure rise coefficient C'_{pbm}, the angular extent of the adverse pressure gradient region θ'_{sm} and the separation angle θ'_s with increasing turbulent separation parameter are portrayed in Figs. 6.27, 6.28 and 6.29, respectively. Examination of their variations reveals the existence of distinctly similar correlations between them and the turbulent separation parameter for each particular background turbulence (or grid position). The results over the entire Reynolds-number range collapse on single similar curves for each grid position. At given Reynolds number, C'_{pbm}, θ'_{sm} and θ'_s took on higher values as the intensity of the background turbulence was larger and, simultaneously, its integral scale was smaller, i.e., as the grid was closer to the cylinder. They further reach asymptotically an upper limit with increasing turbulence separation parameter regardless of the grid position.

The separation is determined by the pressure rise across the adverse pressure gradient region and, therefore, it is important to examine the change in the adverse pressure gradient with varying turbulence separation parameter $(\Lambda_b/\pi D)Tu_b Re^{\frac{1}{2}}$. An approximation of the average adverse pressure gradient is supplied by the ratio of the pressure rise coefficient to the angular extent of the adverse pressure gradient region C'_{pbm}/θ'_{sm} according to

$$\frac{1}{R}\frac{\partial p}{\partial \theta} \cong \frac{\rho U_\infty^2}{D}\frac{C'_{pbm}}{\theta'_{sm}}, \qquad (6.10)$$

where R is the cylinder radius and θ'_{sm} is measured in radians. This average adverse pressure gradient also provides an estimate for the shear stress gradient normal to the wall at separation. Another function whose change with the turbulence separation parameter is of prime concern is the ratio of the pressure rise coefficient to the separation angle C'_{pbm}/θ'_s (where θ'_s is in radians). This ratio is

essentially a measure of the effect of the pressure rise coefficient upon the position of turbulent separation and, hence, it can be viewed as a separation coefficient.

Variations of the average adverse pressure gradient and the separation coefficient as function of the turbulent separation parameter are displayed in Figs. 6.30 and 6.31, respectively. The values of $(\Lambda_b/\pi_D)Tu_bRe^{\frac{1}{2}}$, C'_{pbm}/θ'_{sm} and C'_{pbm}/θ'_s are further tabulated in Table A.VI.2, App. VI, for each Reynolds number-grid position combination. Both exhibit an identical change for each grid position. Their variations with increasing turbulent separation parameter are, in fact, similar to those of their components. The aspect of interest is that both the average adverse pressure gradient and separation coefficient are described over the entire subcritical Reynolds-number range by single correlations for each particular grid position.

The behavior of the average adverse pressure gradient (C'_{pbm}/θ'_{sm}) and the separation coefficient (C'_{pbm}/θ'_s), along with that of their components (C'_{pbm}, θ'_{sm} and θ'_s), with increasing turbulent separation parameter is similar to those of the other characteristics of the pressure distribution (C'_{pm}, θ'_m, θ'_{sm}, θ'_{bs}, C'_{pb} and C'_{pbm}) with higher Reynolds number. This general similar behavior of all these characteristics of the pressure distribution is the result of the change in the nature of the initial laminar boundary layer to partially or even fully turbulent effected by the amplified turbulence. The increase in the values of these characteristics up to certain plateaus is due to the penetration into the boundary layer of these energy-containing eddies within which the turbulent energy amplifies and which are, at the same time, of scales commensurate with the boundary-layer thickness. One cannot expect a continuous increase in the values of these characteristics with higher turbulent separation parameter and/or Reynolds number because of the inherent attendant increase in the size of the energy-containing eddies. As the scale of these eddies becomes larger, the amount of turbulent energy supplied to the boundary layer settles down at some constant level. Consequent upon attaining such a state of equilibrium, the values of the various characteristics of the pressure distribution reach finite upper limits with increasing turbulent separation parameter and/or Reynolds number. It should further be noted that one cannot expect to express the variations of the various characteristics of the pressure distribution by means of single correlations in terms of the turbulent separation parameter for all Reynolds number-background turbulence combinations. This is due to the evolution of the properties of turbulence and, particularly, its

amplification by stretching as it is conveyed by the mean flow toward the cylinder.

The important aspect of the various correlations based on *the turbulent separation parameter is that they provide an empirical method to estimate the turbulent separation angle and associated characteristics of the adverse pressure gradient region for any given Reynolds number-background turbulence combination in terms of solely two readily measurable properties of the background turbulence, the Reynolds number and the cylinder diameter.*

6.10 Mean Turbulent Drag Coefficient

The sectional mean turbulent drag coefficient C_{Dt} was computed for each Reynolds number-background turbulence (or grid position) combination by integrating the corresponding measured surface pressure distribution according to Eq. (3.3). This drag coefficient accounts solely for the form (or pressure) drag which, as a matter of fact, constitutes the major part of the total drag since the friction drag is negligible compared with the former as in smooth incident flow (refs. 2,18,19).

The mean turbulent drag coefficients for all fifteen Reynolds number-grid position cases are plotted as function of increasing Reynolds number in Fig. 6.32. For comparison's sake, the measured (uncorrected) laminar drag coefficients $C_{D\ell}$ over the same Reynolds-number range are also shown in this figure. Values of both drag coefficients and their ratio are further compiled in Tables A.VI.2 and A.VI.3, App. VI. The drag coefficient in both incident flows decreased with higher Reynolds number, with a much greater decrease in turbulent incident flow. As a matter of fact, the greater decrease of the drag coefficient in turbulent incident flow reflects the associated increase of the corresponding base pressure coefficient (vid., Fig. 6.15) and, hence, the variation of the former is essentially the mirror image of the latter.

The mean turbulent drag coefficient decreased from about 1.0 to 0.44, 1.13 to 0.43 and 1.14 to 0.43 with increasing Reynolds number from $5.2\text{x}10^4$ to $2.09\text{x}10^5$ as the grid was positioned at $\tilde{x}_g$ = 8,14 and 20, respectively. On the other hand, the laminar drag coefficient diminished over the same Reynolds-number range from about 1.07 to 0.93. Turbulent drag coefficients smaller than their laminar counterparts were, for the most part, obtained at each Reynolds number. These smaller drag coefficients are the result of the attendant increase in the base pressure coefficients (less negative).

Only in two cases in which the base pressure coefficient was more negative in turbulent incident flow than in smooth incident flow, viz., at the lowest $Re = 5.2 \times 10^4$ with the grid at $\tilde{x}_g = 14$ and 20 (vid., Fig. 6.15), the drag coefficient was greater by about 6 to 7% than its laminar counterpart. One can conjecture that these two slightly larger drag coefficients in turbulent incident flow are due to insufficient weakening of the forming vortices since the wake width was, in all likelihood, of about the same magnitude as the cylinder diameter according to the corresponding separation angles (95 and 85°). These two cases are marked off by a flag in Fig. 6.24 for convenience's sake. It is further important to note that the turbulent drag coefficient decreased to a minimum value of about 0.43 to 0.44 independently of the background turbulence (or grid position) at the highest present Reynolds number of 2.09×10^5. This asymptotic behavior of the turbulent drag coefficient with increasing Reynolds number is similar to that found for all the other characteristics of the pressure distribution.

The ratio of the turbulent drag coefficient to its laminar counterpart $C_{Dt}/C_{D\ell}$ was next inspected in order to point out the reduction of the drag coefficient induced by turbulence. Variations of this ratio with increasing Reynolds number for each grid position are depicted in Fig. 6.33, while their values are listed in Table A.VI.2, App. VI. Note that the two cases in which the turbulent drag coefficient was slightly greater than its laminar counterpart are also marked off by a flag in this figure. The turbulent drag coefficient amounted in most cases-viz., thirteen out of fifteen different Reynolds number-background turbulence cases surveyed-from about 97 to 46% of the laminar drag coefficient depending upon the particular Reynolds number-background turbulence combination. Larger reduction of the turbulent drag coefficient was generally found at each Reynolds number when the grid was closer to the cylinder, i.e., at higher intensity and, simultaneously, smaller integral scale of background turbulence. This notable diminution of the turbulent drag coefficient testifies to the energizing of the boundary layer consequent upon the penetration of turbulence into it.

It should further be noted that the turbulent drag coefficients obtained here at subcritical Reynolds numbers are generally of the same magnitude as those for a smooth cylinder in a smooth incident flow at higher critical, supercritical and even transcritical Reynolds numbers (refs. 19,34,47,48,50). *This correspondence of the drag coefficients, along with that of the separation points, indicates that the penetration of turbulence into the boundary layer induces overall properties similar to those found at much higher Reynolds numbers.*

The dependence of the drag coefficient upon the base pressure and pressure rise coefficients was next examined in view of their dominant role in determining its value. One can approximate the drag coefficient C_D in terms of the base pressure coefficient C_{pb} and the wake width d_w by means of the relationship (refs. 21,56)

$$C_D = (-C_{pb})(d_w/D), \qquad (6.11)$$

where D is the cylinder diameter. This relation is based on momentum consideration and the free-streamline model for the wake. Thus, the drag coefficient is linearly proportional to the absolute value of the base pressure coefficient and the wake width. A less negative base pressure induces a smaller drag coefficient. In turn, a less negative base pressure is necessarily associated with a more negative minimum pressure and, hence, with a larger pressure rise across the adverse pressure gradient region, as previously shown. One consequently expect also a linear reduction of the drag coefficient with increasing pressure rise coefficient.

The variation of the turbulent drag coefficient as function of the base pressure and pressure rise coefficients depicted in Figs. 6.34 and 6.35, respectively, confirm this linear dependence. In both cases, the change in the turbulent drag coefficient for all Reynolds number-grid position combinations is described by a straight line. A similar linear variation was found for the laminar drag coefficient $C_{D\ell}$ which is also shown in these two figures. Note that the decrease of the drag coefficient with increasing Reynolds number is indicated in these figures by an arrow. *The important aspect of these linear correlations is that they supply an immediate estimate of the drag coefficient for given base pressure coefficient and/or pressure rise coefficient.*

The use of Eq. (6.11) in estimating the drag coefficient hinges on knowing the wake width. Measurement of the latter is quite difficult owing to the entrainment across the free-shear layer and the transverse velocity fluctuations. A gross approximation of the wake width was, however, obtained at $Re = 1.25 \times 10^5$ with the grid at $\tilde{x}_g = 14$, as earlier described in Sect. 6.8. In applying Eq. (6.11) to this case, a drag coefficient of about 0.61 is obtained ($C'_{pb} = -0.711$ vid, Fig. 6.15 and Table A.VI.2, App. VI; and, $d'_w/D = 0.86$, see Sect. 6.8). At the same time, the mean turbulent drag coefficient deduced from the measured surface pressure distribution was 0.65 in the same case (vid., Fig. 6.31 and

Table A.VI.2, App. VI) and, hence, it was about 7% greater than that deduced by means of Eq. (6.11). This relatively reasonable agreement indicates that one can apply Eq. (6.11) to roughly approximate the mean turbulent drag coefficient. A poorer agreement was, on the other hand, found at the same Reynolds number in smooth incident flow. The measured laminar drag coefficient was about 1.05 (vid., Fig. 6.32), while that estimated according to Eq. (6.11) amounted to 1.25 (C_{pb} = -0.939, vid., Fig. 6.7 and Table A.VI.3, App. VI; and d_w/D = 1.33, see Sect. 6.8). Thus, the measured laminar drag coefficient was about 16% smaller.

Attempts to estimate the wake width according to Eq. (6.11) based on the measured values of C'_{pb} and C_{Dt} were only partially successful. In five cases (viz., at Re = 5.2×10^4 with the grid at $\tilde{x}_g$ = 8 and 14; at Re = 9.4×10^4 with the grid at $\tilde{x}_g$ = 14 and 20; and at Re = 1.25×10^5 with the grid at $\tilde{x}_g$ = 20) in which the observed separation angle was distinctly greater than 90°, the calculated values of the wake width were larger than the cylinder diameter (viz., d'_w/D varied between 1.01 and 1.07). It is conjectured that these larger values are due to the intrinsic limitations of the free-streamline model of the wake since the entrainment across the wake and its dependence upon the Reynolds number are not accounted for in this model. It is interesting to remark that a similar lack of agreement was found in smooth incident flow at higher supercritical Reynolds numbers (ref. 21).

7. DISCUSSION OF RESULTS

The separation angles and mean turbulent drag coefficients, along with the characteristics of the mean surface pressure distribution, obtained here for a smooth cylinder in turbulent incident flow at subcritical Reynolds numbers are by and large of the same magnitude as those found for a smooth cylinder in smooth incident flow at higher critical, supercritical and transcritical Reynolds numbers, as previously alluded to. In order to stress this striking similarity and its implication concerning the nature of the boundary layer, it is imperative to compare the present results with those reported at these higher Reynolds numbers.

The division of smooth flow about a smooth cylinder into four distinct regimes with increasing Reynolds number beyond 10^4 is associated with the nature of the boundary layer and the properties of the wake. Consequently, specification of these regimes in terms of Reynolds-number ranges depends on myriad interweaved characteristics, viz., magnitude and position of the minimum pressure, angular extent of the adverse pressure gradient region and the pressure rise across it, magnitude of the base pressure, laminar separation, occurrence of a laminar separation bubble followed by transition and reattachment to a turbulent boundary layer and turbulent separation, direct transition from a laminar to a turbulent boundary layer followed by turbulent separation, shear layer instabilities, narrowing of the wake and entrainment across it, vortex shedding frequency and associated Strouhal number, and the drag coefficient. In view of this complex dependence, which is not yet completely elucidated, the Reynolds-number ranges of these flow regimes are estimated based on the position of the separation point and the magnitude of the drag coefficient as briefly outlined hereinafter.

The subcritical flow regime extends to a Reynolds number of about 1.2×10^5 (ref. 47) or 2×10^5 (ref. 21) or even 2.5×10^5 (ref. 19). This flow regime is characterized by a laminar boundary layer with laminar separation around 80°, high negative base pressure, a relatively wide wake, and a drag coefficient approximately constant at values ranging between 1.20 and 0.90.

The critical (or lower transition) flow regime develops as the Reynolds number increases to about 5×10^5 (ref. 21) or 6×10^5 (ref. 47). In this flow regime, the laminar separation shifts initially to about 110° (ref. 47) with increasing Reynolds number as the flow is able to follow the body contour over a longer distance consequent upon a decrease in the friction forces. With further increase in the Reynolds

number, there appears a short laminar separation bubble in the adverse pressure gradient region followed by transition and reattachment to a turbulent boundary layer and turbulent separation at 130 to 140° (ref. 47) which is associated with a less negative base pressure and a narrower wake. In this flow regime, the drag coefficient drops quite rapidly from its nearly constant subcritical value to a minimum of about 0.30 (refs. 21,47) and even to 0.14-0.20 (refs. 48,50). This minimum drag coefficient is found at a critical Reynolds number of $3x10^5$ (ref. 47) or $5x10^5$ (refs. 21, 34,50).

The supercritical (or upper transition) flow regime extends between Reynolds numbers of $5-6x10^5$ and $2x10^6$ (ref. 47) or $3.5x10^6$ (refs. 19,21). Characteristic of this flow regime is the forward movement of the transition to a turbulent boundary layer which leads to the gradual extermination of the laminar separation bubble and, hence, to direct transition to a turbulent boundary layer at angles larger than 90° and even slightly smaller than 90°. As a result, the turbulent separation angle moves forward to around 120°, the wake slightly opens, the base pressure becomes more negative, and the drag coefficient increases to about 0.40 to 0.70 (refs. 21,47,48,50). It should be noted that both the critical and supercritical flows are highly sensitive to any flow disturbance.

Finally, the transcritical flow regime exists at Reynolds numbers greater than $2x10^6$ (ref. 47) or than $3.5x10^6$ (ref. 21). In this flow regime, the direct transition from a laminar to a turbulent boundary layer moves upstream on the front of the cylinder at angles smaller than 90° followed by turbulent separation on its back part. Transition occurs at angles ranging from 80 to about 20° with increasing Reynolds number and turbulent separation transpires at a nearly constant angle between 110 and 120°. The base pressure and the wake width remain at almost constant levels and, at the same time, the drag coefficient is approximately constant at values varying from 0.40 to 0.70 (refs. 21,47,48,50).

It is apparent that the boundaries among these four flow regimes are loosely delineated and that no consensus concerning the Reynolds-number range of each flow regime has yet been reached. This is due to the inherent differences among the results of the various investigations and the want for a calibration experiment specifically conceived to advance standard Reynolds-number range for each flow regime. In view of the observed disparaties and based on a review of published data (refs. 19,21,34,47,48,50,57), including that of the present investigation, the following Reynolds-number ranges are proposed for these four flow regimes: (1) subcritical flow at $Re < 2.5x10^5$; (2)

critical flow at $2.5x10^5 < Re < 5x10^5$; (3) supercritical flow at $5x10^5 < Re < 3.5x10^6$; and, (4) transcritical flow at $Re > 3.5x10^6$. These Reynolds-number ranges are advanced, according to the established custom, based on the variations of the separation angle and the drag coefficient with increasing Reynolds number in smooth incident flow.

The results obtained here in turbulent incident flow at subcritical Reynolds numbers were compared with those reported by Achenbach (refs. 19,47), Guven et al. (ref. 34), James et al. (ref. 48) and Jones et al. (ref. 50) for a smooth cylinder in a smooth incident flow in critical, supercritical and transcritical flow regimes. A summary of the experimental conditions under which the data taken from these five studies was collected is provided in Table 4 below. In addition to the Reynolds numbers, the freestream turbulence intensity (Tu) of the nominally smooth incident flow, the freestream Mach number (M), the blockage coefficient (D/h), and the relative surface roughness (k/D) are listed in this table. Lack of information is denoted by NR which means not reported. The experimental conditions of the present test (background turbulence intensity at the test position, blockage coefficient, relative surface roughness) are given in this table for convenience's sake. It is apparent that the incident flow in these five studies can be classified as smooth since the freestream turbulence intensity was always below 1%. The Mach number is included in Table 4 in order to point out that the compressibility effect upon the separation angle and drag coefficient can be disregarded at the selected high transcritical Reynolds numbers. This effect is important at Mach numbers greater than about 0.25 or 0.30 (ref. 50). The blockage coefficient is listed for comparison's sake despite that no correction was applied. Note that the blockage was the smallest in the present test. The values of the relative surface roughness indicate the high degree of smoothness of the cylinders used

TABLE 4. EXPERIMENTAL CONDITIONS

Source	Ref.	Re ($x10^{-5}$)	Tu (%)	M	D/h (%)	k/D ($x10^5$)
Achenbach	19,Figs. 4-6, 9-10	2.6-36	0.70	< 0.1	16.7	1 1/3
	47,Figs. 6-9	1.0-40	0.45	< 0.1	16.4	NR
Guven et al.	34,Tb. 4.2	2.24-5.63	0.20	< 0.1	17.8	NR
James et al.	48,Figs. 3-6	9.2-109	NR	0.27-0.28	9.2-13.1	0.185-0.309
Jones et al.	50,Figs. 5,10 Tb. 1	4.0-90	0.17	< 0.30	19.3	0.185
Present Test		0.52-2.09	2.05-4.10	< 0.1	8.7	1.6

Tb. means Table; NR means not reported.

in these studies. In the two cases in which the relative surface roughness is not reported, the appearance of the cylinder surface is described as 'highly polished'.

Variations of the separation angle θ_s and drag coefficient C_D measured here, along with those given and/or deduced from the data reported in the foregoing five studies, are portrayed as function of increasing Reynolds number in Figs. 6.36 and 6.37, respectively. In addition, the variations with increasing Reynolds number of the angular extent of the adverse pressure gradient region θ_{sm}, the base pressure coefficient C_{pb} and the pressure rise coefficient C_{pbm} obtained in the present investigation and in the aforementioned studies are shown in Figs. 6.38, 6.30 and 6.40, respectively. The four flow regimes are delineated in all these figures according to the Reynolds-number ranges introduced herein.

The similarity of the present results with those in smooth incident flow at higher Reynolds numbers is clearly discerned. This remarkable similarity attests to the effect of the interaction of amplified turbulence with the boundary layer as proposed by the vorticity-amplification theory. The prevalent laminar boundary layer in the subcritical regime is energized by the penetrating turbulence and, consequently, its characteristics and nature are drastically altered. It should be noted that the behavior of the modified boundary layer cannot exactly be assessed at this time since measurements of the velocity variation within it, the skin friction and the wake have not yet been completed. One can, however, hypothesize what are the main changes in the nature of the boundary layer based on the observed similarity of the various characteristics. In view of the dependence of these changes upon Reynolds number-background turbulence combination and of the division of smooth incident flow in distinct flow regimes, each case is examined according to the observed separation angle and associated mean drag coefficient. Inspection of the gradual increase in the separation angle and the attendant reduction of the mean turbulent drag coefficient with higher Reynolds number for each grid position (or background turbulence) shown in Figs. 6.36 and 6.37 suggests the realization of four different types of boundary layer.

At the present lowest subcritical Reynolds number of 5.2×10^4 with the grid at $\tilde{x}_g = 14$ and 20, separation angles (95 & 85°) and drag coefficients (1.13 & 1.14) slightly larger than in smooth incident flow were found. These results indicate that the interaction of turbulence with the

boundary layer supplied additional momentum that enabled the flow to follow the cylinder contour for a little longer distance but, in all likelihood, not sufficient to alter the initial laminar nature of the boundary layer. The slight increase in the drag is, as a matter of fact, the outcome of this lengthening. One can view this slightly longer laminar boundary layer as being buffeted by the turbulence, viz., a buffeted laminar boundary layer. As far as the similarity of this buffeted laminar boundary layer to that in smooth incident flow at higher Reynolds numbers is concerned, it corresponds to that found in the lower Reynolds-number range ($Re < 3x10^5$) of the critical regime.

Separation angles greater than 90° (105 & 110°) and drag coefficients slightly smaller than in smooth incident flow (1.0 & 1.03) were obtained at $Re = 5.2x10^4$ and $9.4x10^4$ with the grid at $\tilde{x}_g = 8$ and 20, respectively. In addition, a short laminar separation bubble apparently occurred around the cylinder crest (around 90 to 100°) ahead of separation in these two cases, as earlier mentioned. One can, therefore, infer that the penetration of turbulence into the boundary layer provided sufficient momentum to arrest the growth of the laminar separation bubble and to induce, downstream of it, transition and reattachment to a short turbulent boundary layer followed by turbulent separation. This boundary layer can also be considered as buffeted by the turbulence in view of its structure. It is further apparent that this boundary layer is essentially similar to that prevailing in smooth incident flow in the critical regime.

At $Re = 9.4x10^4$ with the grid at $\tilde{x}_g = 8$ and 14 and at $Re = 1.25x10^5$ with the grid at $\tilde{x}_g = 20$, separation angles on the back of the cylinder (125,120 & 122°) along with drag coefficients smaller than in smooth incident flow (0.68,0.93 & 0.85) were monitored. Simultaneously, no indication of the occurrence of a laminar separation bubble was detected. One can, therefore, deduce that the energizing of the boundary layer by the penetrating turbulence caused in these cases eradication of the laminar separation bubble and, hence, direct transition to a turbulent boundary at angles larger than 90° followed by turbulent separation. Thus, this boundary layer exhibits features similar to those found in smooth incident flow in the supercritical regime.

Finally, at $Re = 1.25x10^5$ with the grid at $\tilde{x}_g = 8$ and 14 and at $Re = 1.67x10^5$ and $2.09x10^5$ for all three grid positions ($\tilde{x}_g = 8,14,20$), nearly constant separation angle of 130° (128 to 130°) and drag coefficients much smaller than in smooth incident flow and of almost constant magnitude (0.65 to 0.43) were obtained. This behavior indicates

that the diffusion of the penetrating turbulence into the boundary layer furnished ample momentum to induce direct transition from a laminar to a turbulent boundary layer on the front of the cylinder (at angles smaller than 90°) followed by turbulent separation on the back side. The angular position of the transition depends on the intensity of the penetrating turbulence and, particularly, on the level of turbulent energy concentrated at scales commensurate with the boundary-layer thickness. As a result, the transition can occur at any angle in the favorable pressure gradient region and even it can move to the stagnation point leading to the growth of a fully developed turbulent boundary layer. In view of these characteristics, one can conclude that the boundary layer in these cases is basically of the same nature as those observed in smooth incident flow within the upper Reynolds-number range of supercritical regime ($Re > 10^6$) and in the transcritical regime. Recall that in these two flow regimes transition angles ranging from about 80 to nearly 20° are found in smooth incident flow (ref. 47).

Further substantiation of the striking correspondence of the boundary-layer characteristics at subcritical Reynolds numbers in turbulent incident flow to those found at higher Reynolds numbers in smooth incident flow is provided by the variations of the angular extent of the adverse pressure gradient region, the base pressure and the pressure rise coefficients portrayed in Figs. 6.38, 6.39 and 6.40. *The aspect of prime interest of these results is that a boundary-layer flow similar to that found in critical, supercritical and/or transcritical flow regimes is induced by turbulence at subcritical Reynolds numbers. In other words, the effect of turbulence is equivalent to an effective increase in the Reynolds number. The results further indicate that one can manage the position of the separation point and the magnitude of the mean turbulent drag coefficient in the subcritical regime by prescribing the Reynolds number-background turbulence combination.*

8. CONCLUDING REMARKS

The results presented in this work indicate quite clearly that the interaction of incident turbulence with the initial laminar boundary layer on a smooth circular cylinder in crossflow at subcritical Reynolds numbers from 5.2×10^4 to 2.09×10^5 modifies the characteristics of the mean surface pressure distribution, delays the separation and reduces the drag. These changes exhibited a distinct dependence upon the Reynolds number-background turbulence combination, where the latter is the grid-produced turbulence monitored behind the grid at the test position of the cylinder in its absence. Generally, the modifications of the characteristics of the mean surface pressure distribution consisted of: (1) a more favorable pressure gradient along the front of the cylinder; (2) a more negative minimum pressure and a rearward shift in its angular position; (3) a longer adverse pressure gradient region and a greater pressure rise across it; (4) a shorter base region; and, finally, (5) a less negative base pressure than in smooth (laminar) incident flow at the same Reynolds number. The aft shift in the separation point ranged from 5 to a maximum of 50° beyond the constant laminar separation angle of about 80°, since separation angles varying from 85 to 130° were obtained based on the mean surface pressure distribution and further corroborated by their visualization. At the same time, the mean turbulent drag coefficient reduced from around 1.0 to about 0.43 with increasing Reynolds number and, hence, it amounted, for the most part, from 97 to 46% of its nearly constant laminar counterpart. Only in two cases out of the different fifteen Reynolds number-background turbulence situations surveyed, the mean drag coefficient was slightly greater (by about 6 to 7%) than in smooth incident flow due to the nature of the boundary layer.

These significant changes in the properties of the boundary layer result, according to the vorticity-amplification theory, from the energizing of the initial laminar boundary layer by penetrating turbulence concentrated at scales commensurate with its thickness. Turbulent energy accumulates within such eddies owing to the preferred amplification of freestream turbulence induced by the stretching of cross-vortex tubes in the diverging flow around the cylinder. These energy-containing eddies form a coherent substructure near the cylinder stagnation zone (refs. 6,58), which ensures a continual supply of turbulent momentum and energy to the boundary layer.

This turbulence-boundary layer interaction mechanism is supported by the correlations among the various characteristics of the mean surface pressure distributions and the position of the separation point with a turbulence parameter

Tu_b^2Re (or Tu_c^2Re) and a turbulent separation parameter $(\Lambda_b/\pi D)Tu_bRe^{\frac{1}{2}}$. These correlations attest to the transfer of turbulent momentum to the boundary layer and to the dependence of the interaction on the scale of the background turbulence. In addition, these correlations supply a method that permits immediate estimation of the turbulent separation angle and associated characteristics of the adverse pressure gradient region for any given Reynolds number-background turbulence combination in terms of solely two readily measurable properties of the background turbulence, the Reynolds number and the cylinder diameter.

The separation angles, the mean drag coefficients and the characteristics of the mean surface pressure distribution, measured at the present subcritical Reynolds numbers ($5.2x10^4$-$2.09x10^5$) in turbulent incident flow are generally of the same magnitude as those reported for a smooth cylinder in smooth incident flow at higher critical ($2.5x10^5$-$5x10^5$), supercritical ($5x10^5$-$3.5x10^6$) and transcritical ($> 3.5x10^6$) Reynolds numbers. This similarity substantiates the proposition that the penetrating turbulence modifies the nature and properties of the initial laminar boundary layer. However, the degree of modification depends: (1) on the extent to which the penetrating amplified turbulence supplies sufficient momentum to enable the flow to follow the cylinder contour for a longer distance; and, (2) on the increase in the base pressure (less negative) consequent upon the weakening of the forming vortexes in the near wake which, in turn, is induced by the entrainment across the wake of fluid from the outer turbulent flow.

Further examination of the correspondence of the separation angles and the drag coefficients suggests that turbulence promotes, depending on the particular Reynolds number-background turbulence (or grid position) combination, the development of: (1) a buffeted laminar boundary layer at lower subcritical Reynolds number, which is similar to that found in the critical regime; (2) direct transition on the back of the cylinder from a laminar to a turbulent boundary layer followed by turbulent separation at intermediate subcritical Reynolds numbers, which is similar to that found in the supercritical regime; and, for the most part, (3) direct transition on the front of the cylinder and, in all probability, even at the stagnation point to a turbulent boundary layer followed by turbulent separation on the back side at higher subcritical Reynolds numbers, which is generally similar to that found in the supercritical and, particularly, in the transcritical regime. A buffeted laminar boundary layer is either a slightly longer laminar boundary layer that separates laminarly around the cylinder crest and/or a laminar boundary layer with a short laminar separation bubble around the cylinder crest followed on the

back of the cylinder by transition and reattachment to a short turbulent boundary layer and turbulent separation.

These hypotheses are submitted here based on the observed similarity of the separation angles and drag coefficients, along with that of the key characteristics of the surface pressure distribution, since the survey of the modified boundary layer has not yet been consummated. Notwithstanding the relatively conjectural aspect of these hypotheses, the results clearly point out that the interaction of turbulence with the boundary layer is equivalent to an effective increase in the Reynolds number. Another aspect of major interest revealed by the results is that one can manage the position of the separation point and the magnitude of the mean drag coefficient at subcritical Reynolds numbers by controlling the Reynolds number-background turbulence combination.

In conclusion, the change in the nature of the boundary layer in the subcritical regime as a result of the penetration of turbulence into it is in basic agreement with the model put forward by the vorticity-amplification theory.

REFERENCES

1. Fage, A. & Warsap, J. H.: The effects of turbulence and surface roughness on the drag of a circular cylinder. ARC R&M 1283, 1929, pp. 1-8.

2. Fage, A. & Falkner, V. M.: Further experiments on the flow around a circular cylinder. ARC R&M 1369, 1931, pp. 186-198.

3. Giedt, W. H.: Effect of turbulence level of incident air stream on local heat transfer and skin friction on a cylinder. J. Aero. Sciences, vol. 18, no. 11, 1951, pp. 725-730.

4. Sutera, S. P., Maeder, P. F. & Kestin, J.: On the sensitivity of heat transfer in the stagnation-point boundary layer to freestream vorticity. J. Fluid Mech., vol. 16, part 4, 1963, pp. 497-520.

5. Sadeh, W. Z., Sutera, S. P. & Maeder, P. F.: Analysis of vorticity amplification in the flow approaching a two-dimensional stagnation point. Z. angew. Math. Phys. (ZAMP-J. Appl. Math. & Phys.), vol. 21, fasc. 5, 1970, pp. 699-716.

6. Sadeh, W. Z. & Brauer, H. J.: A visual investigation of turbulence in stagnation flow about a circular cylinder. J. Fluid Mech., vol. 99, part 1, 1980, pp. 53-64.

7. Schlichting, H.: Boundary-Layer Theory. 7th ed., McGraw-Hill Book Co., New York, New York, 1979.

8. Corrsin, S.: Turbulence: Experimental Methods. Encyclopedia of Physics, eds. Flügge, S. & Truesdell, C., Fluid Dynamics II, vol. VIII/2, Springer-Verlag, Berlin, 1963.

9. Comte-Bellot, G. & Corrsin, S.: The use of a contraction to improve the isotropy of grid-generated turbulence. J. Fluid Mech., vol. 25, part 4, 1966, pp. 657-682.

10. Gad-el-Hak, M. & Corrsin, S.: Measurements of nearly isotropic turbulence behind a uniform jet grid. J. Fluid Mech., vol. 62, part 1, 1974, pp. 115-143.

11. Sadeh, W. Z. & Sullivan, P. P.: Turbulence behind a grid of parallel rods (to be published).

12. Roshko, A.: On the development of turbulent wakes from vortex streets. NACA TR 1191, 1954.

13. Taylor, G. I.: The spectrum of turbulence. Proc. Roy. Soc., A, Vol. CLXIV, 1938, pp. 524-533.

14. Sadeh, W. Z., Brauer, H. J. & Durgin, J. R.: Dry-surface coating method for visualization of separation on a bluff body. AIAA J., vol. 19, no. 7, 1981, pp. 954-956.

15. Hurd, C. W., Chesky, K. P. & Shapiro, A. H.: Influence of viscous effects on impact tubes. Trans. ASME, J. Appl. Mech., vol. 20, no. 2, 1953, pp. 253-256.

16. Dean, R. C., Jr., ed.: Aerodynamic Measurements. Gas Turbine Lab., Massachusetts Inst. of Technology, Cambridge, Massachusetts, 1955, pp. 61-65.

17. Ower, E. & Pankhurst, R. C.: The Measurement of Airflow. 4th ed., Pergamon Press, London, England, 1966, pp. 45-46.

18. Goldstein, S., ed.: Modern Developments in Fluid Dynamics. Vol. II, Dover Publications, Inc., New York, New York, 1965, p. 428.

19. Achenbach, E.: Distribution of local pressure and skin friction around a circular cylinder in cross-flow up to Re = $5x10^6$. J. Fluid Mech., vol. 34, part 4, 1968, pp. 625-639.

20. Allen, H. J. & Vincenti, W. G.: Wall interference in a two-dimensional-flow wind tunnel, with consideration of the effect of compressibility. NACA Report No. 782, 1944.

21. Roshko, A.: Experiments on the flow past a circular cylinder at very high Reynolds number. J. Fluid Mech., vol. 10, part 3, 1961, pp. 345-356.

22. Dalton, C.: Allen and Vincenti blockage corrections in a wind tunnel. AIAA Journal, vol. 9, no. 9, 1971, pp. 1864-1865.

23. Farell, C., Carrasquel, S., Güven, O. & Patel, V. C.: Effect of wind-tunnel walls on the flow past circular cylinders and cooling tower models. Trans. ASME, J. Fluid Engin., vol. 99, series 1, no. 3, 1977, pp. 470-479.

24. Maskell, E. C.: A theory of blockage effects on bluff bodies and stalled wings in a close wind tunnel. ARC R&M 3400, 1963.

25. McKeon, R. J. & Melbourne, W. H.: Wind tunnel blockage effects and drag on bluff bodies in a rough wall boundary layer. Proceedings, Third International Conference on Wind Effects on Buildings and Structures, Tokyo, Japan, 6-9 September 1971, ed., Japanese Organizing Committee, Saikon Co., Ltd., Tokyo, Japan, 1971, pp. 263-272.

26. Modi, V. J. & El-Sherbiny, S.: Wall confinement effects on bluff bodies in turbulent flows. Proceedings, Fourth International Conference on Wind Effects on Buildings and Structures, London, England, 8-12 September 1975, ed., Eaton, K. J., Cambridge University Press, Cambridge, England, 1977, pp. 121-132.

27. Achenbach, E.: Influence of surface roughness on the cross-flow around a circular cylinder. J. Fluid Mech., vol. 46, part 2, 1971, pp. 321-335.

28. Bearman, P. W.: On vortex shedding from a circular cylinder in the critical Reynolds number regime. J. Fluid Mech., vol. 37, part 3, 1969, pp. 577-585.

29. Modi, V. J. & El-Sherbiny, S.: Effect of wall confinement on aerodynamics of stationary circular cylinders. ibid Ref. 25, pp. 365-375.

30. Eskinazi, S.: Principles of Fluid Mechanics. Allyn and Bacon, Inc., Boston, Massachusetts, 1968, p. 304.

31. Flachsbart, O.: Winddruck auf Gasbehälter, TR Aerodyn. Versuchsanstalt, Göttingen, Germany, IVth series, 1932, pp. 134-138.

32. Chang, P. K.: Separation of Flow. Pergamon Press, New York, New York, 1970, p. 14.

33. Batham, J. P.: Pressure distributions on circular cylinders at critical Reynolds numbers. J. Fluid Mech., vol. 57, part 2, 1973, pp. 209-228.

34. Guven, O., Patel, V. C. and Farell, C.: Surface roughness effects on the mean flow past circular cylinders. Iowa Inst. of Hydraulic Research, Rep. No. 175, University of Iowa, Iowa City, Iowa, 1975.

35. Morsbach, M.: Über die Bedingungen für eine Wirbelstrassenbildung hinter Kreiszylinder. Dissertation, T. H. Aachen, Aachen, Germany, 1967.

36. Okamuto, T. & Takeuchi, M.: Effect of side walls of wind-tunnel on flow around two-dimensional circular cylinder and its wake. Bulletin, Japanese Soc. of Mech. Eng., vol. 18, no. 123, 1975, pp. 1011-1017.

37. Wieselsberger, C.: Neuere Feststellungen über die Gesetze des Flüssigkeitsund Luftwiderstandes. Physikalishe Zeitschrift, vol. 22, no. 11, 1921, pp. 321-328.

38. Schmidt, E. & Wenner, K.: Heat transfer over the circumference of a heated cylinder in transverse flow. English trans., NACA TM 1050, 1943.

39. Bursnall, W. J. & Loftin, Jr., L. K.: Experimental investigation of the pressure distribution about a yawed circular cylinder in the critical Reynolds number range. NACA TN 2463, 1951.

40. Delany, N. K. & Sorensen, N. E.: Low-speed drag of cylinders of various shapes. NACA TN 3038, 1953.

41. Polhamus, E. C.: Effect of flow incidence and Reynolds number on low-speed aerodynamic characteristics of several noncircular cylinders with applications to directional stability and spinning. NACA TR R-29, 1959.

42. Hinze, J. O.: Turbulence. 2nd ed., McGraw-Hill Book Co., New York, New York, 1975, p. 65.

43. Dryden, H. L., Schubauer, G. B., Mock, Jr., W. C. & Skramstad, H. K.: Measurement of intensity and scale of wind-tunnel turbulence and their relation to the critical Reynolds number of spheres. NACA Rep. 581, 1937.

44. Batchelor, G. K. & Townsend, A. A.: Decay of turbulence in the initial period. Proc., Royal Soc., London, A, vol. 193, 1948, pp. 539-558.

45. Uberoi, M. S.: Energy transfer in isotropic turbulence. Phy. of Fluids, vol. 6, no. 8, 1963, pp. 1048-1056.

46. Simpson, R. L.: Review - A review of some phenomena in turbulent flow separation. J. Fluids Engin., Trans. ASME, vol. 103, no. 4, 1981, pp. 520-533.

47. Achenbach, E.: Total and local heat transfer from a smooth circular cylinder in cross-flow at high Reynolds number. Int. J. Heat Mass Transfer, vol. 18, 1975, pp. 1387-1396.

48. James, W. D., Paris, S. W. & Malcolm, G. N.: Study of viscous crossflow effects on circular cylinders at high Reynolds numbers. AIAA J., vol. 18, no. 9, 1980, pp. 1066-1072.

49. Kamiya, N., Suzuki, S. & Nishi, T.: On the aerodynamic force acting on a circular cylinder in the critical range of the Reynolds number. AIAA 12th Fluids and Plasma Dynamics Conference, Williamsburg, Virginia, 23-25 July 1979, Paper 79-1475.

50. Jones, G. W., Cincotta, J. J. & Walker, R.W.: Aerodynamic forces on a stationary and oscillating circular cylinder at high Reynolds numbers. NASA TR R-300, 1969.

51. Morkovin, M. V.: Flow around circular cylinder-A kaleidoscope of challenging fluid phenomena. Symposium on Fully Separated Flows, Philadelphia, Pennsylvania, 18-20 May 1964, ed., Hansen, A. G. ASME, pp. 102-118.

52. Stratford, B. S.: The prediction of separation of the turbulence boundary layer. J. Fluid Mech., vol. 5, part 1, 1956, pp. 1-16.

53. Townsend, A. A.: The behaviour of a turbulent boundary layer near separation. J. Fluid Mech., vol. 12, part 3, 1962, pp. 536-554.

54. Surry, D.: Some effects of intense turbulence on aerodynamics of a circular cylinder at subcritical Reynolds number. J. Fluid Mech., vol. 52, part 3, 1972, pp. 543-563.

55. Gerrard, J. H.: The mechanics of the formation region of vortices behind bluff bodies. J. Fluid Mech., vol. 25, part 2, 1966, pp. 401-413.

56. Eppler, R.: Beiträge zu Theorie und Anwendung der unstetigen Strömungen. J. Rational Tech. Anal., vol. 3, 1954, pp. 591-644.

57. Farell, C.: Flow around fixed circular cylinders: Fluctuating loads. J. Eng. Mech. Div., Proc. ASCE, vol. 197, No. EM3, 1981, pp. 565-688.

58. Sadeh, W.Z. & Brauer, H.J.: Coherent substructure of turbulence near the stagnation zone of a bluff body. J. Wind Eng. Indus. Aero., 8, 1981, pp. 59-72.

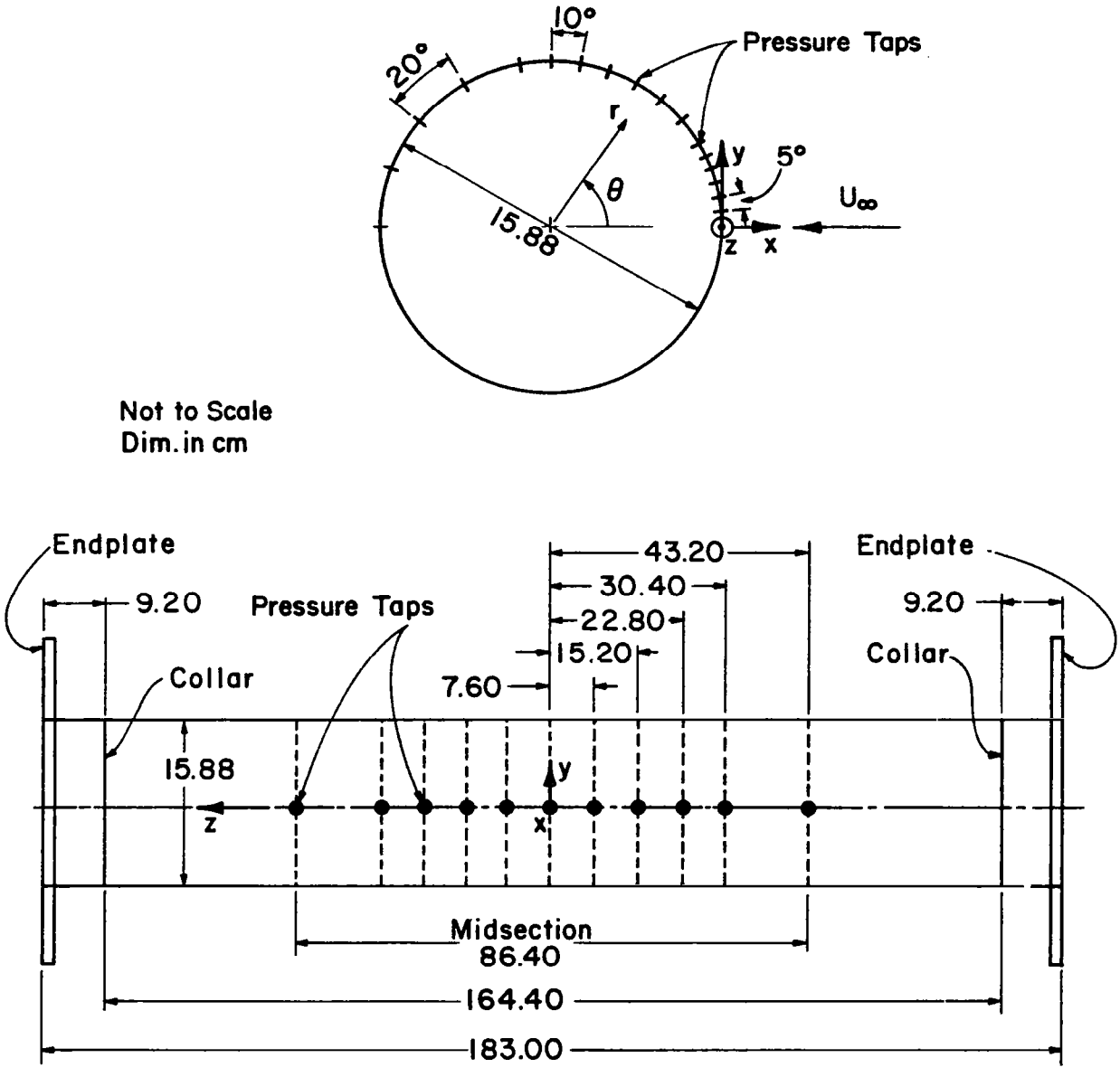

Fig. 2.1 Sketch of circular cylinder showing location of pressure taps and system of coordinates.

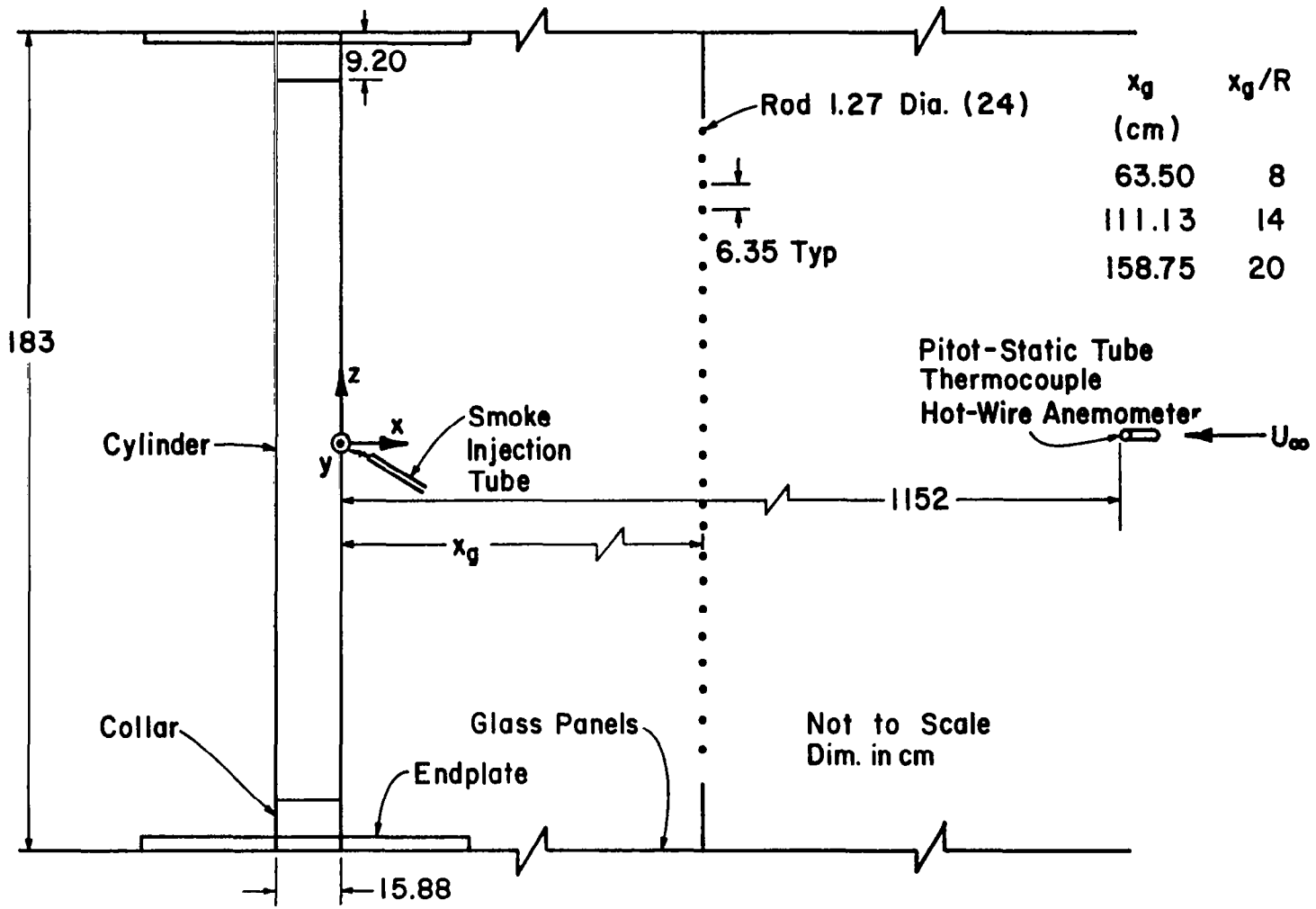

x_g (cm)	x_g/R
63.50	8
111.13	14
158.75	20

Fig. 2.2 Sketch of experimental arrangement.

Fig. 2.3 View of test section showing the circular cylinder and the turbulence-generating grid.

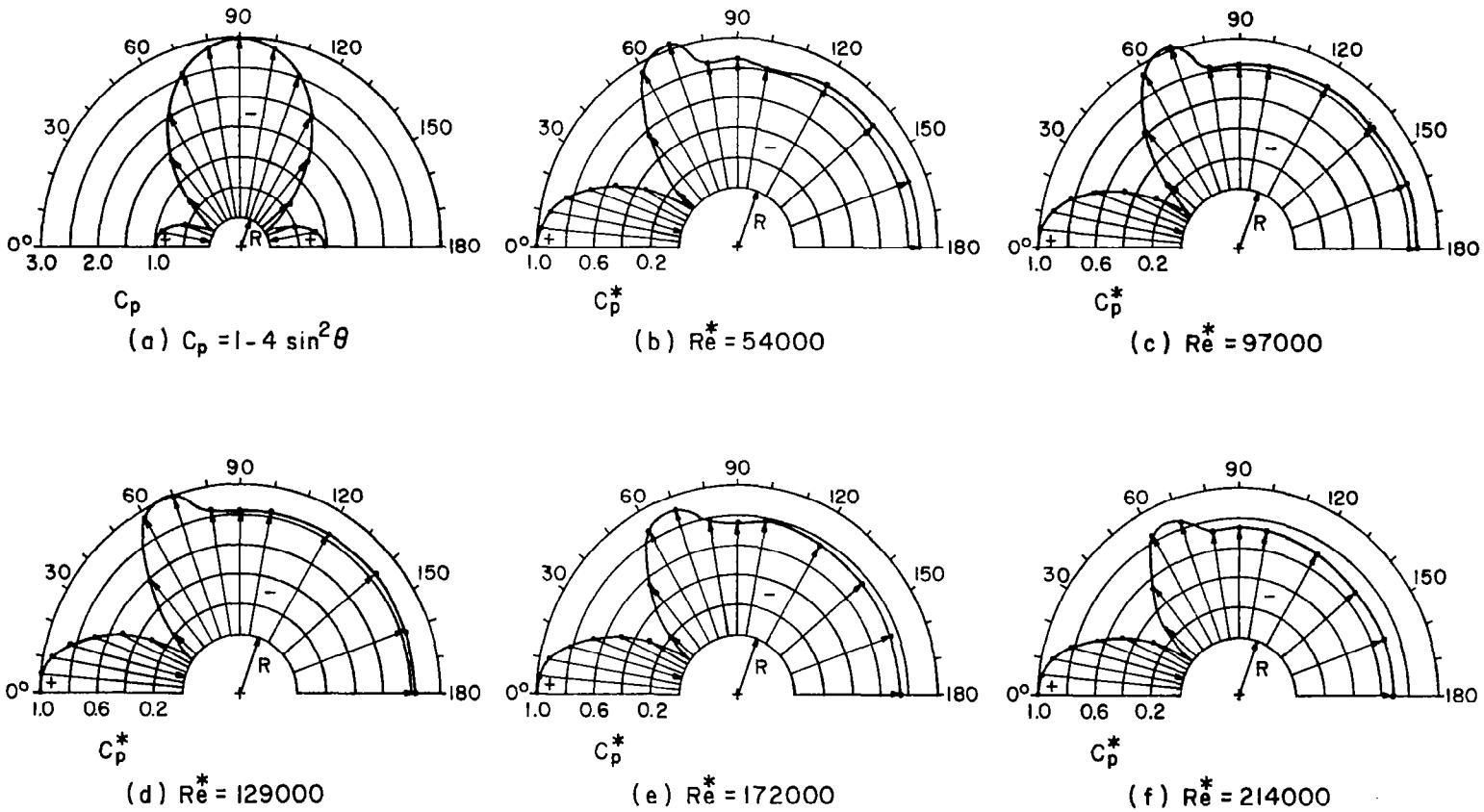

Fig. 5.1 Pressure coefficient (corrected) distribution at subcritical Reynolds numbers in smooth incident flow and in potential flow (a); polar form.

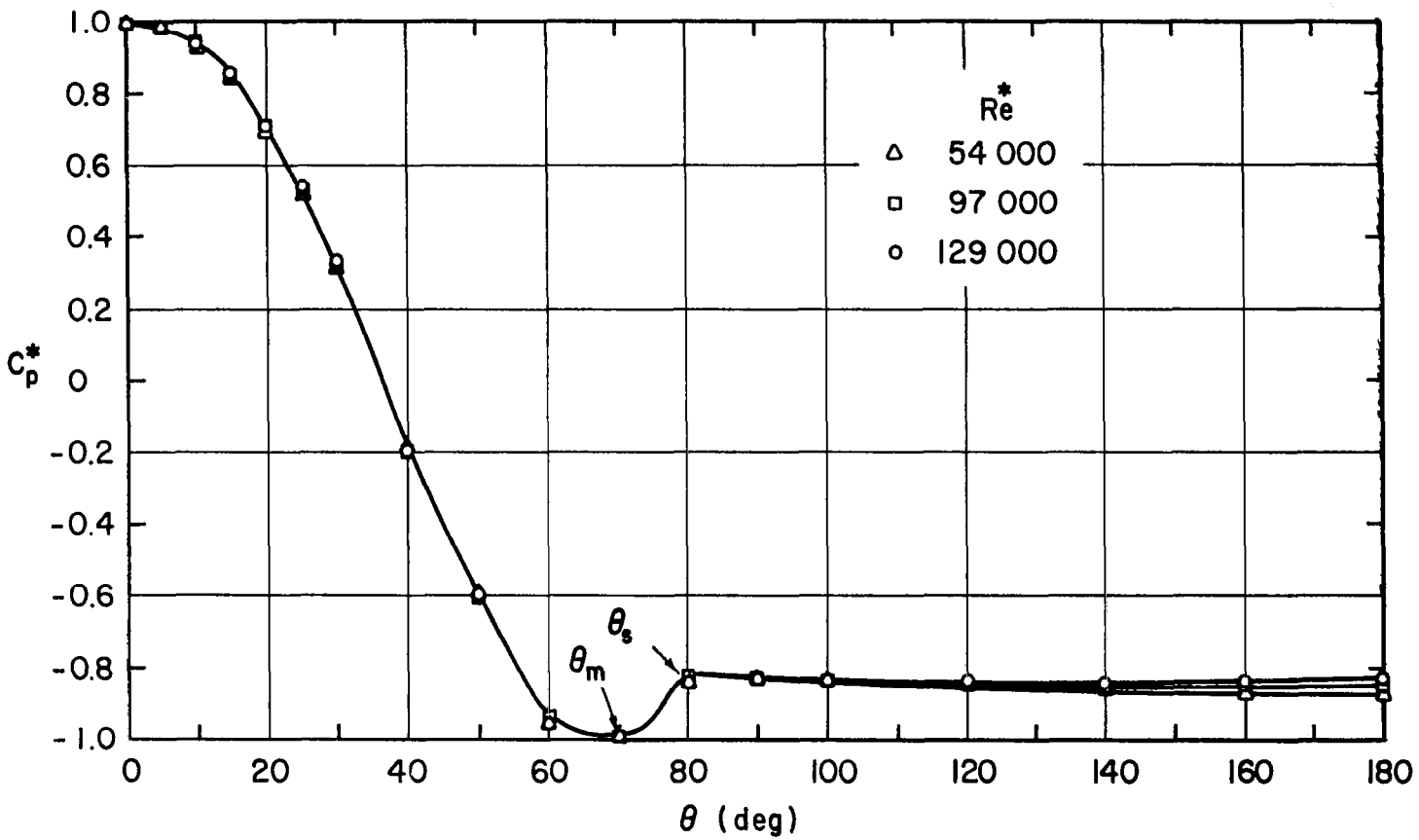

Fig. 5.2 Pressure coefficient (corrected) distribution in smooth incident flow at $Re^* = 5.4 \times 10^4$, 9.7×10^4 and 1.29×10^5 .

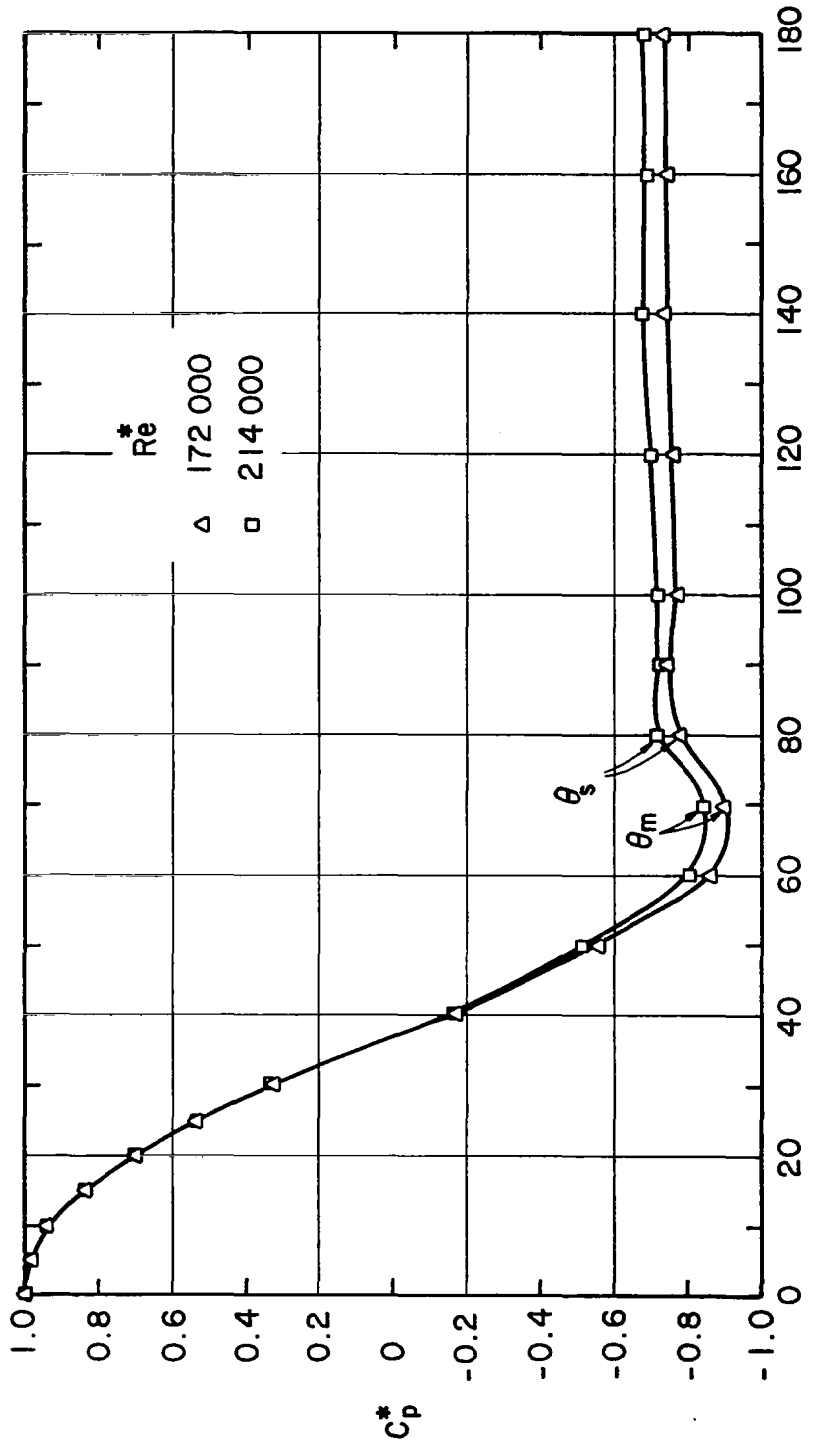

Fig. 5.3 Pressure coefficient (corrected) distribution in smooth incident flow at $Re^* = 1.72 \times 10^5$ and 2.14×10^5.

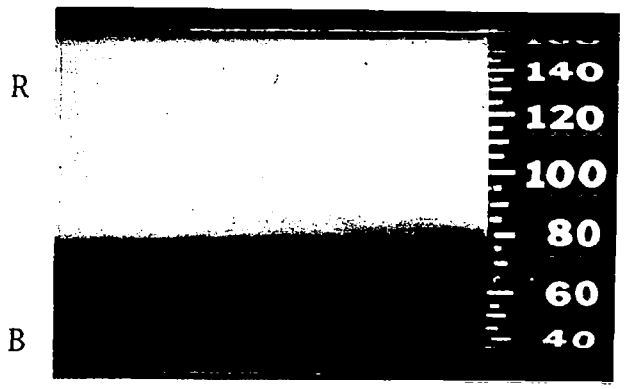

Fig. 5.4 View of separation angle in smooth incident flow at subcritical Reynolds numbers; B: Blue, attached flow; R: Red, separated flow.

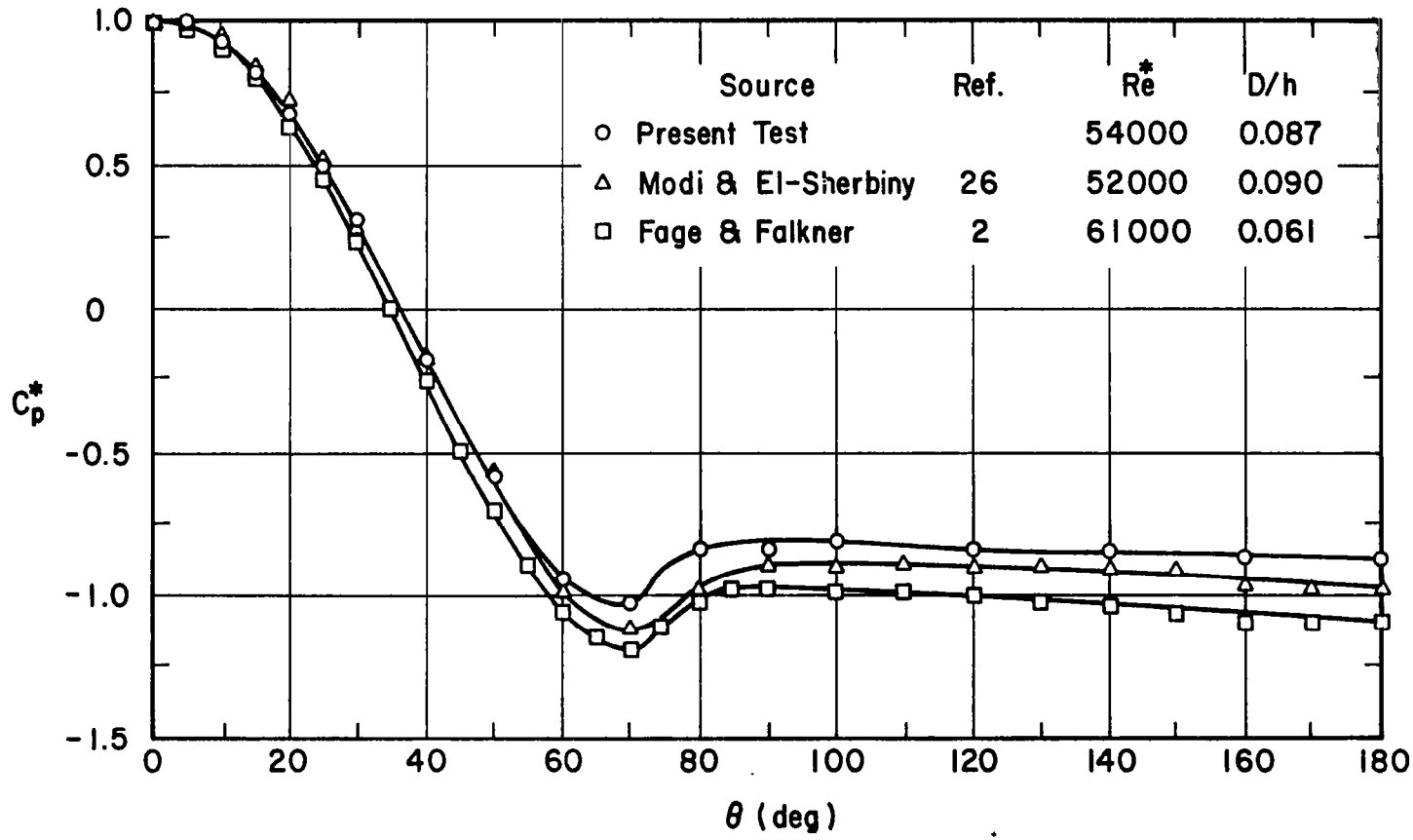

Fig. 5.5 Pressure coefficient (corrected) distribution comparison.

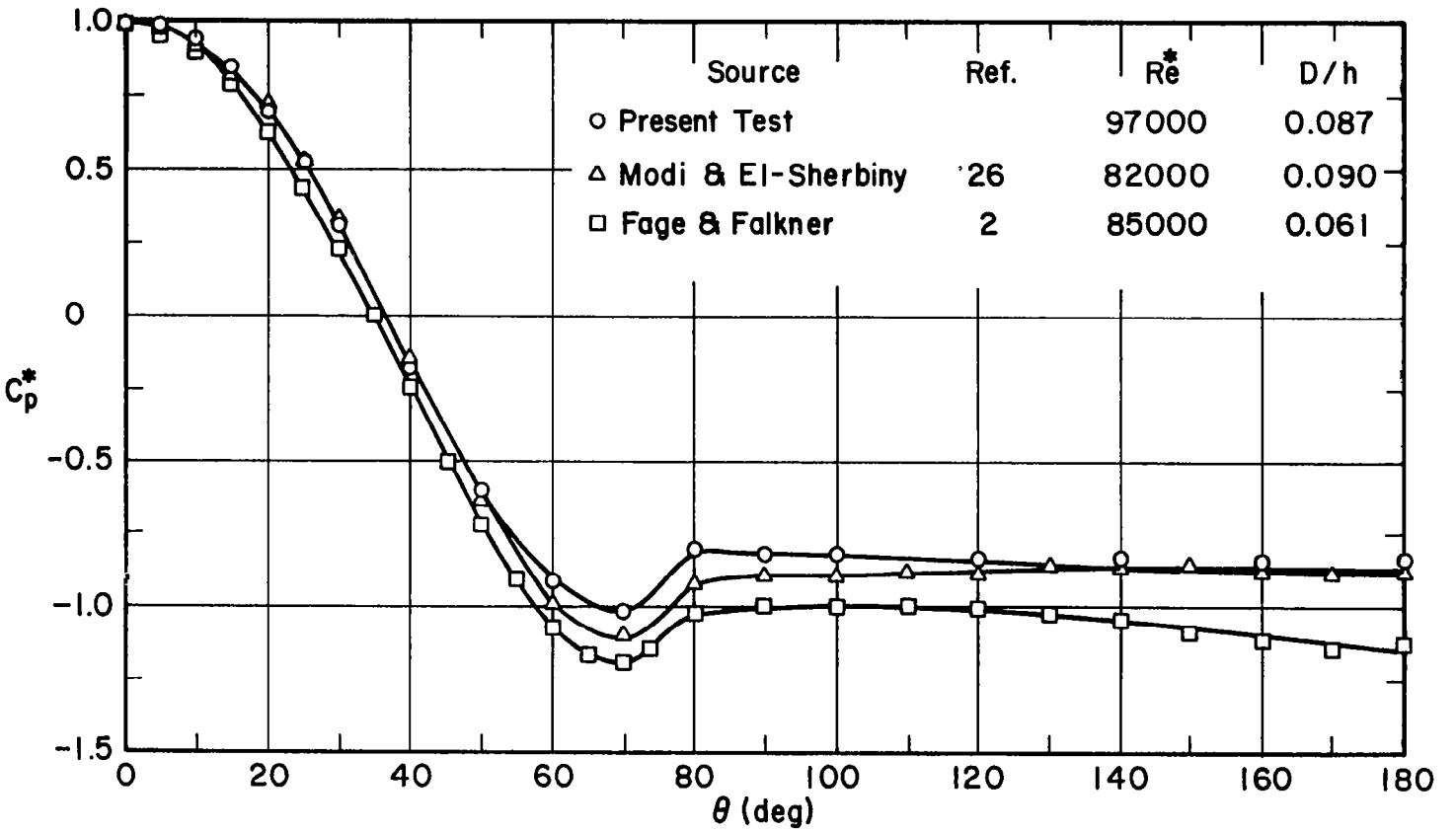

Fig. 5.6(a) Pressure coefficient (corrected) distribution comparison.

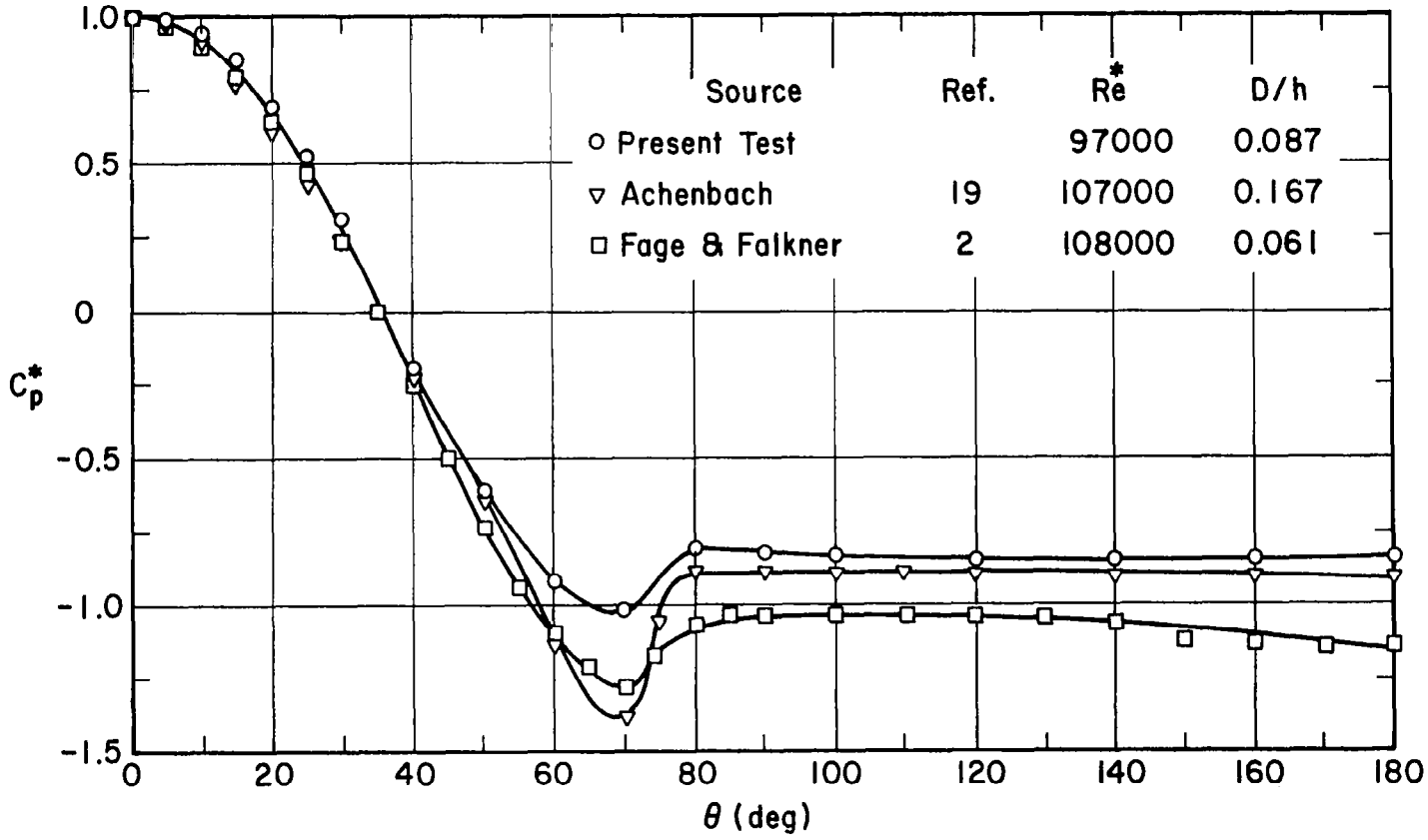

Fig. 5.6(b) Pressure coefficient (corrected) distribution comparison.

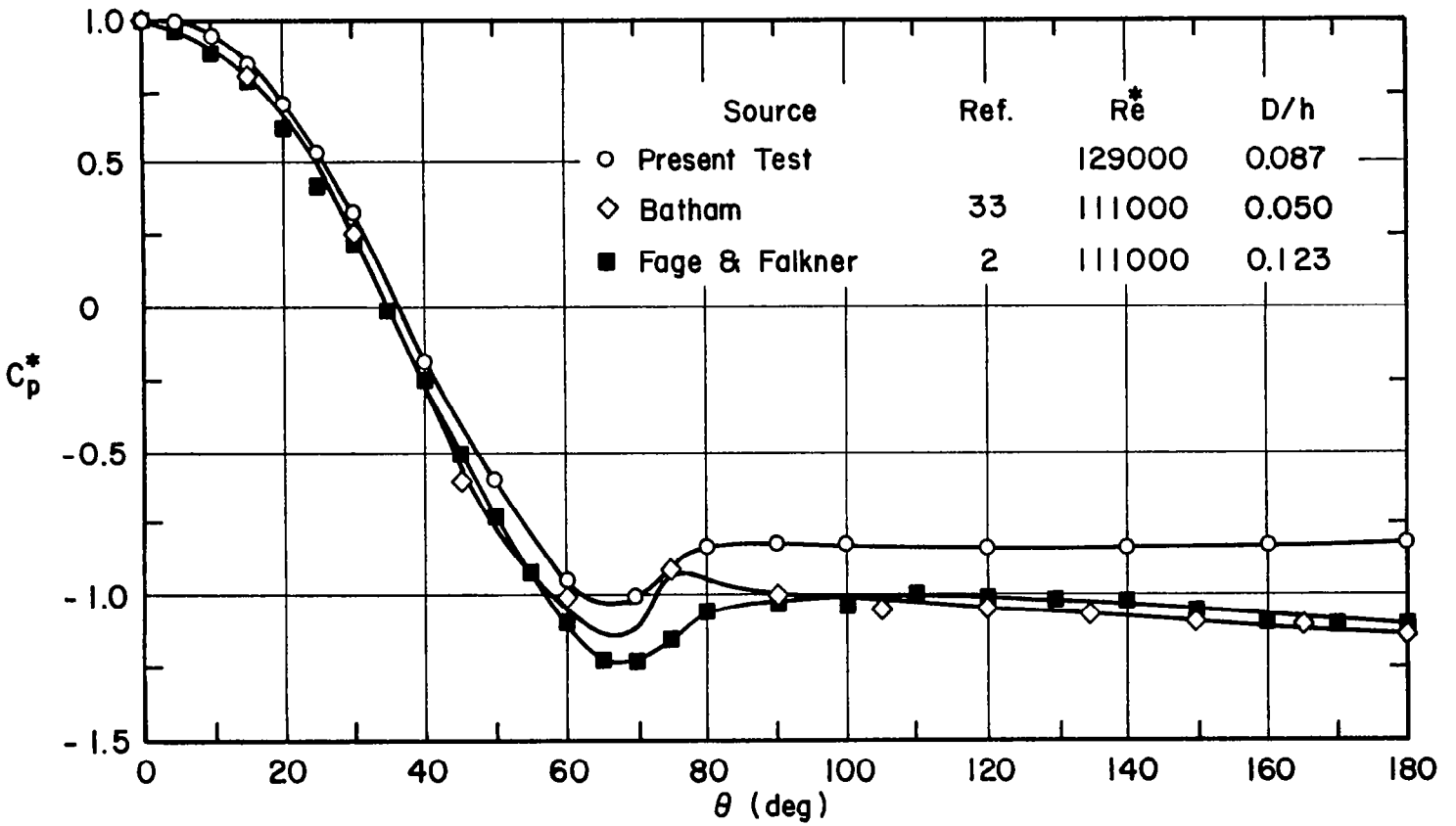

Fig. 5.7 Pressure coefficient (corrected) distribution comparison.

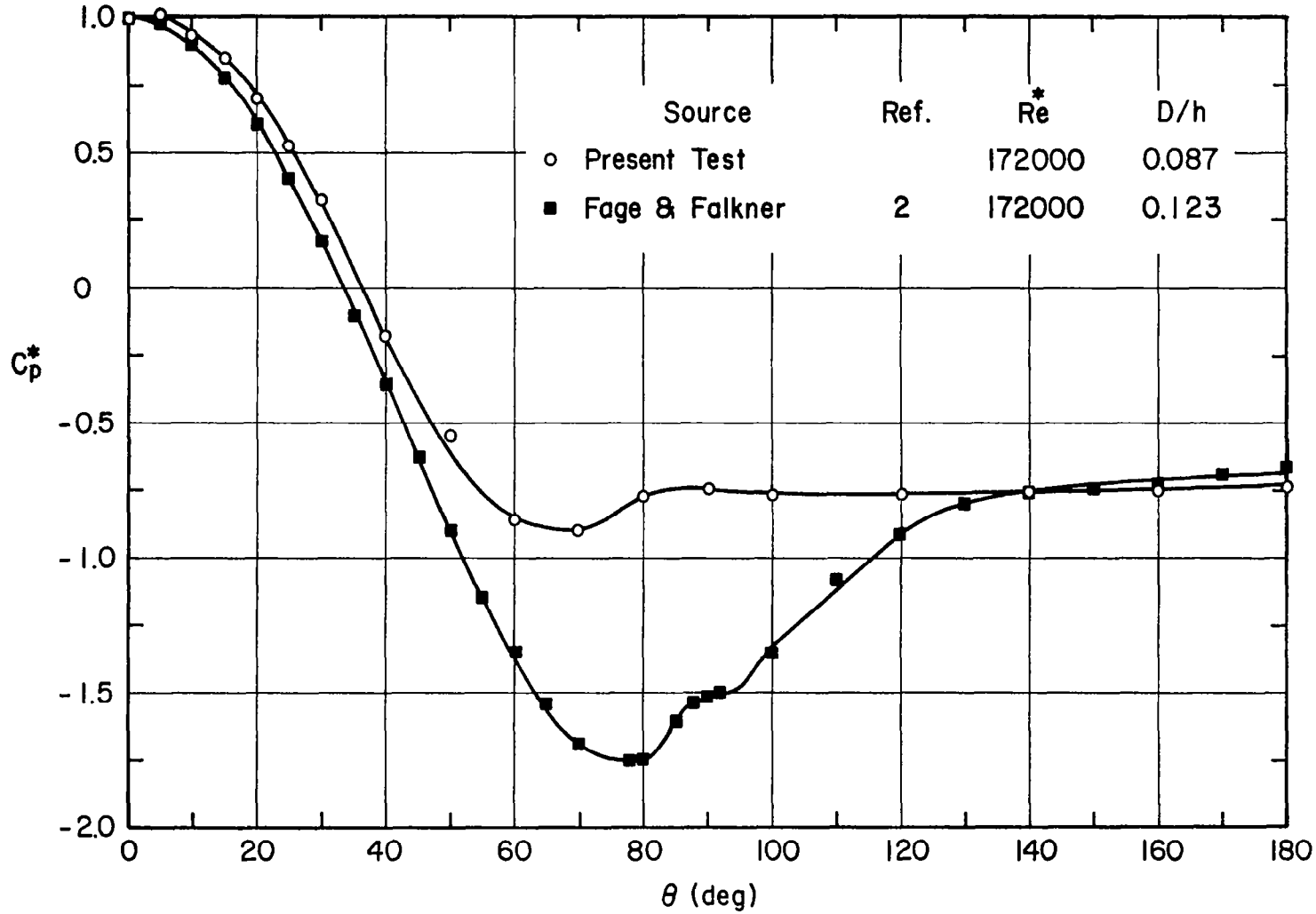

Fig. 5.8 Pressure coefficient (corrected) distribution comparison.

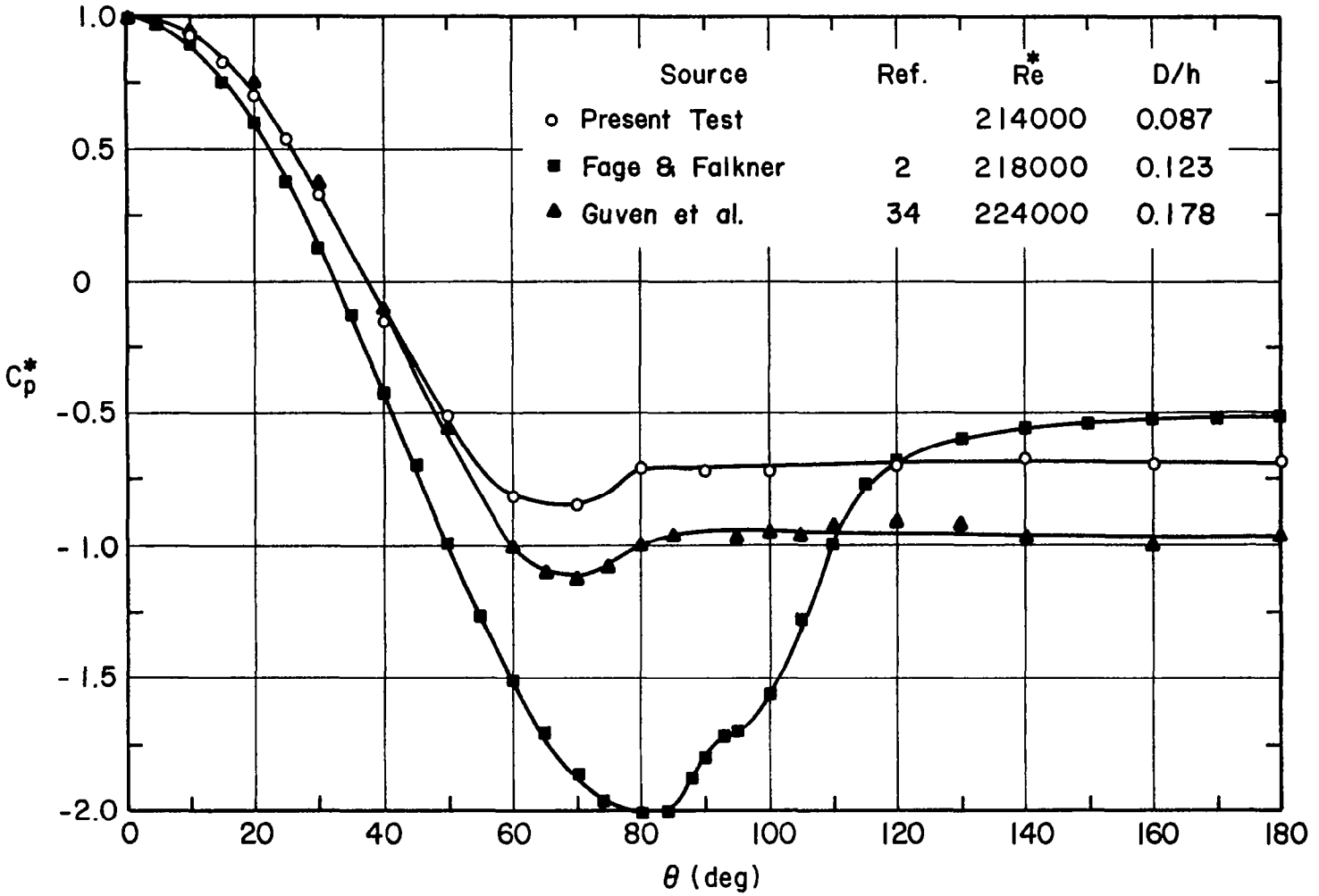

Fig. 5.9 Pressure coefficient (corrected) distribution comparison.

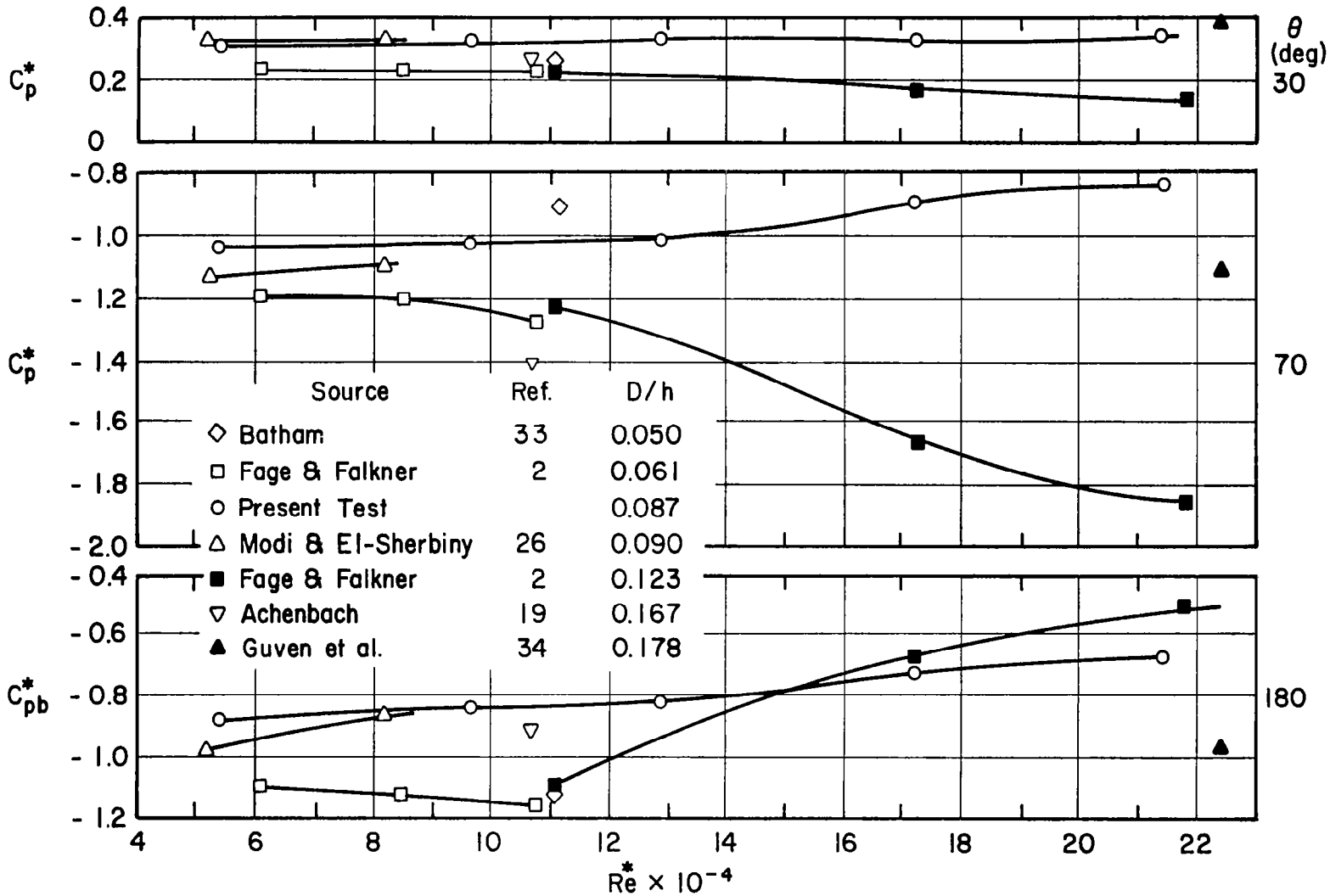

Fig. 5.10 Comparison of pressure coefficient (corrected) distribution as function of Reynolds number at three peripheral angles.

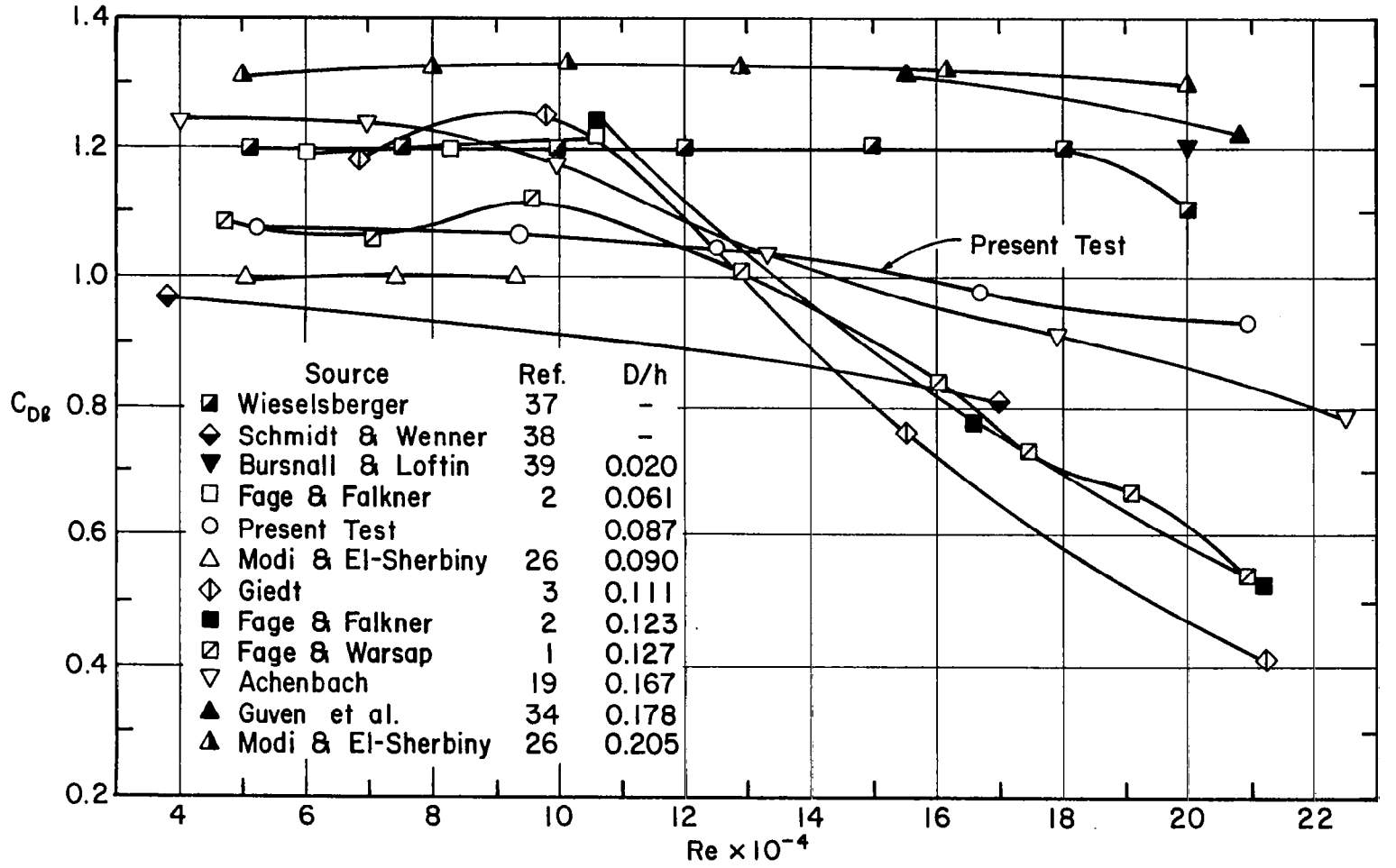

Fig. 5.11 Drag coefficient in smooth incident flow as function of Reynolds number and comparison with other results.

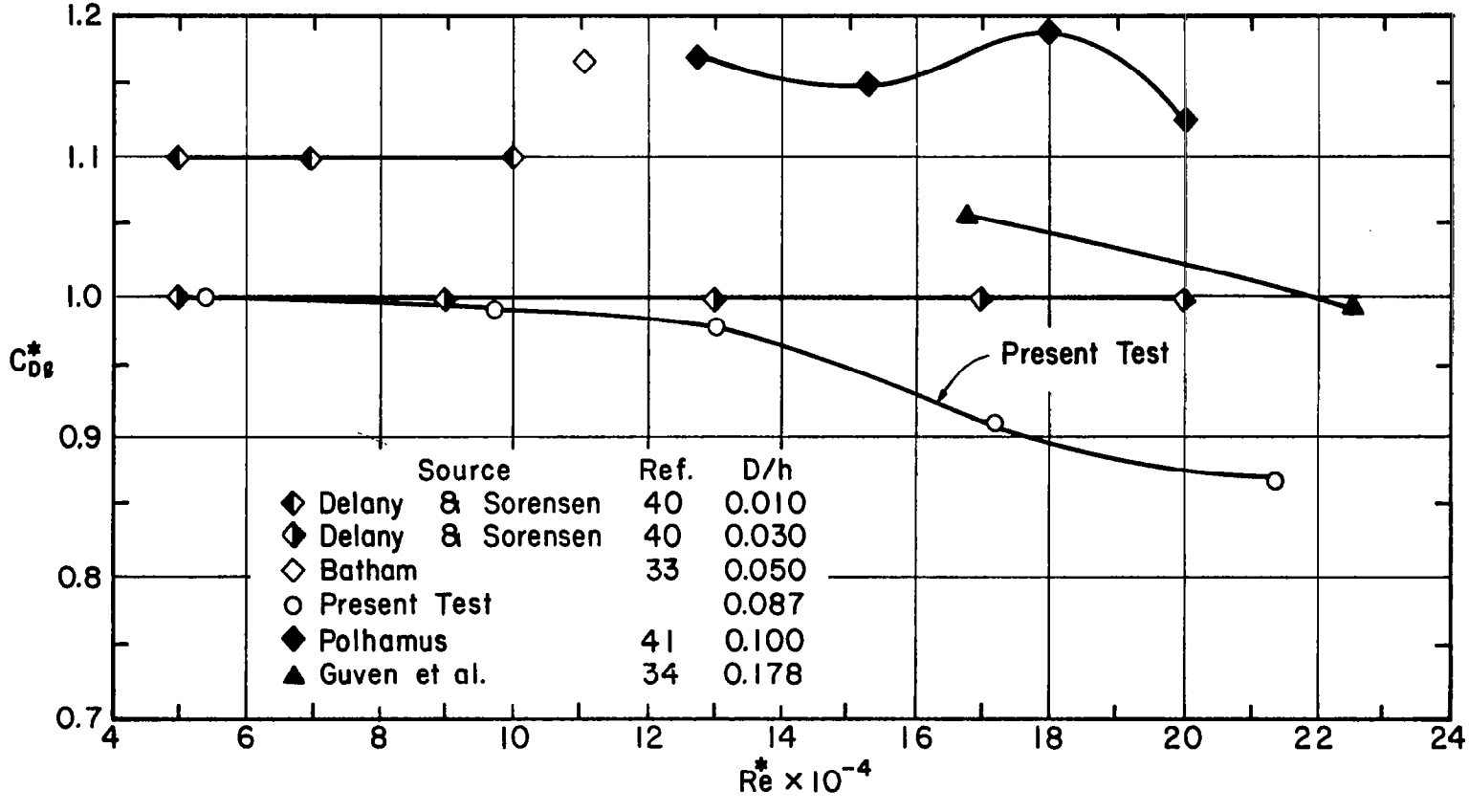

Fig. 5.12 Drag coefficient (corrected) in smooth incident flow as function of Reynolds number and comparison with other results.

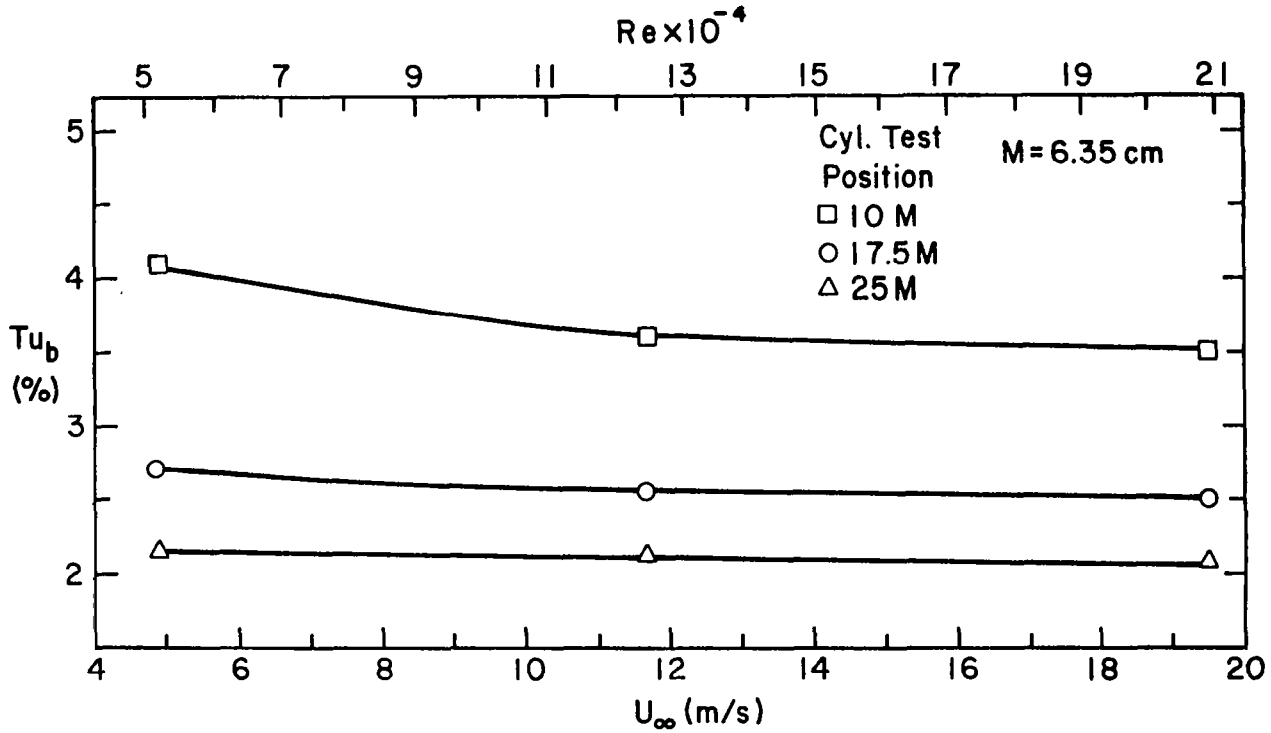

Fig. 6.1 Background axial turbulence intensity at cylinder (Cyl.) test position as function of freestream velocity and corresponding cylinder-diameter Reynolds number.

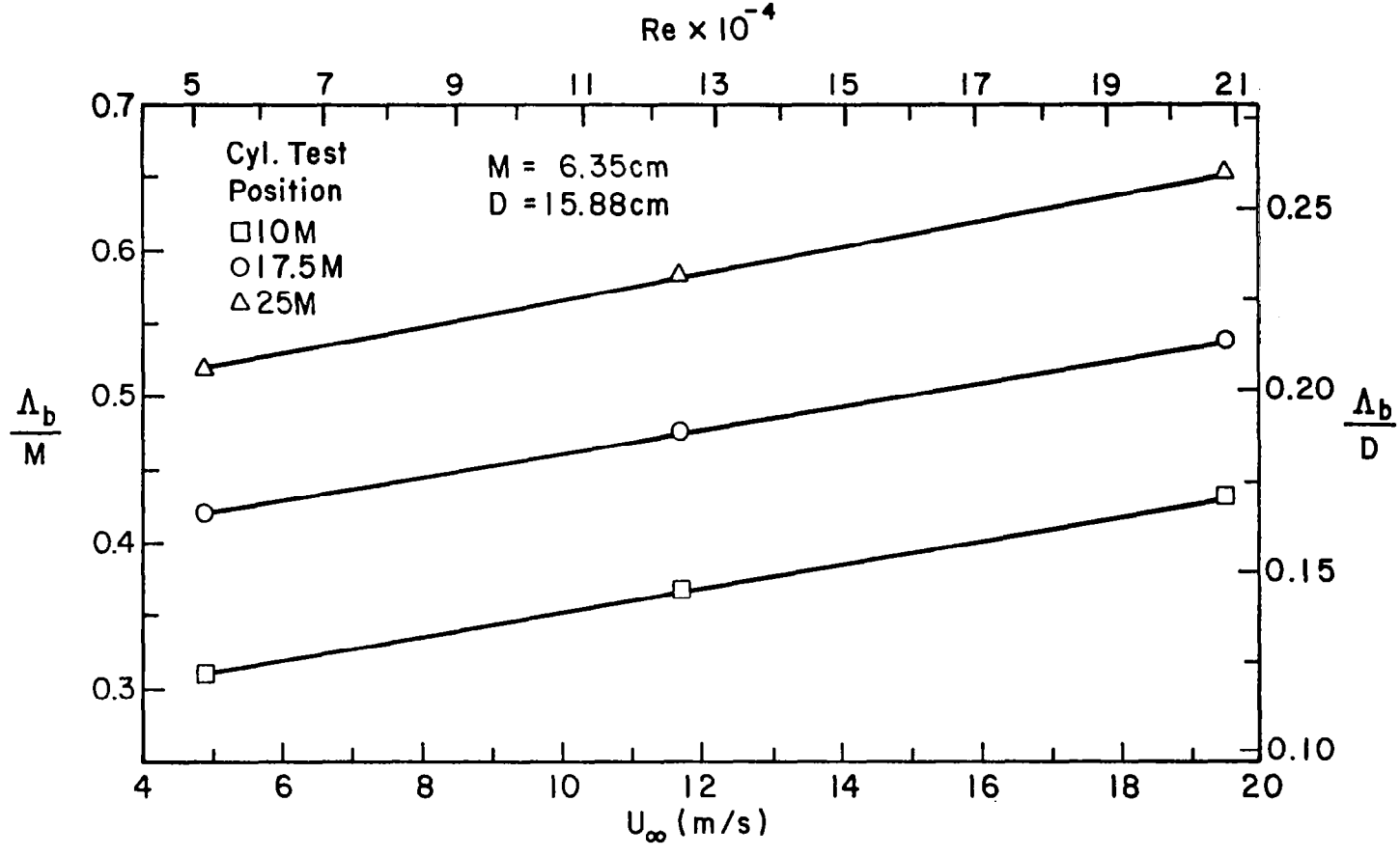

Fig. 6.2 Dimensionless longitudinal integral scale of background turbulence at cylinder (Cyl.) test position as function of freestream velocity and corresponding cylinder-diameter Reynolds number.

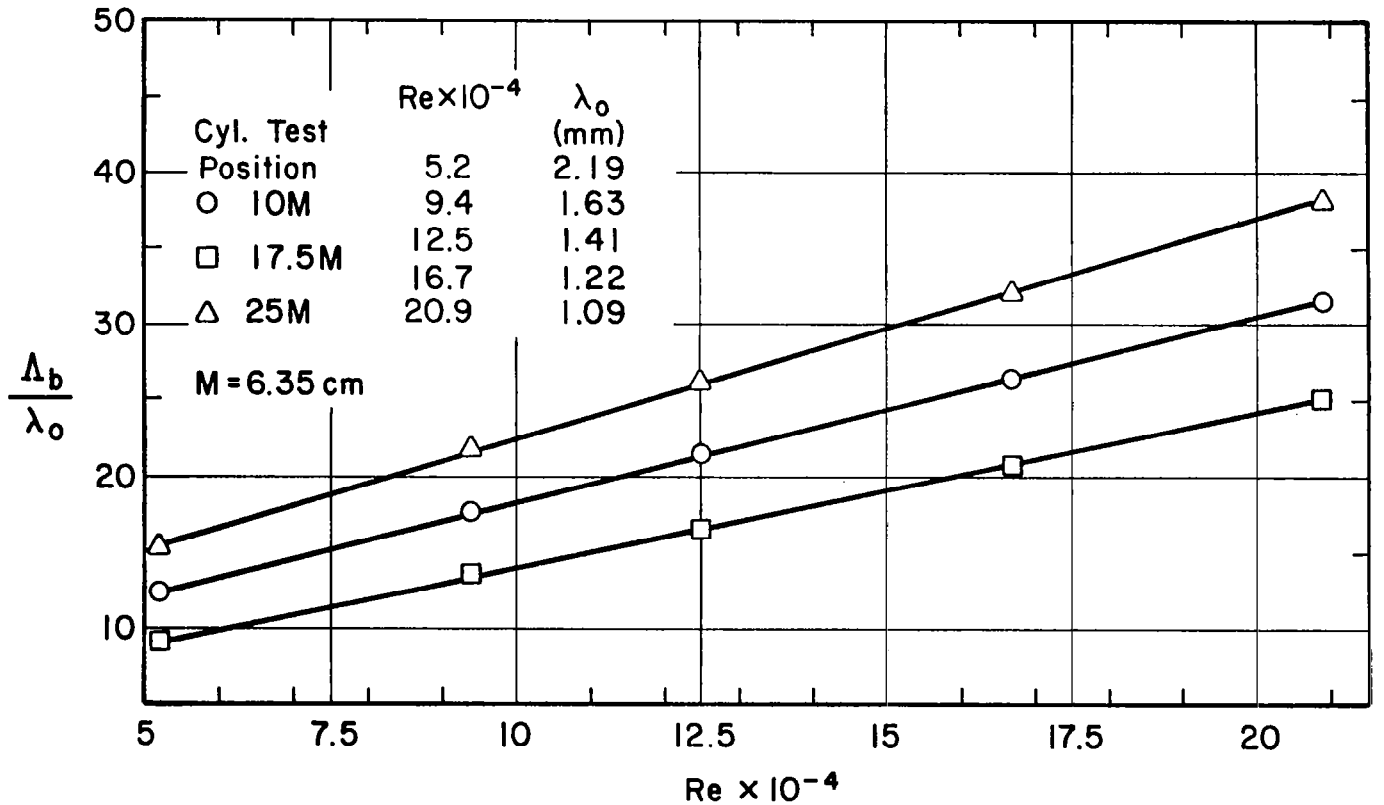

Fig. 6.3 Ratio of background turbulence longitudinal integral scale at cylinder (Cyl.) test position to neutral scale of stagnation flow as function of cylinder-diameter Reynolds number.

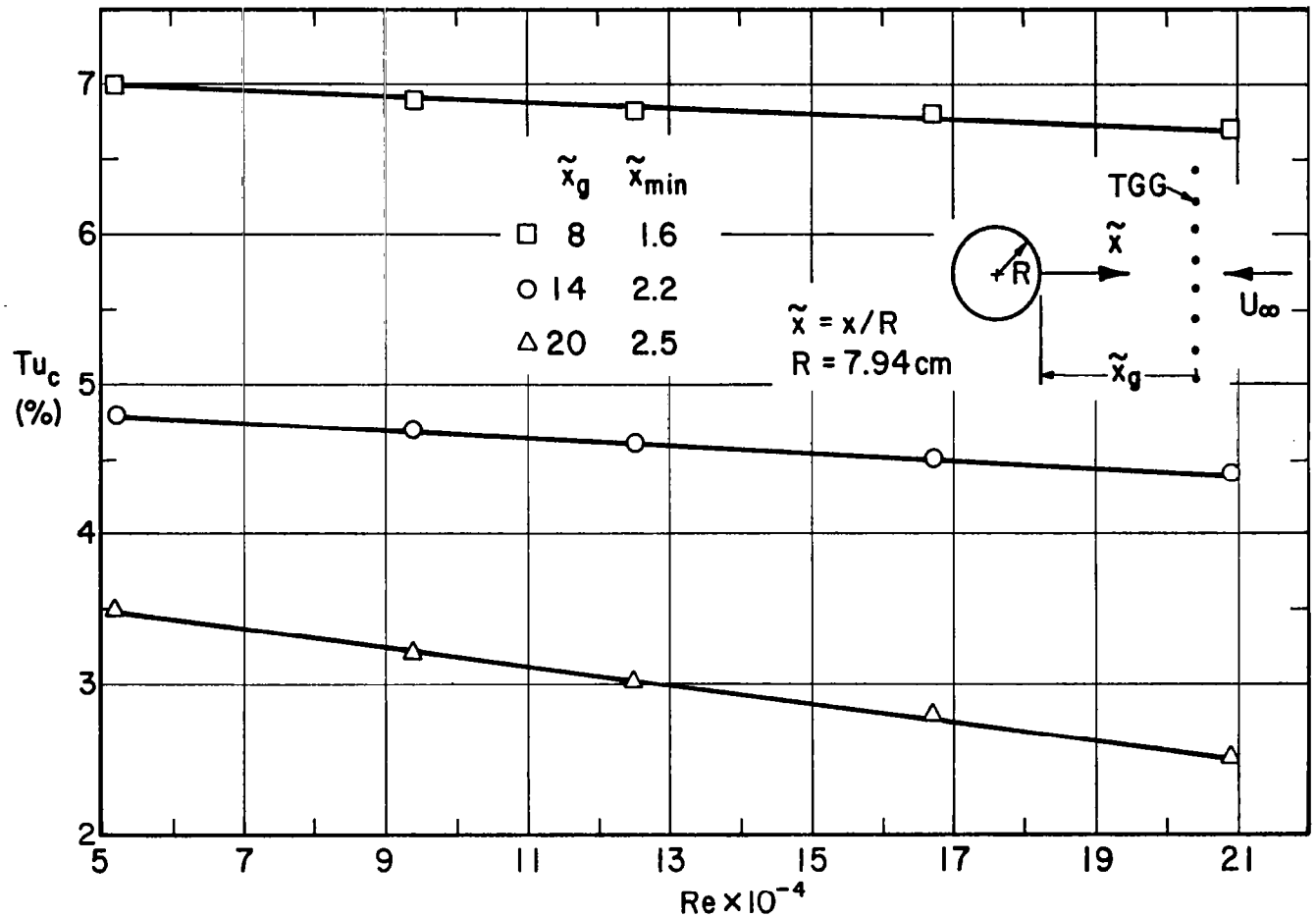

Fig. 6.4 Critical turbulence intensity as function of Reynolds number for three turbulence-generating grid (TGG) positions.

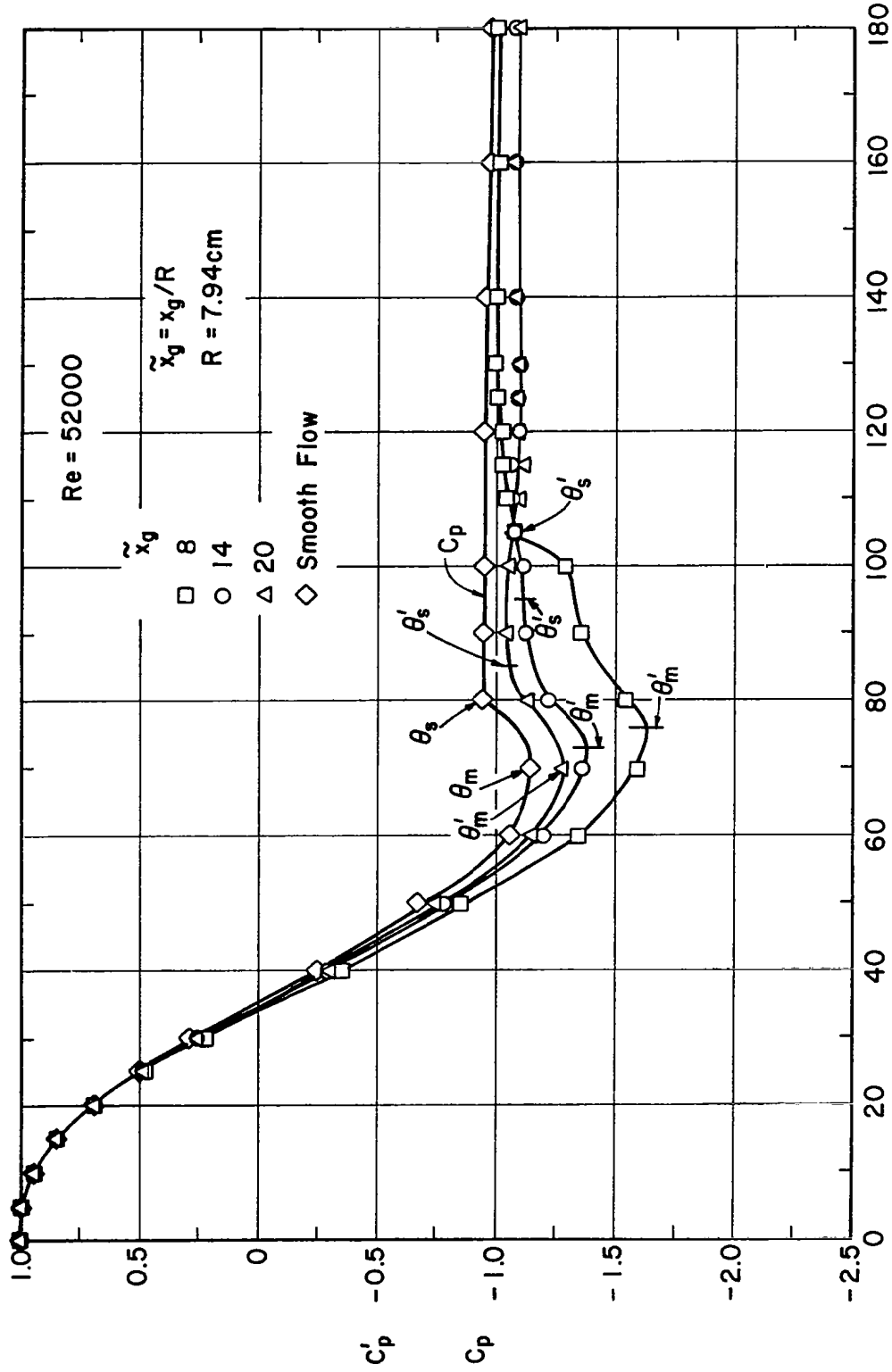

Fig. 6.5 Mean pressure coefficient distribution in turbulent incident flow and in smooth incident flow at Re = 5.2×10^4.

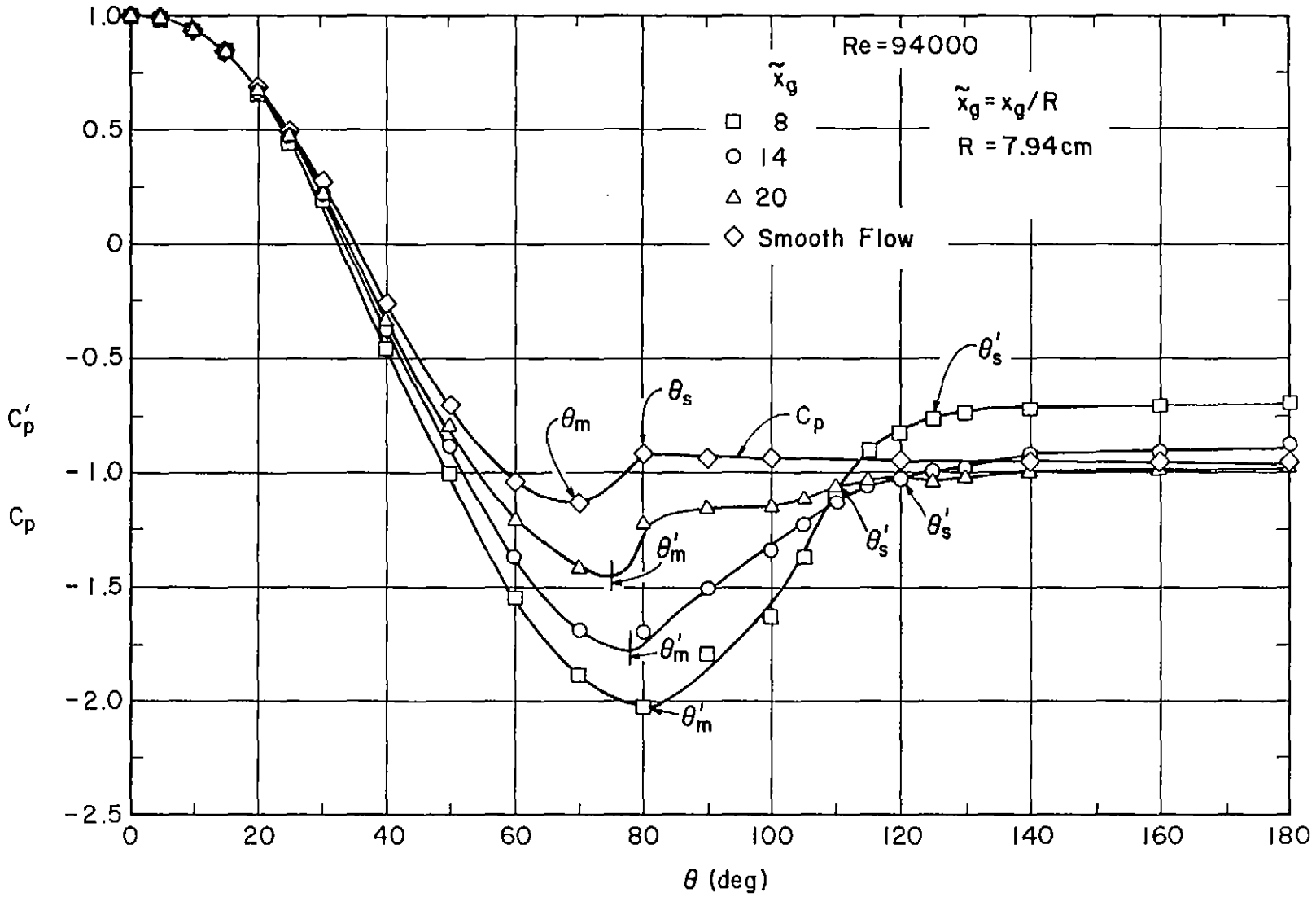

Fig. 6.6 Mean pressure coefficient distribution in turbulent incident flow and in smooth incident flow at Re = 9.4×10^4.

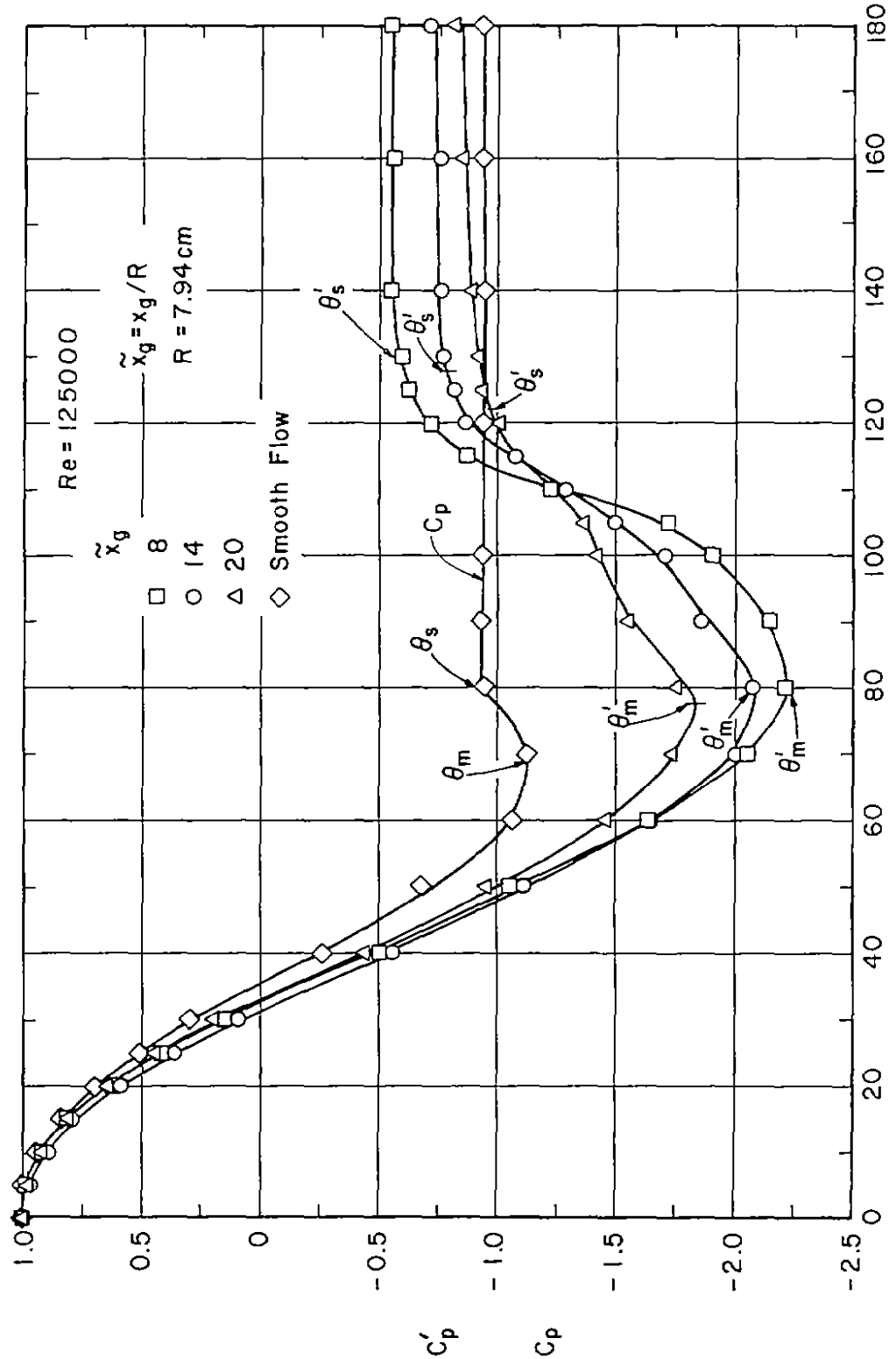

Fig. 6.7 Mean pressure coefficient distribution in turbulent incident flow and in smooth incident flow at Re = 1.25×10^5.

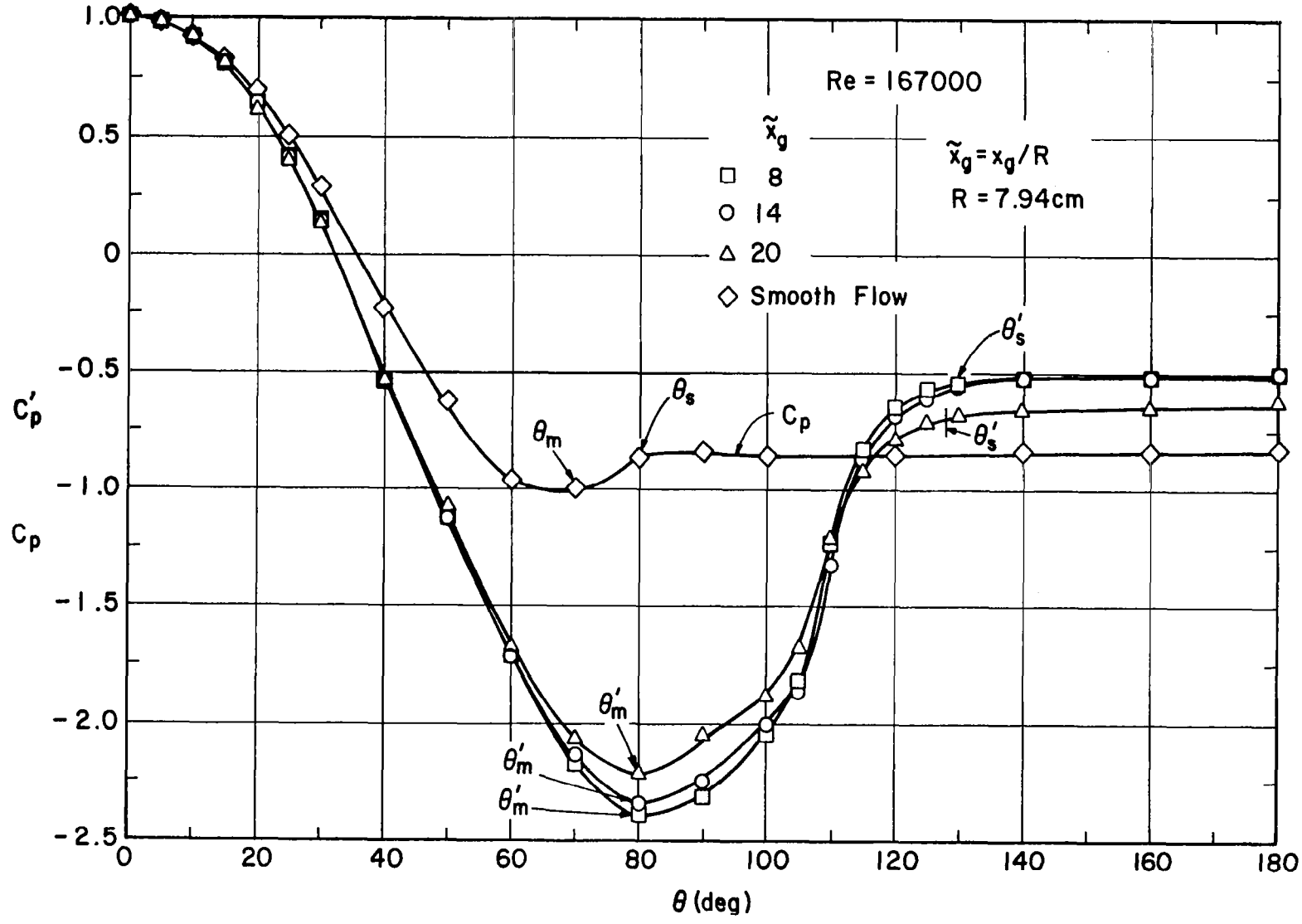

Fig. 6.8 Mean pressure coefficient distribution in turbulent incident flow and in smooth incident flow at Re = 1.67×10^5.

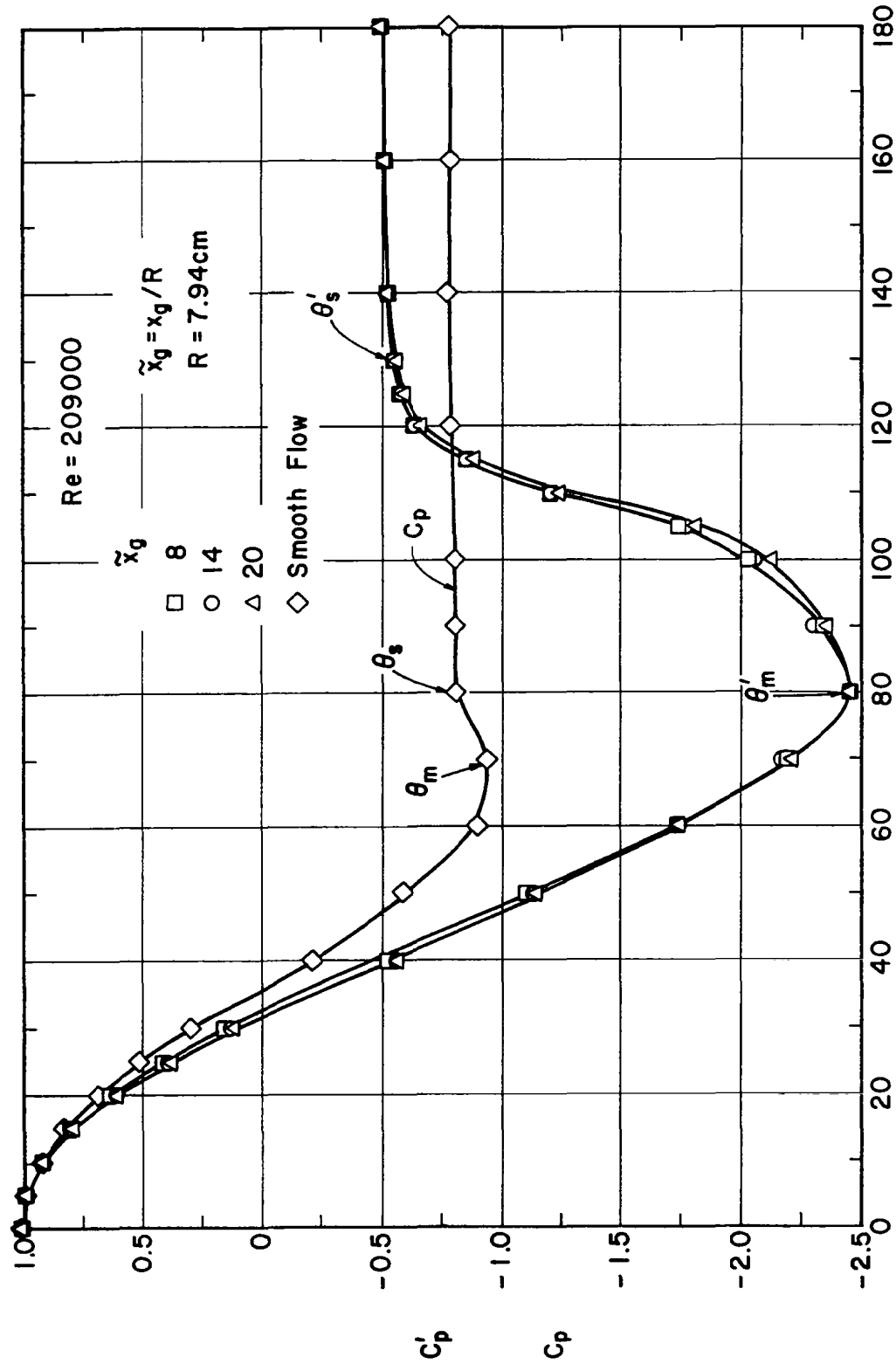

Fig. 6.9 Mean pressure coefficient distribution in turbulent incident flow and in smooth incident flow at Re = 2.09×10^5.

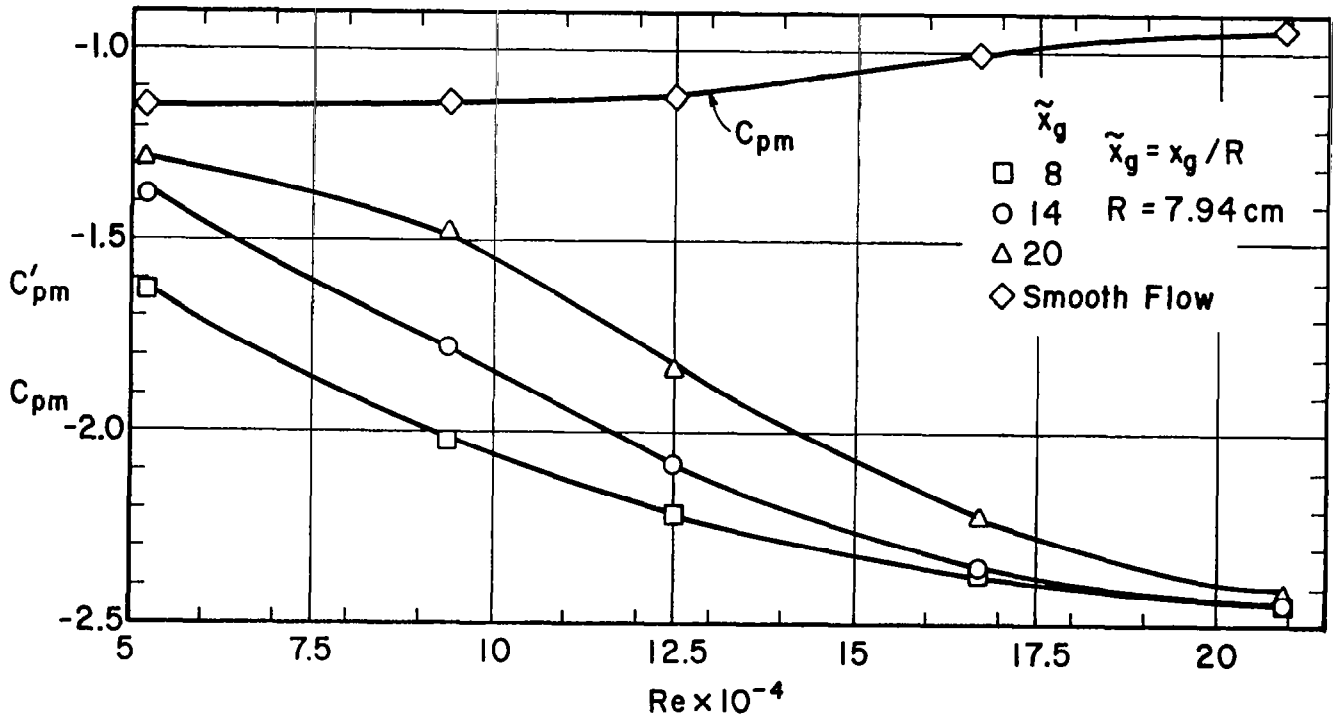

Fig. 6.10 Minimum pressure coefficient in turbulent and smooth incident flows as function of Reynolds number.

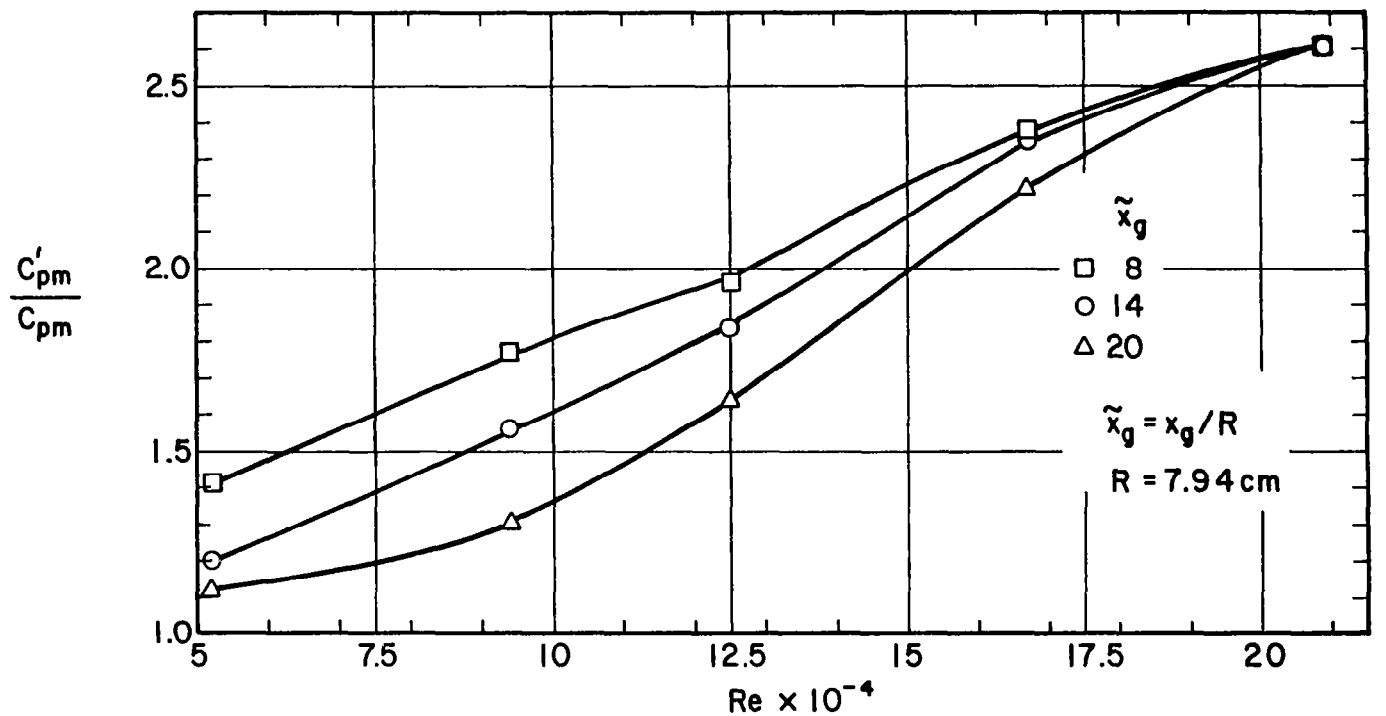

Fig. 6.11 Ratio of minimum pressure coefficient in turbulent incident flow to its counterpart in smooth incident flow as function of Reynolds number.

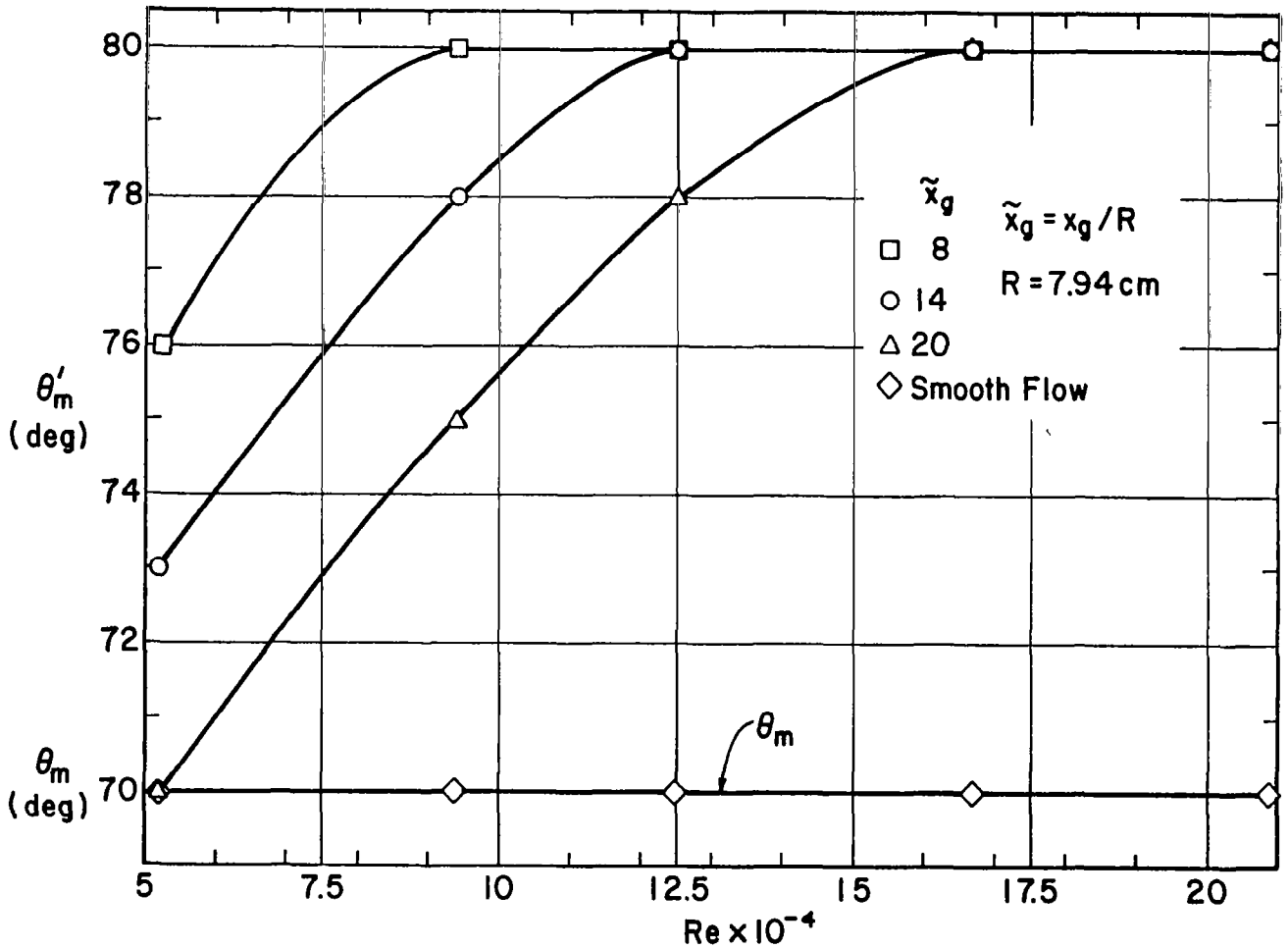

Fig. 6.12 Angular position of minimum pressure in turbulent and smooth incident flows as function of Reynolds number.

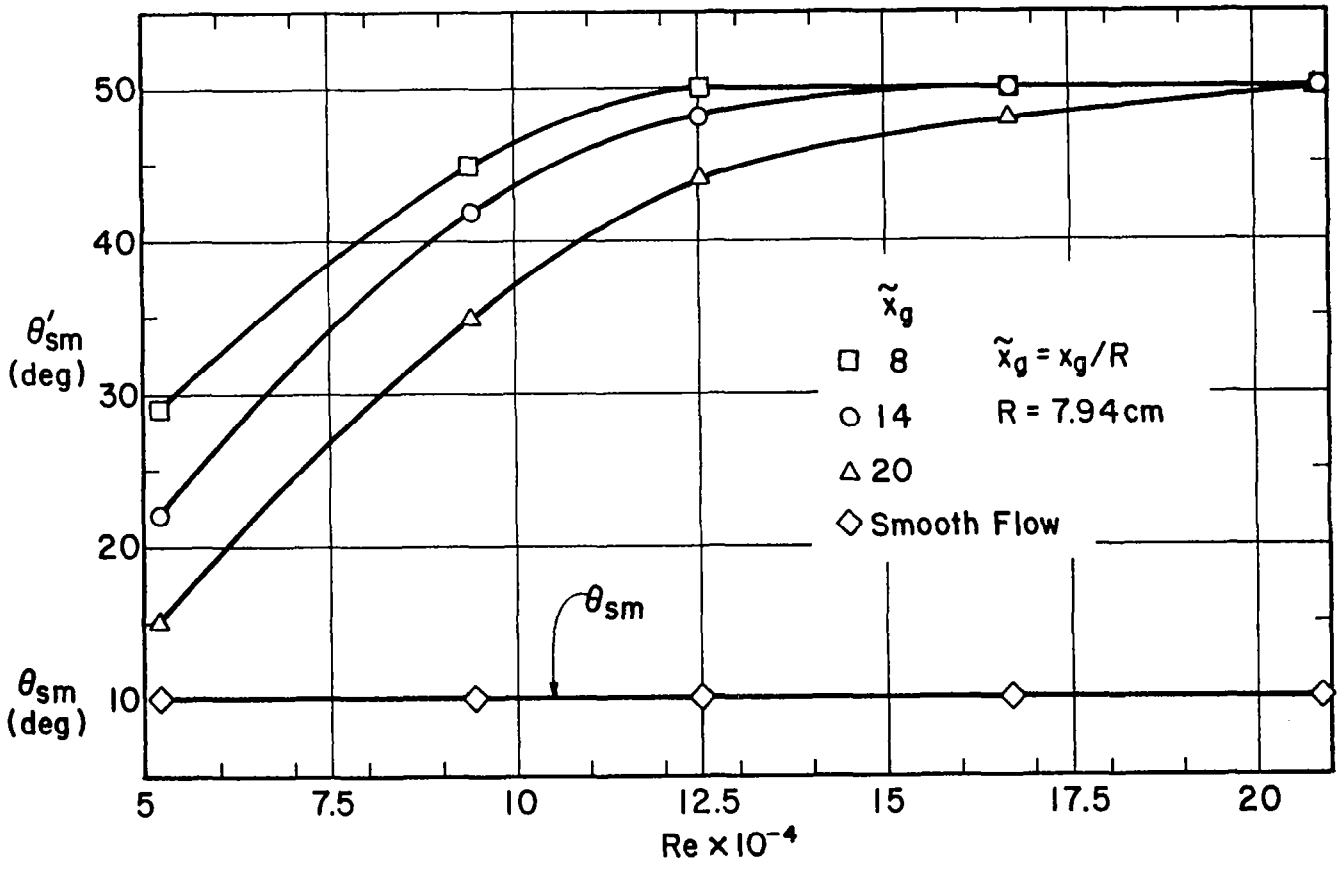

Fig. 6.13 Angular extent of adverse pressure gradient region in turbulent and smooth incident flows as function of Reynolds number.

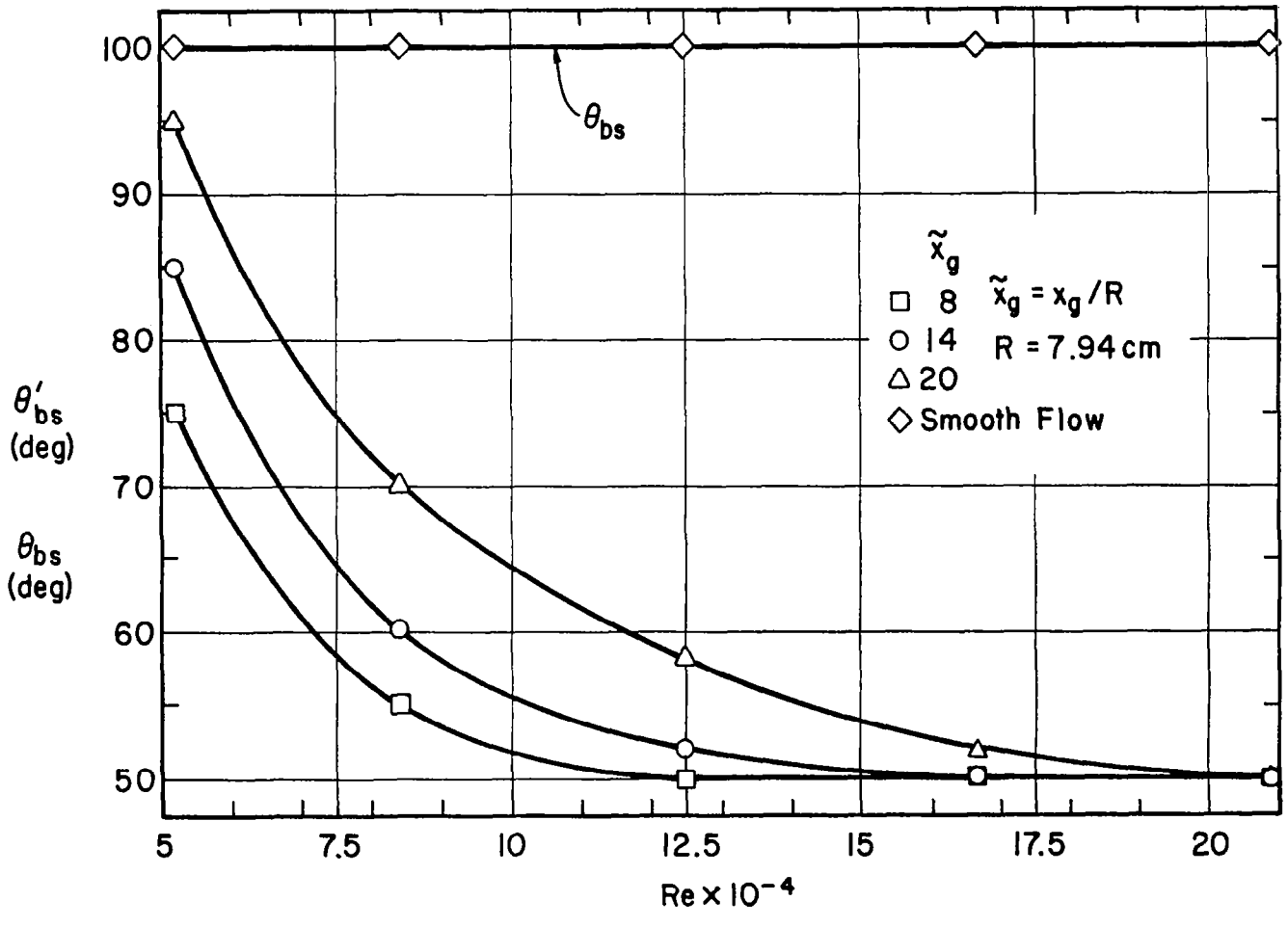

Fig. 6.14 Angular extent of base region in turbulent and smooth incident flows as function of Reynolds number.

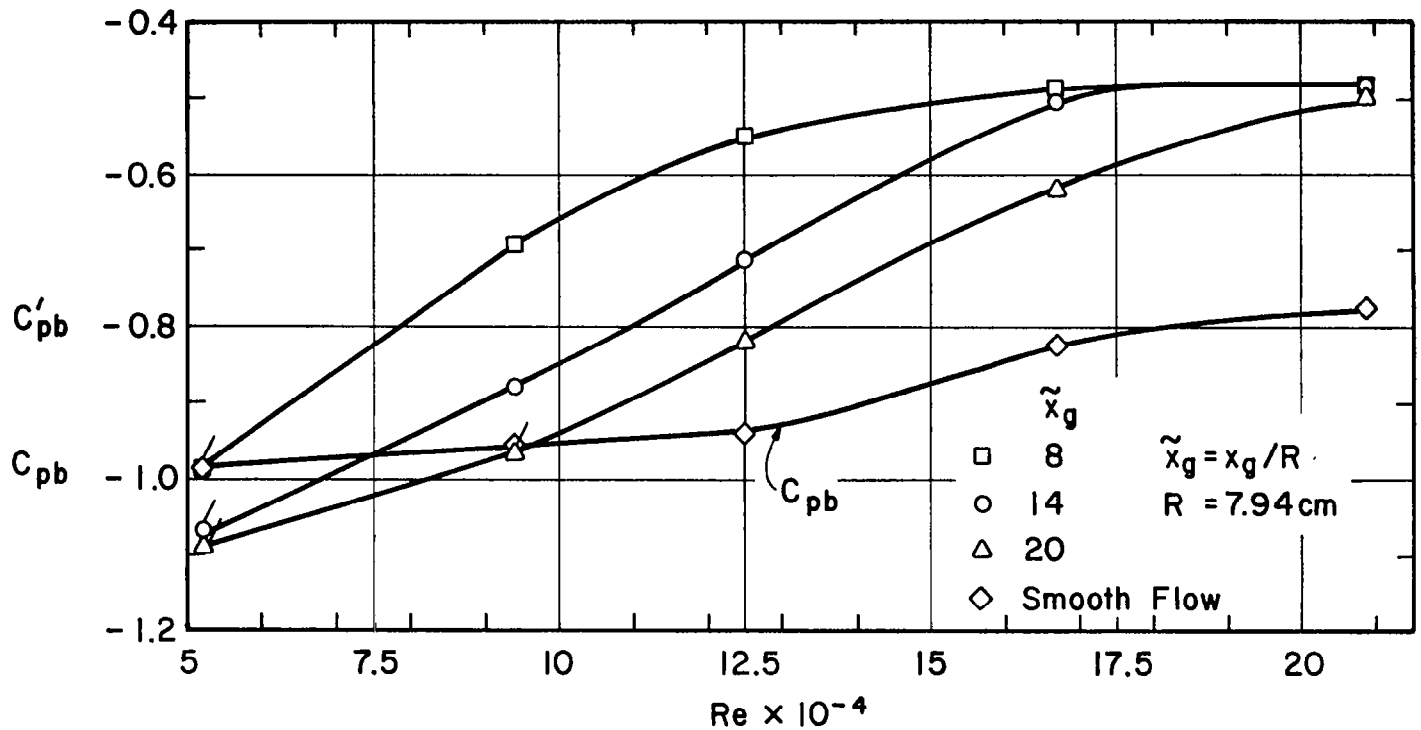

Fig. 6.15 Base pressure coefficient in turbulent and smooth incident flows as function of Reynolds number.

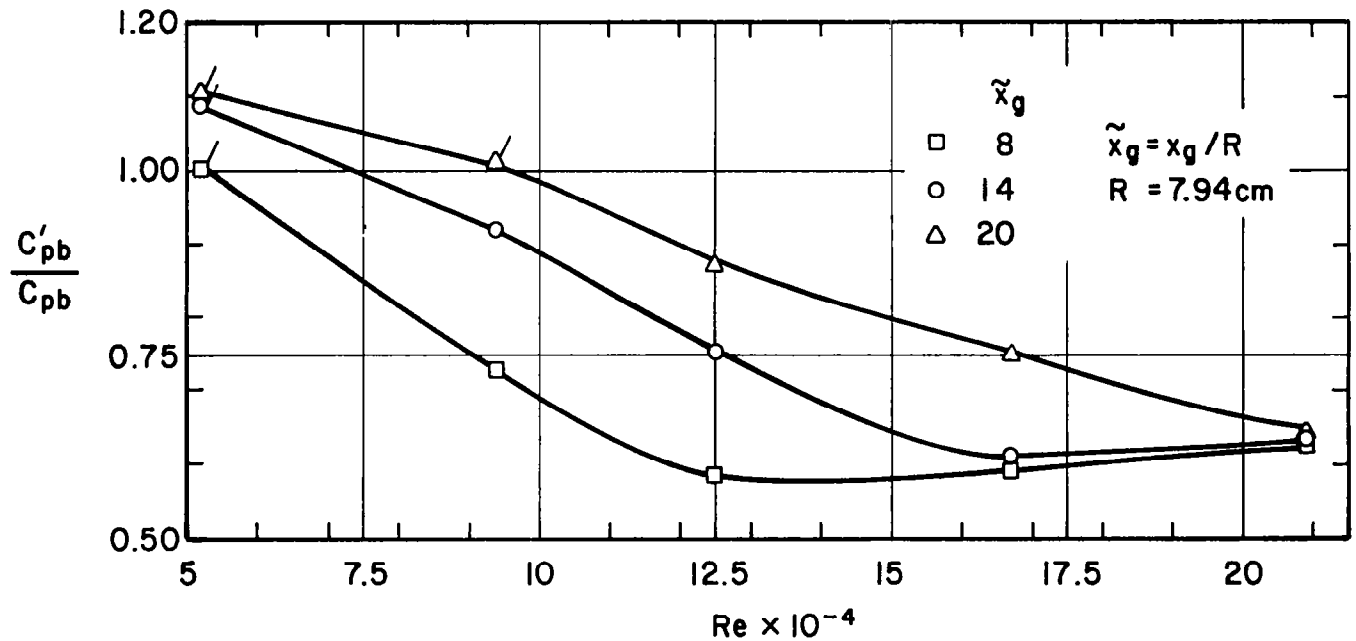

Fig. 6.16 Ratio of base pressure coefficient in turbulent incident flow to its counterpart in smooth incident flow as function of Reynolds number.

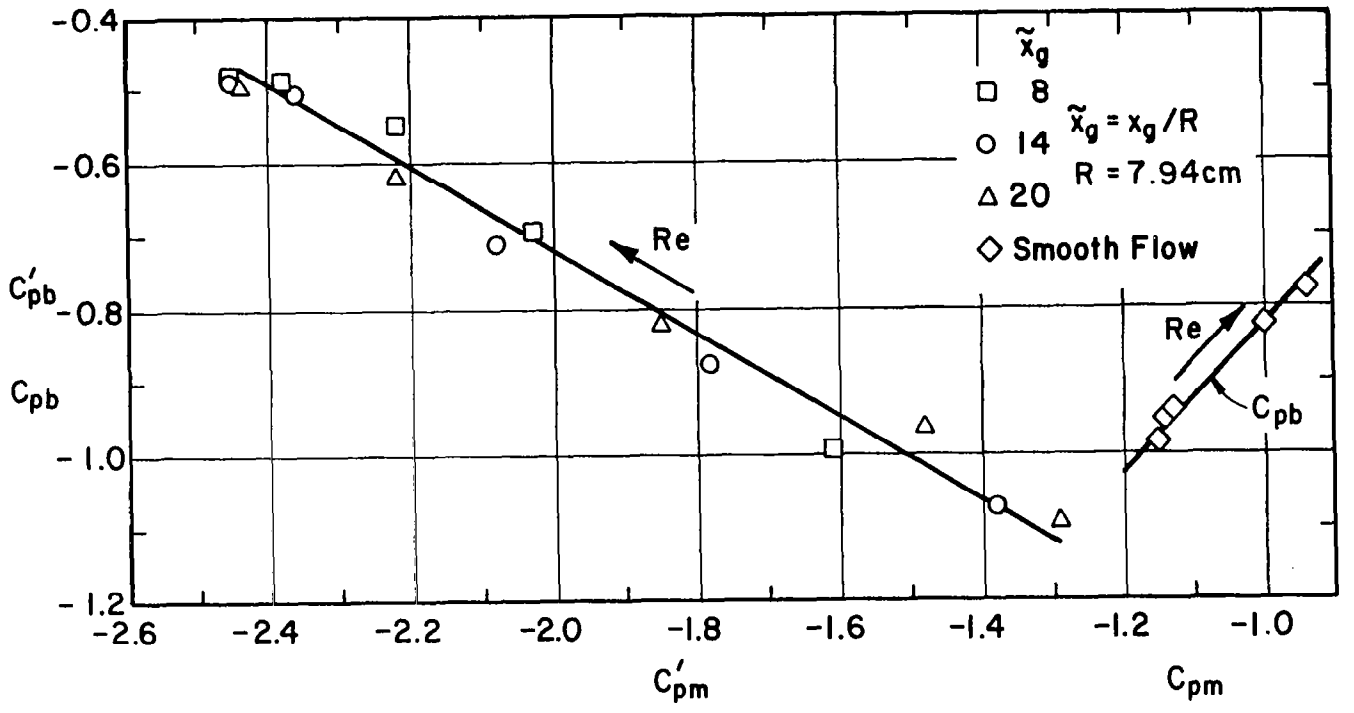

Fig. 6.17 Variation of base pressure coefficient with varying minimum pressure coefficient in turbulent and smooth incident flows.

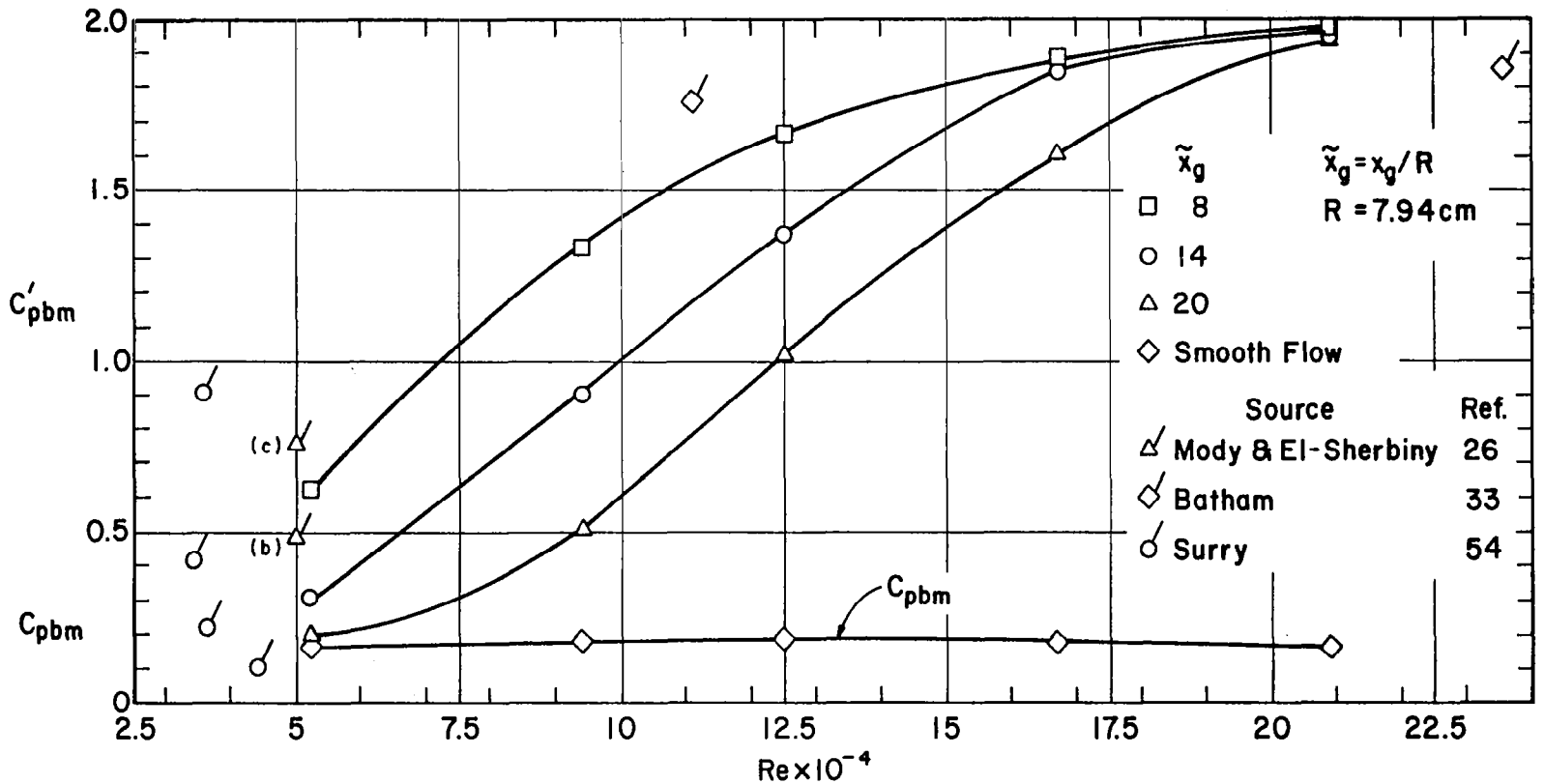

Fig. 6.18 Pressure rise coefficient in turbulent and smooth incident flows as function of Reynolds number.

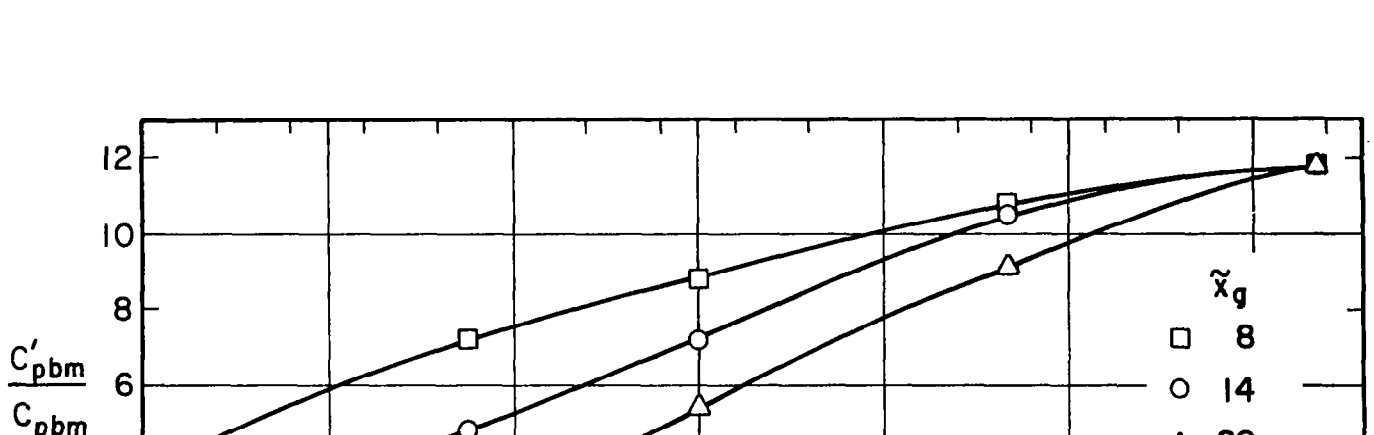

Fig. 6.19 Ratio of pressure rise coefficient in turbulent incident flow to its counterpart in smooth incident flow as function of Reynolds number.

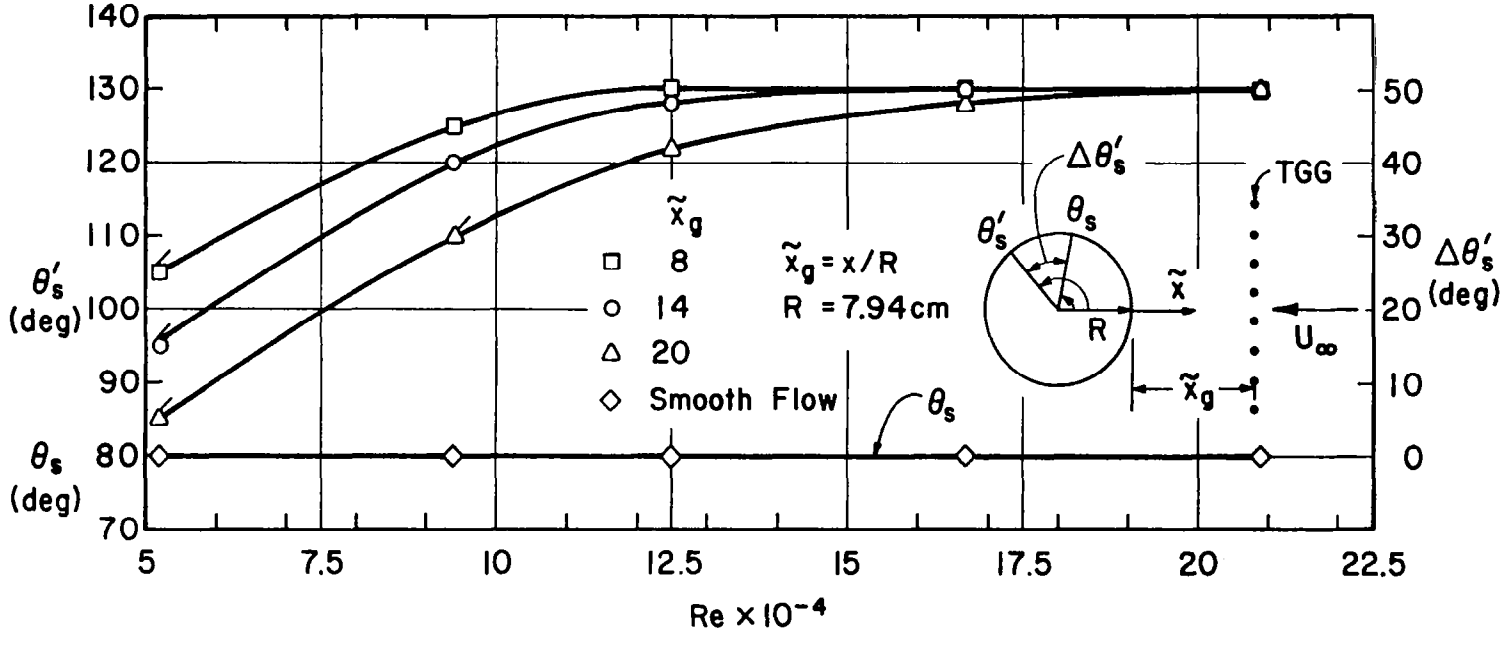

Fig. 6.20 Variation of separation angle in turbulent and smooth incident flows and of their difference with increasing Reynolds number (TGG means turbulence-generating grid).

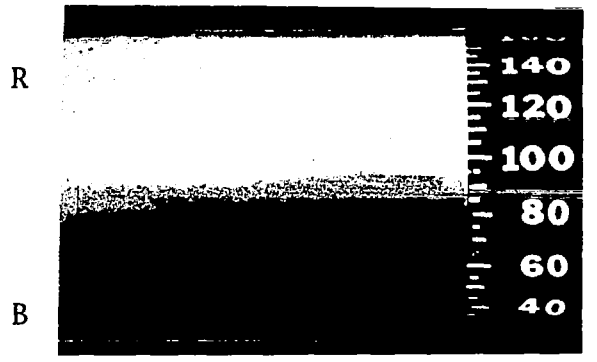

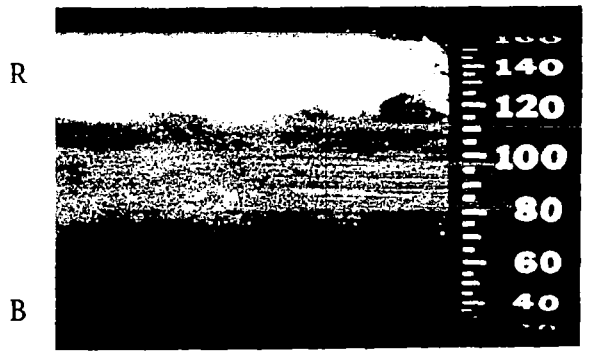

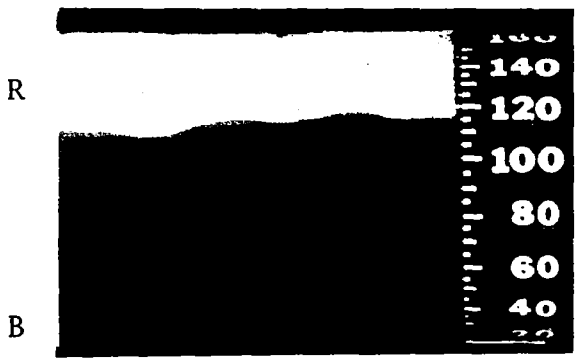

Re ($\times 10^4$)	$\tilde{x}_g$	θ'_s (deg)
5.2	14	95
7.5	8	115
12.5	20	120

Fig. 6.21 View of separation angle in turbulent incident flow at three selected subcritical Reynolds numbers; B: Blue, attached flow; R: Red, separated flow.

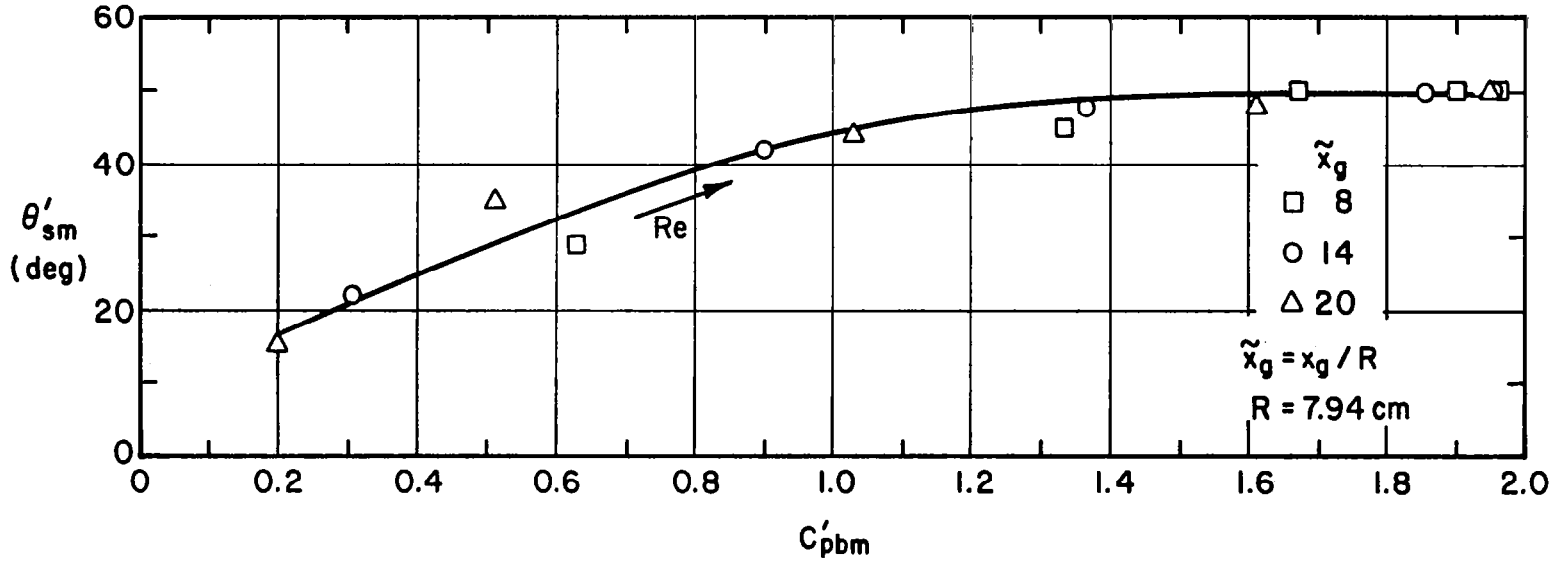

Fig. 6.22 Variation of angular extent of adverse pressure gradient region as function of pressure rise coefficient.

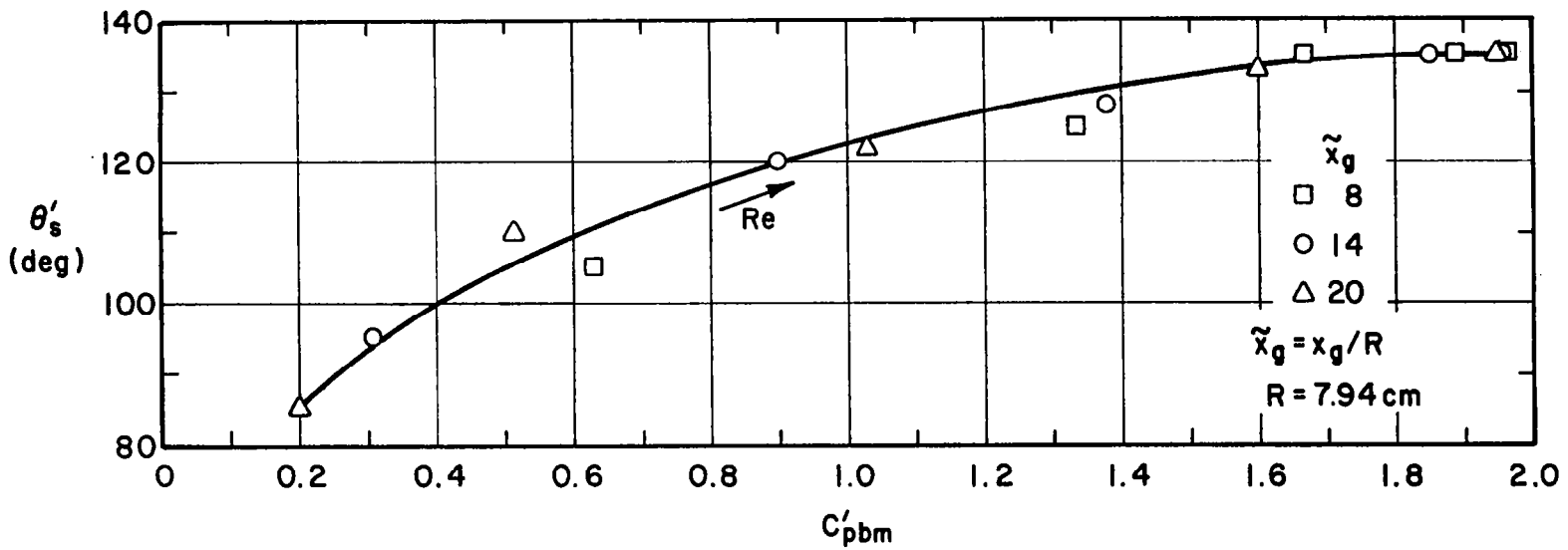

Fig. 6.23 Variation of separation angle as function of pressure rise coefficient.

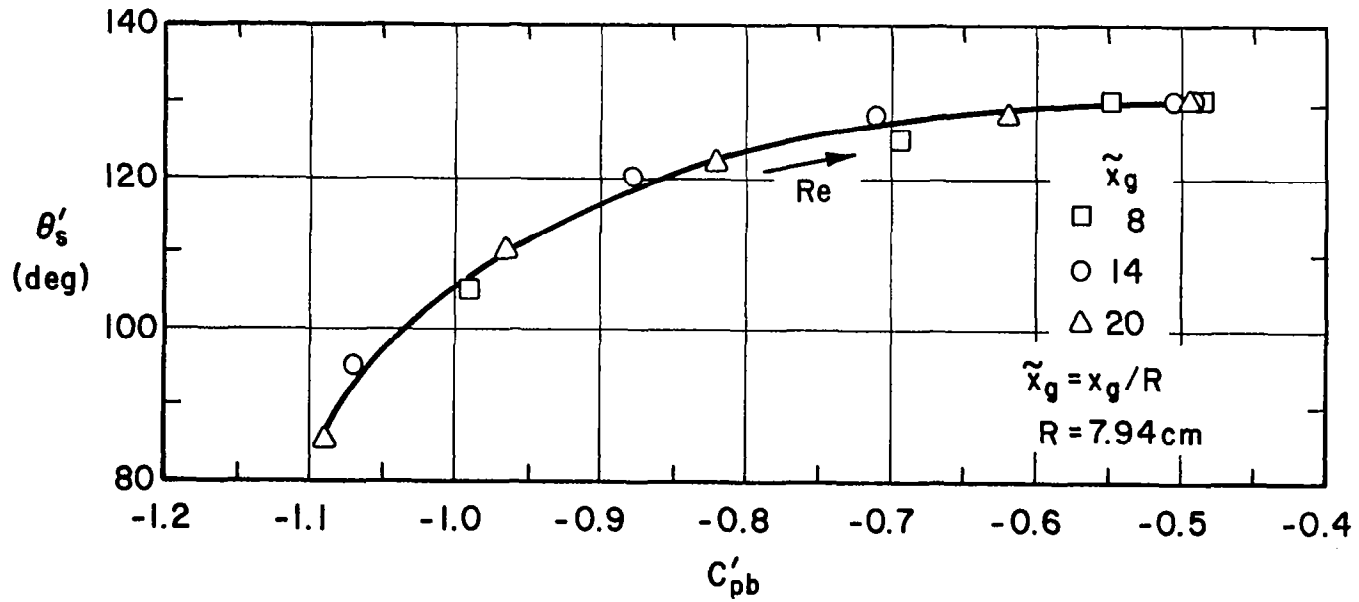

Fig. 6.24 Variation of separation angle as function of base pressure coefficient.

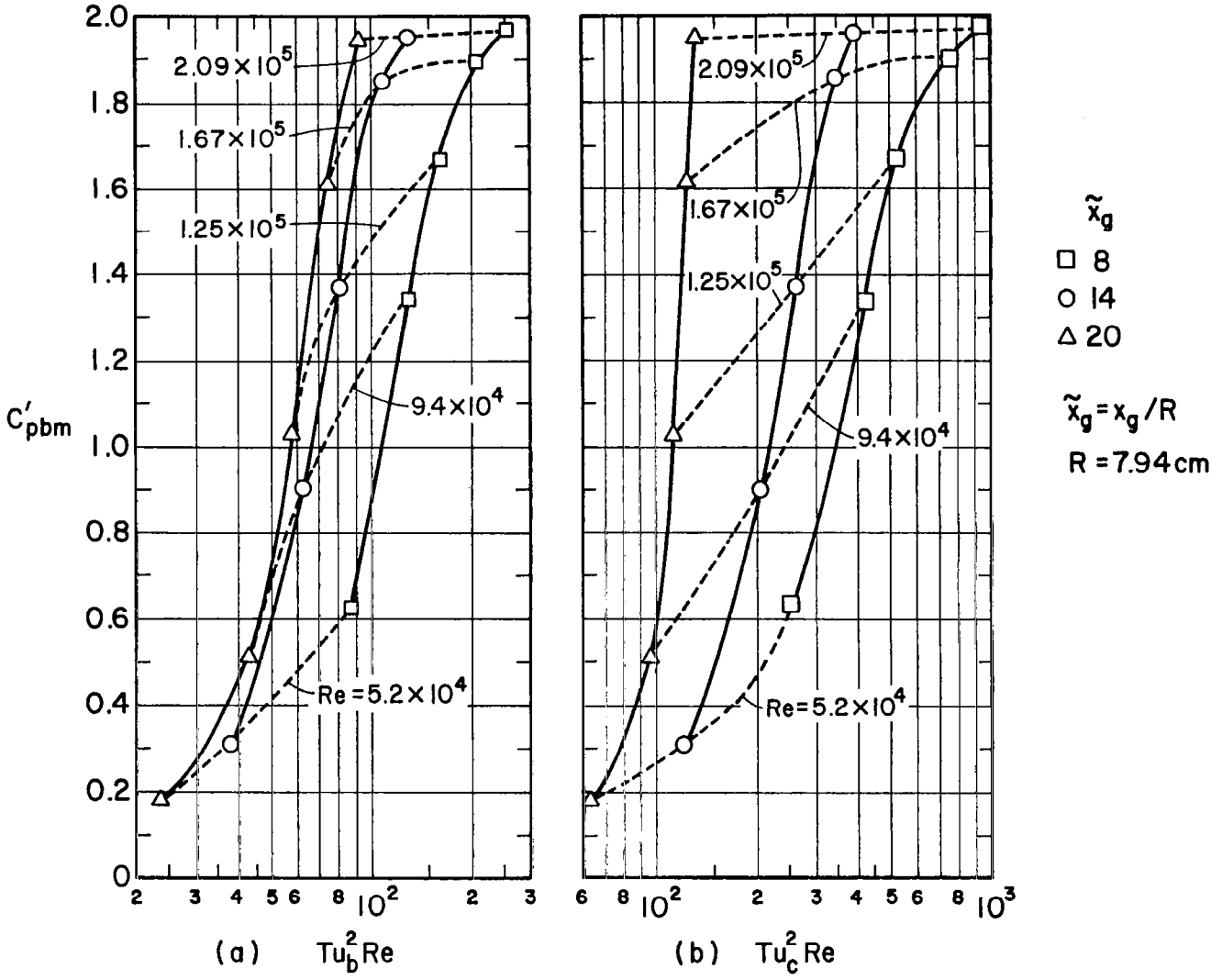

Fig. 6.25 Pressure rise coefficient as function of turbulence parameter based on (a) background turbulence intensity and (b) critical turbulence intensity.

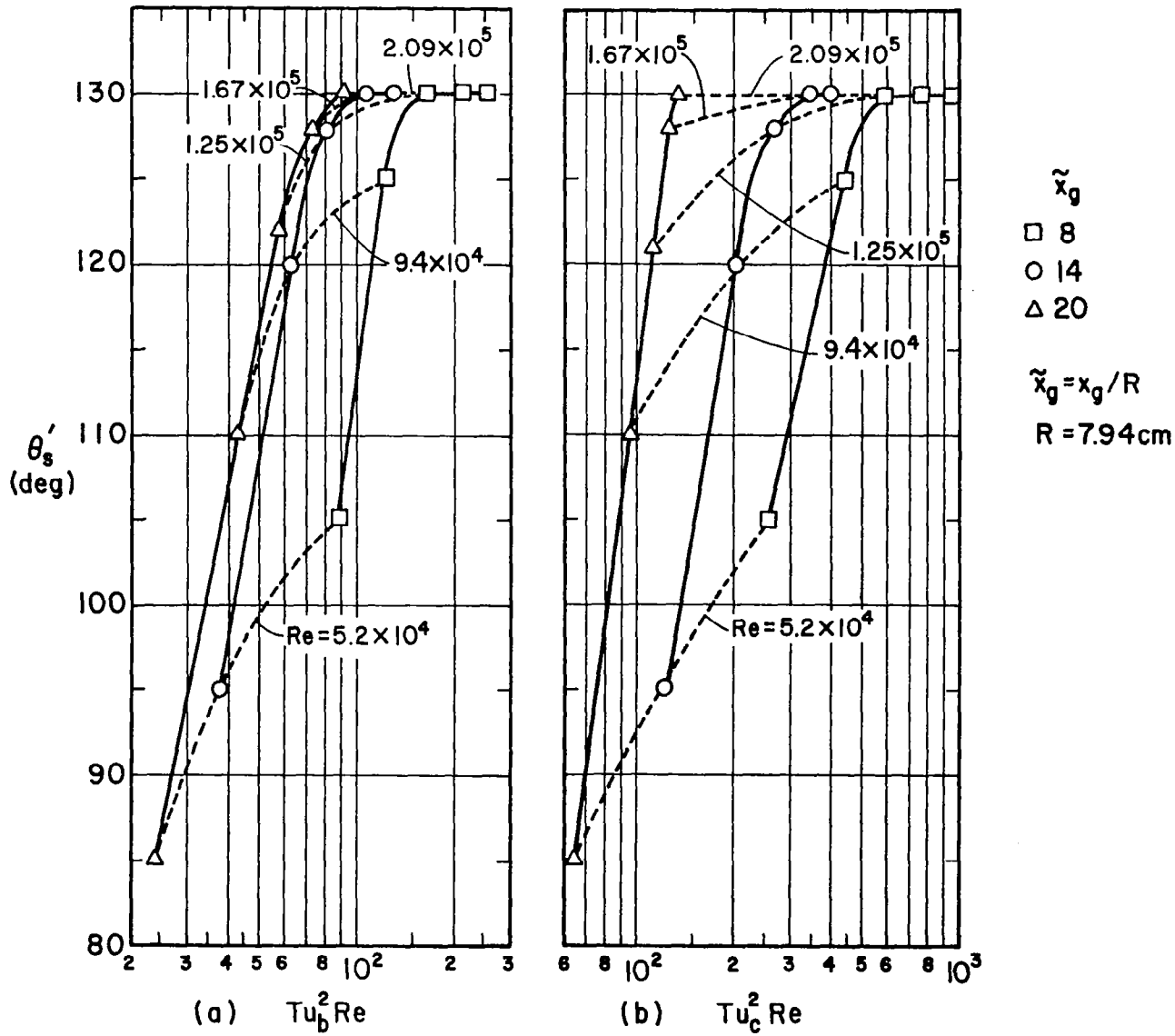

Fig. 6.26 Separation angle as function of turbulence parameter based on (a) background turbulence intensity and (b) critical turbulence intensity.

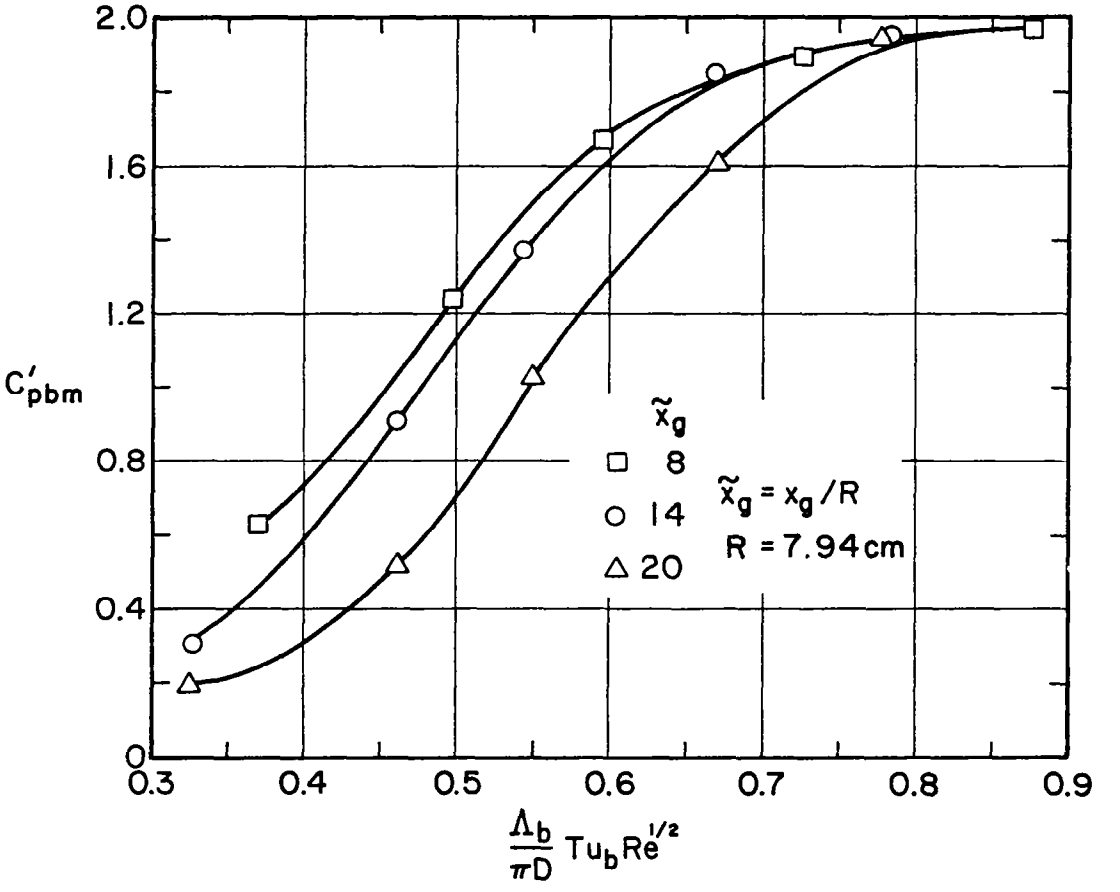

Fig. 6.27 Variation of pressure rise coefficient with increasing turbulent separation parameter.

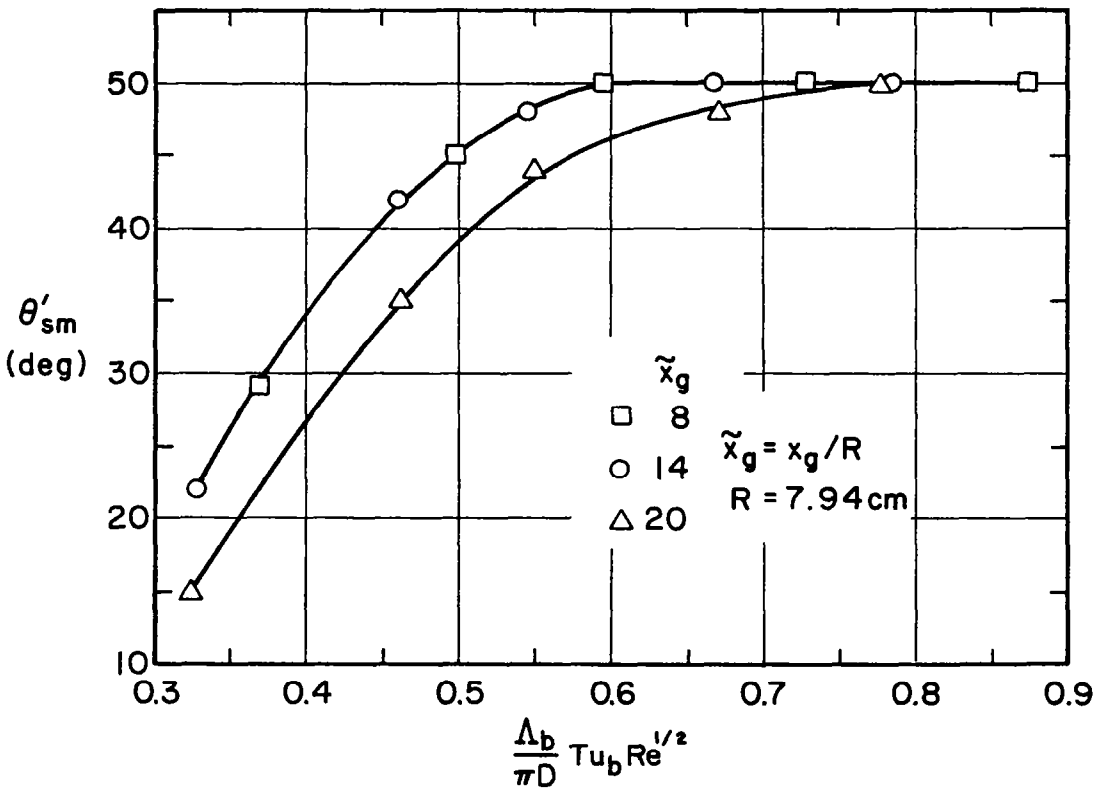

Fig. 6.28 Variation of angular extent of adverse pressure gradient region with increasing turbulent separation parameter.

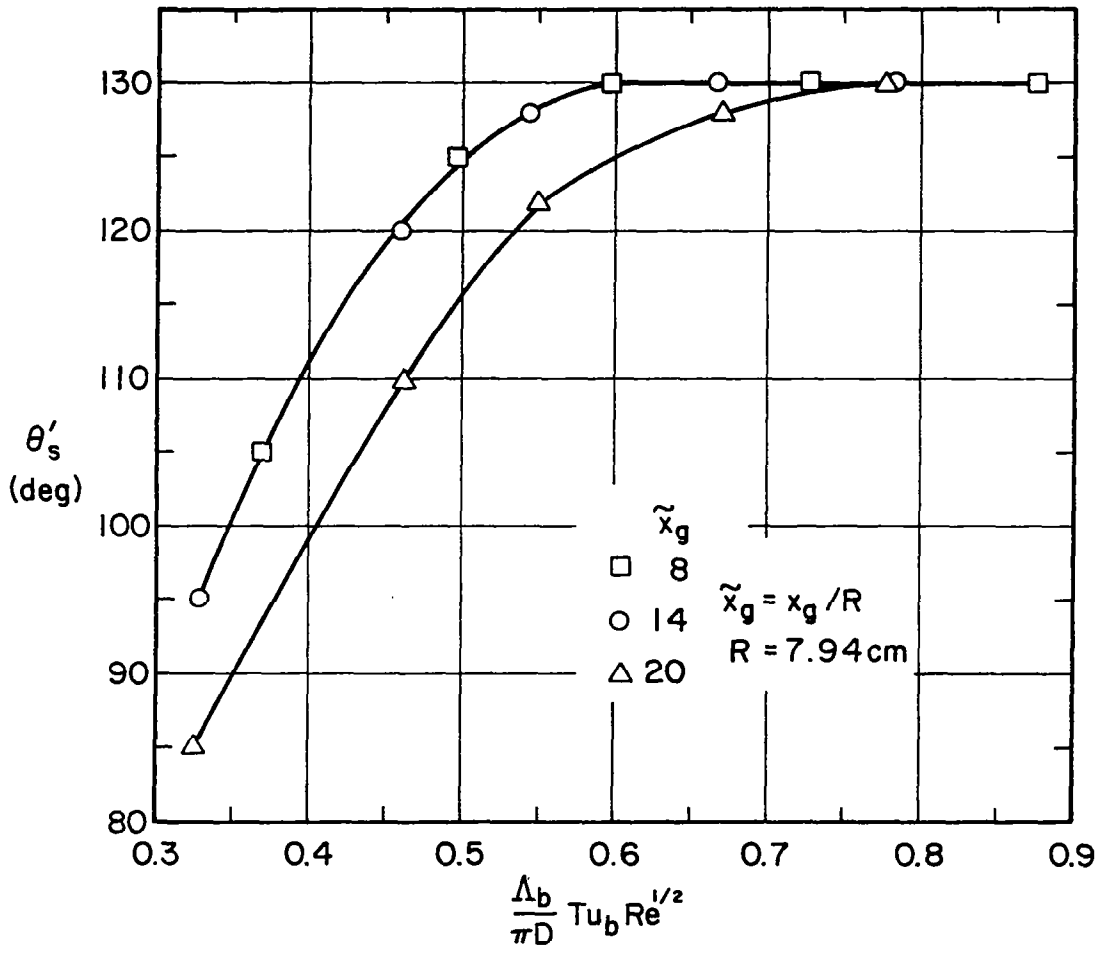

Fig. 6.29 Variation of separation angle with increasing turbulent separation parameter.

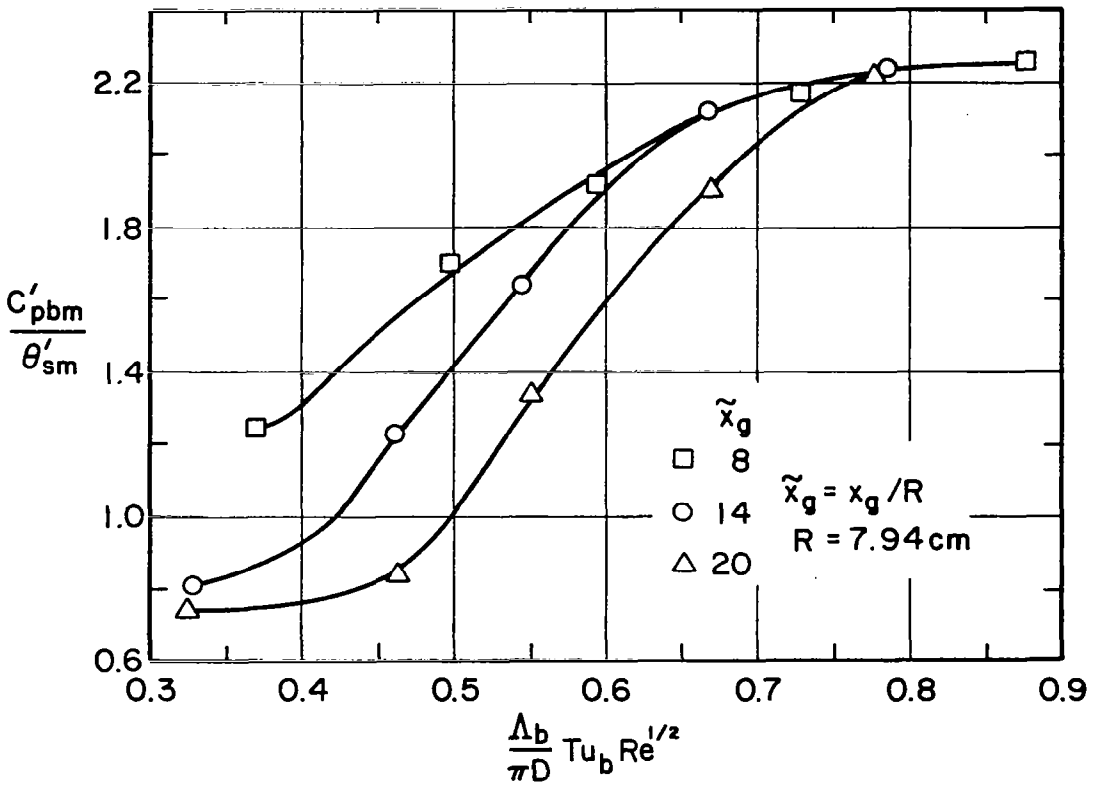

Fig. 6.30 Variation of average adverse pressure gradient as function of turbulent separation parameter.

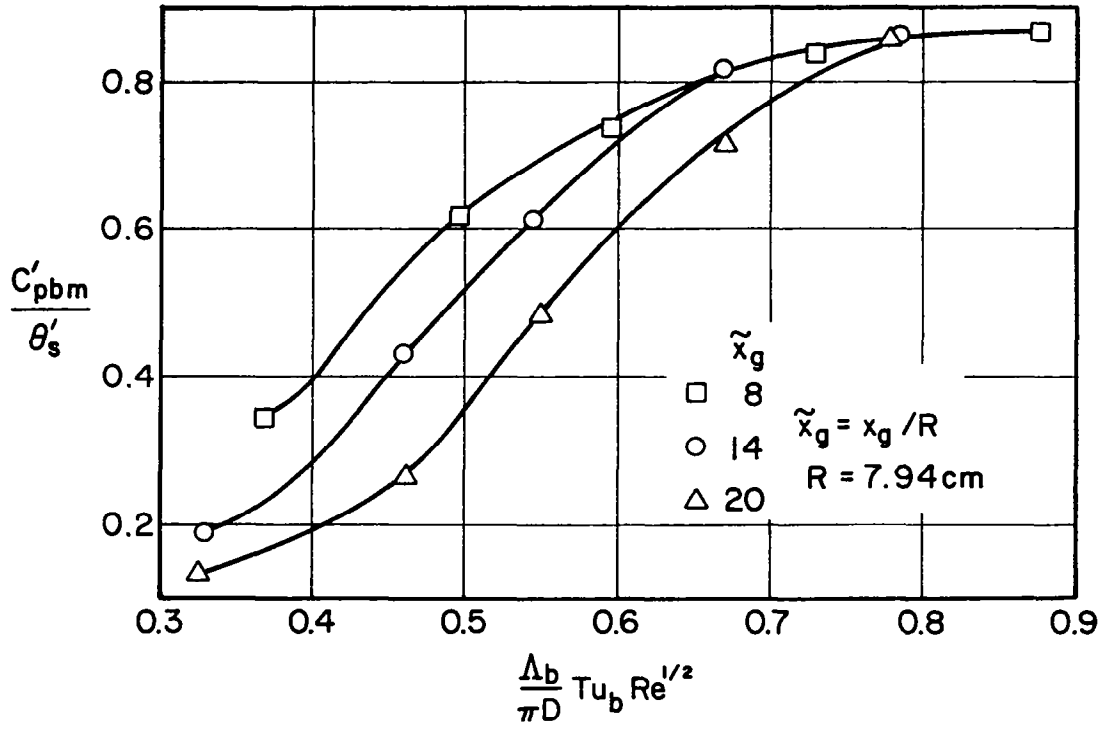

Fig. 6.31 Variation of separation coefficient as function of turbulent separation parameter.

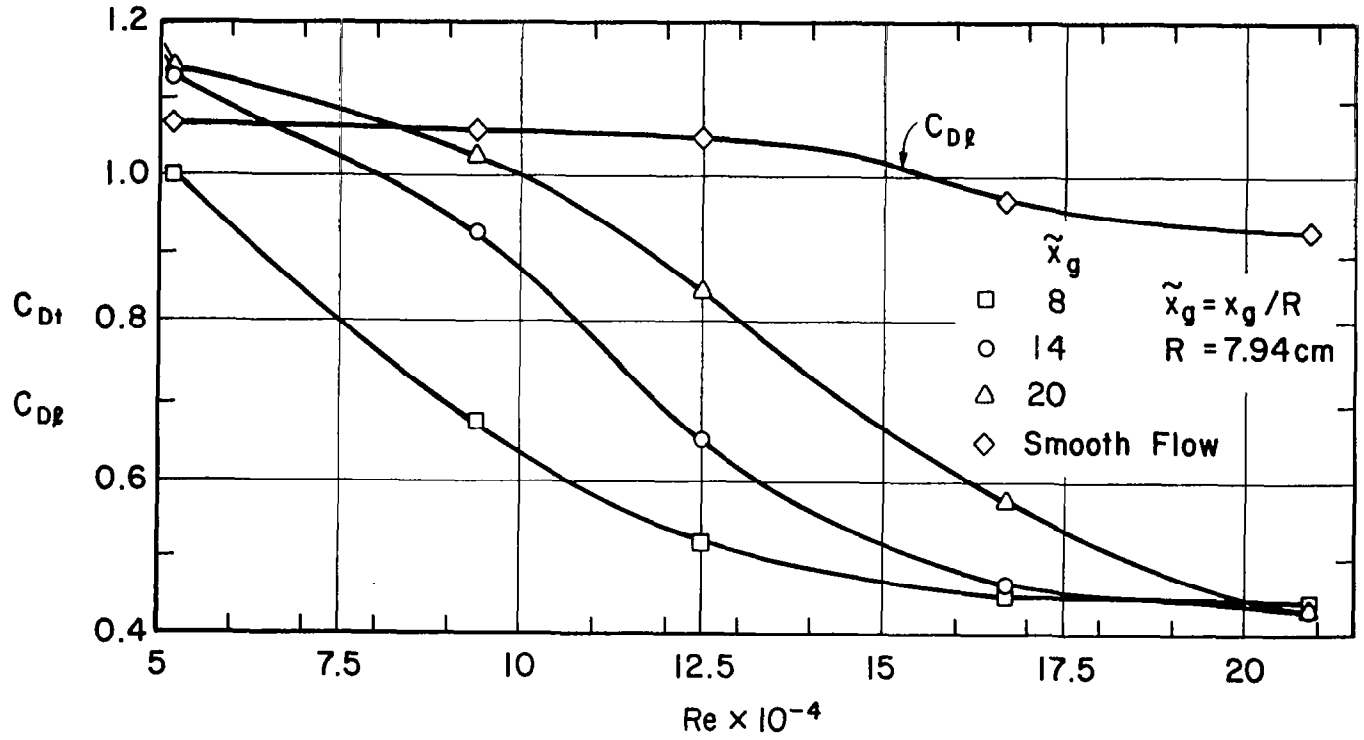

Fig. 6.32 Mean turbulent drag coefficient and laminar drag coefficient as function of subcritical Reynolds number.

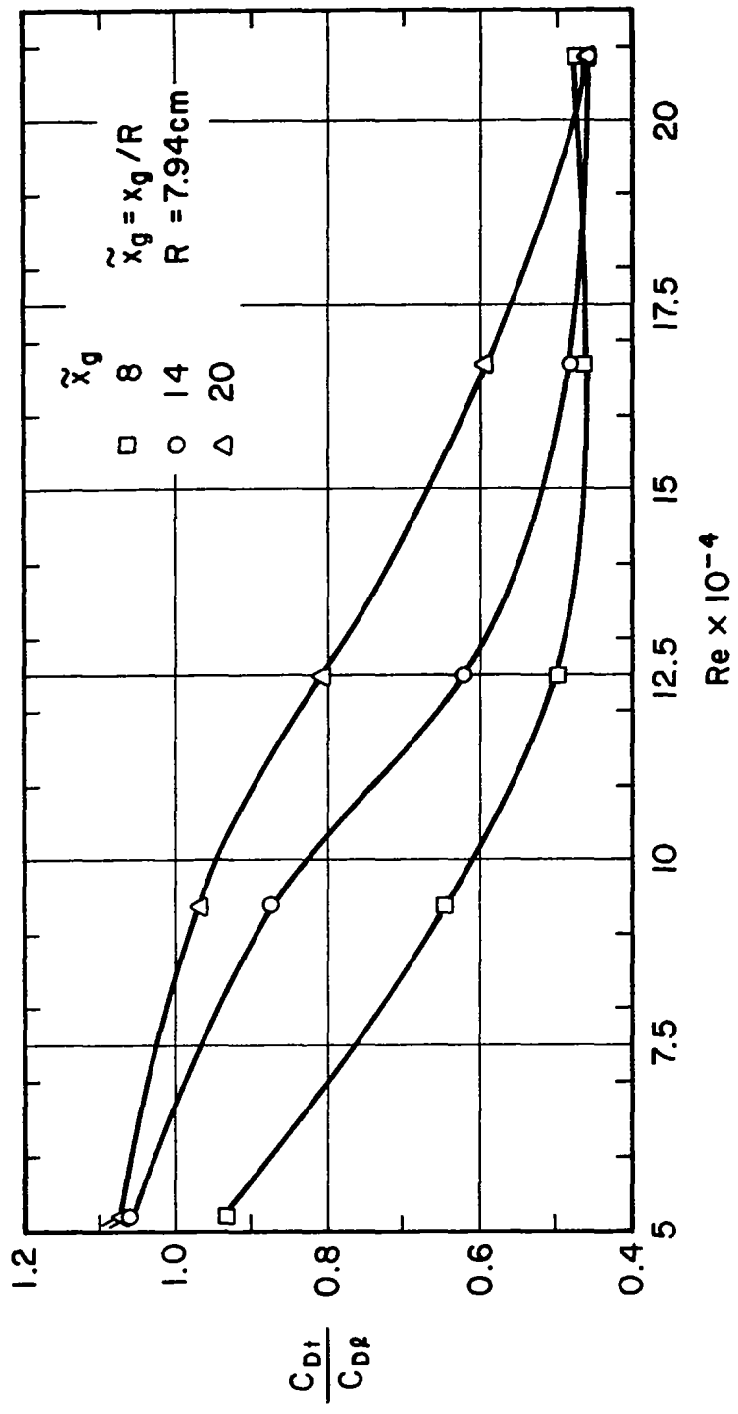

Fig. 6.33 Ratio of mean turbulent drag coefficient to laminar drag coefficient as function of Reynolds number.

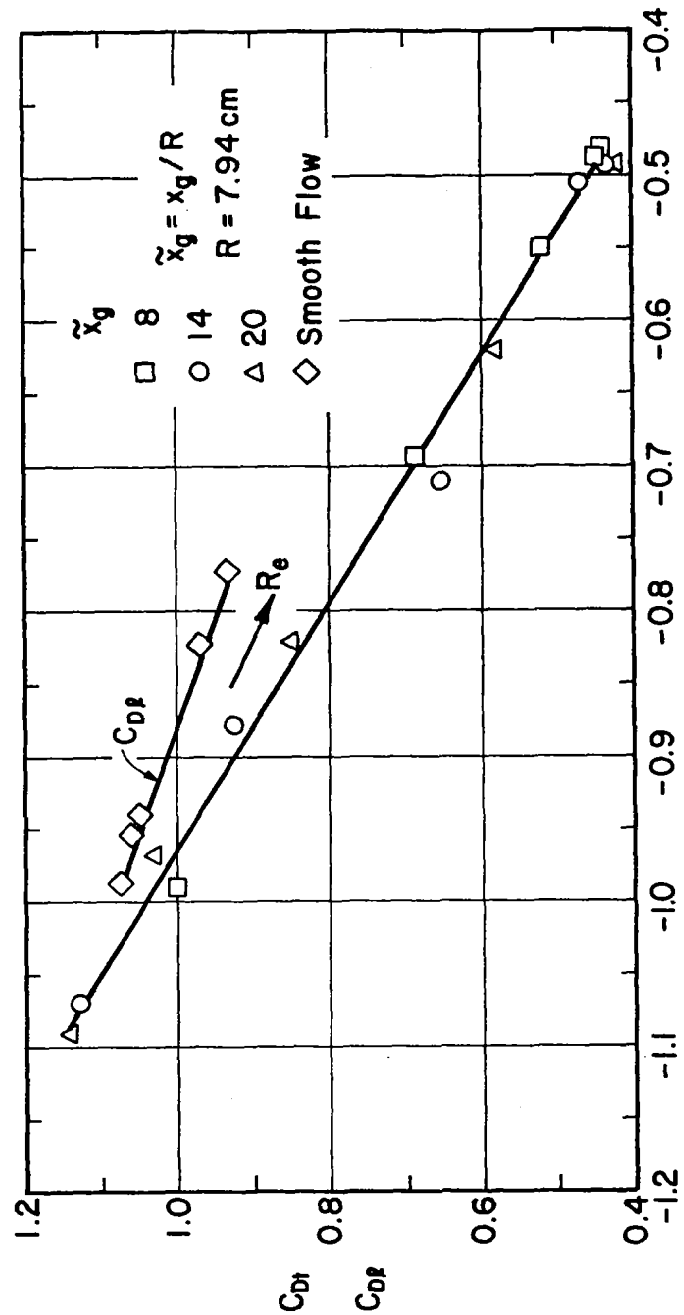

Fig. 6.34 Mean turbulent drag coefficient and laminar drag coefficient as function of base pressure coefficient.

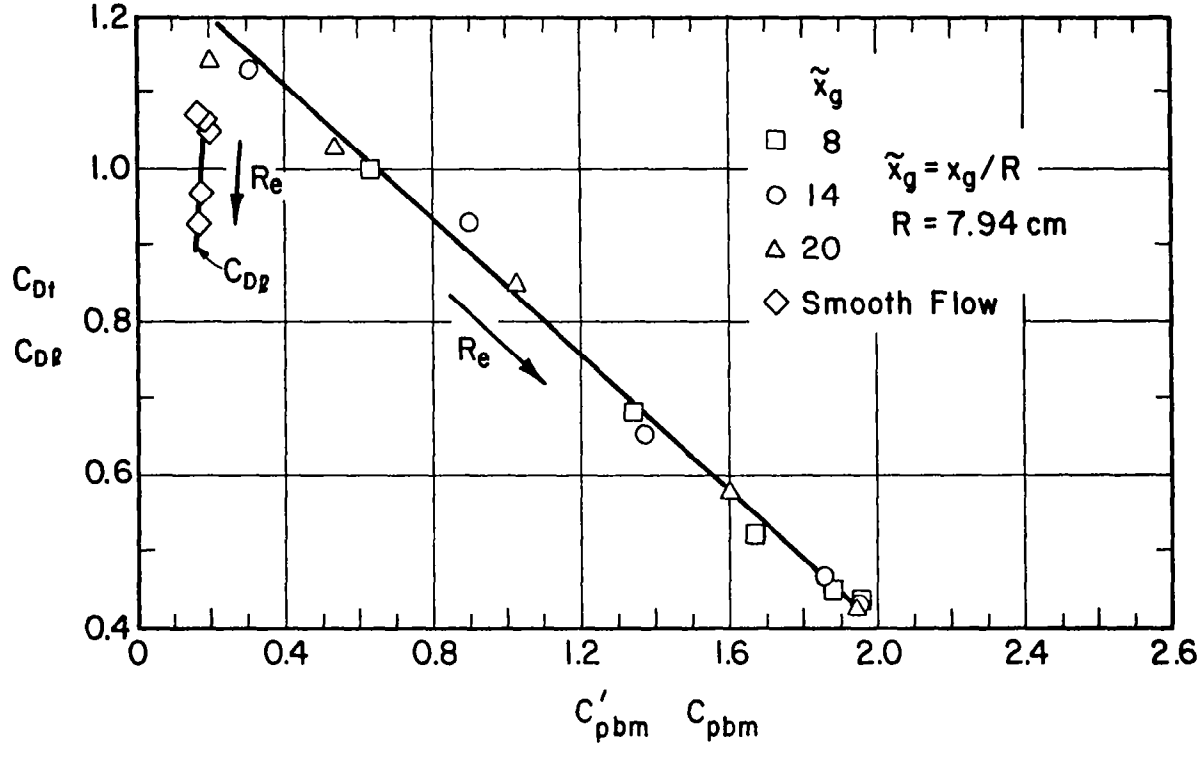

Fig. 6.35 Mean turbulent drag coefficient and laminar drag coefficient as function of pressure rise coefficient.

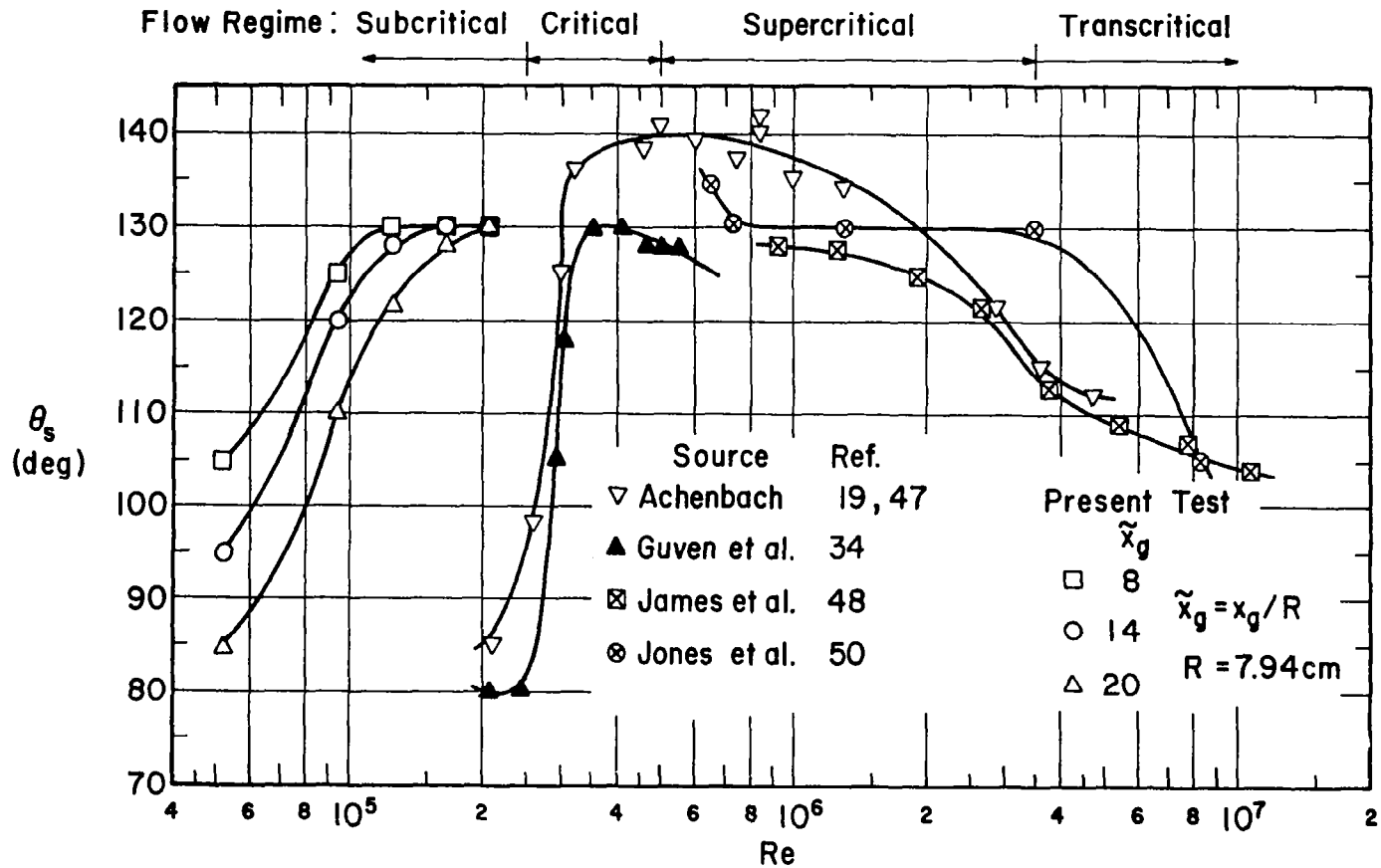

Fig. 6.36 Separation angle as function of Reynolds number.

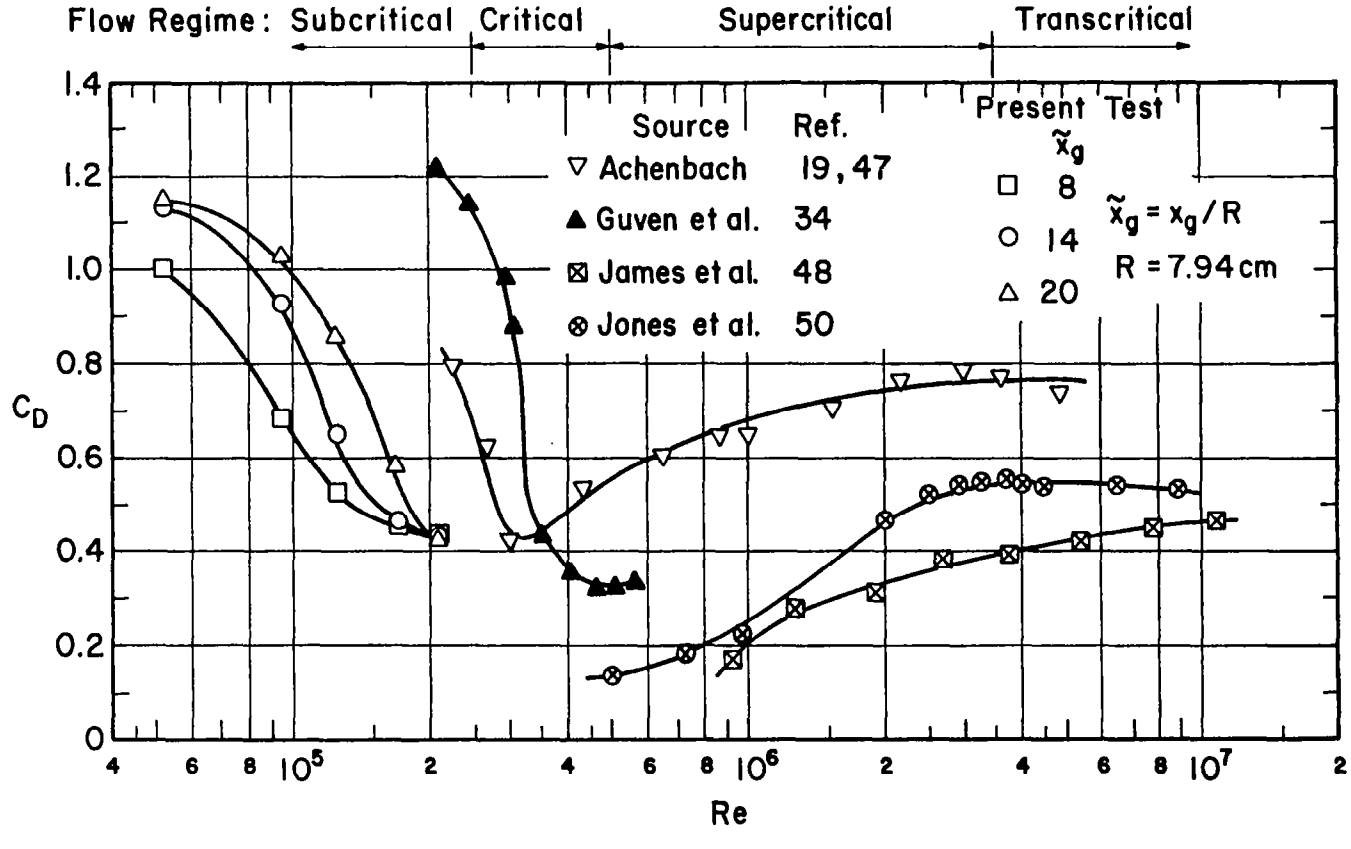

Fig. 6.37 Drag coefficient as function of Reynolds number.

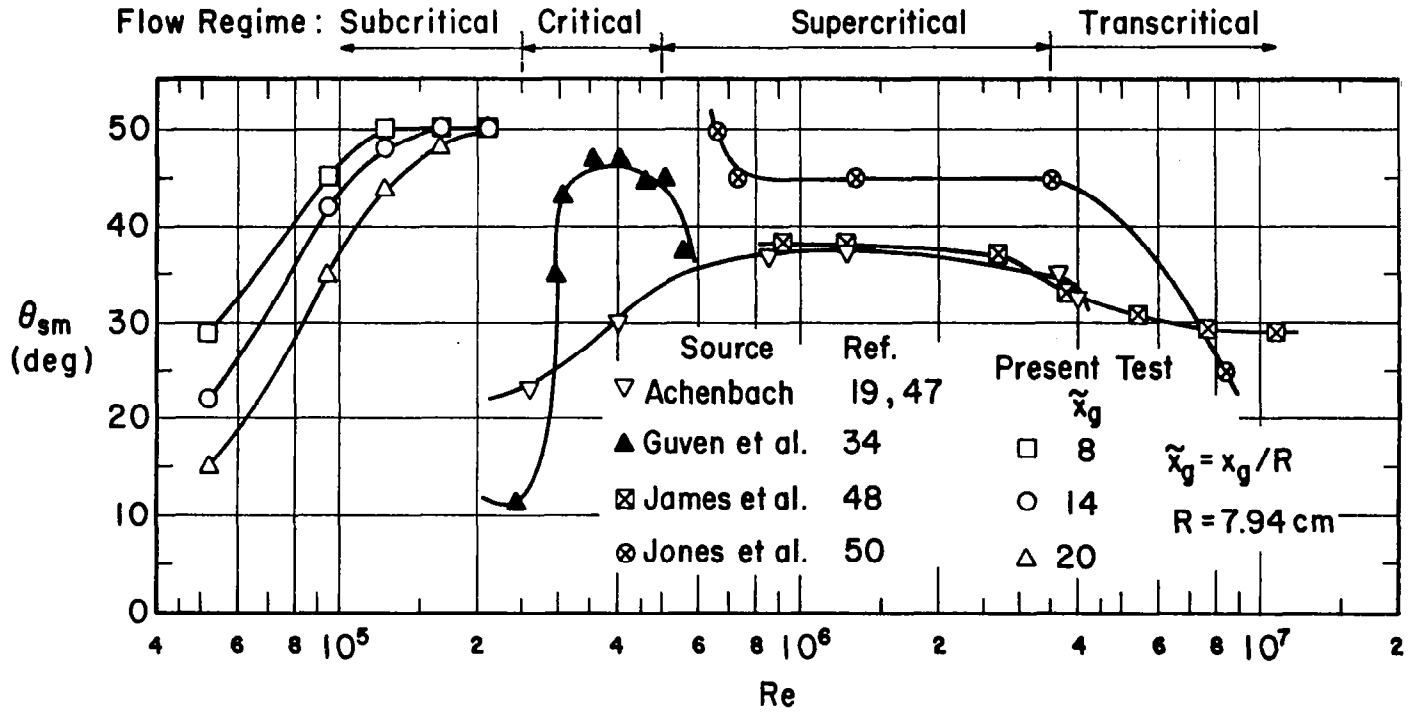

Fig. 6.38 Angular extent of adverse pressure gradient region as function of Reynolds number.

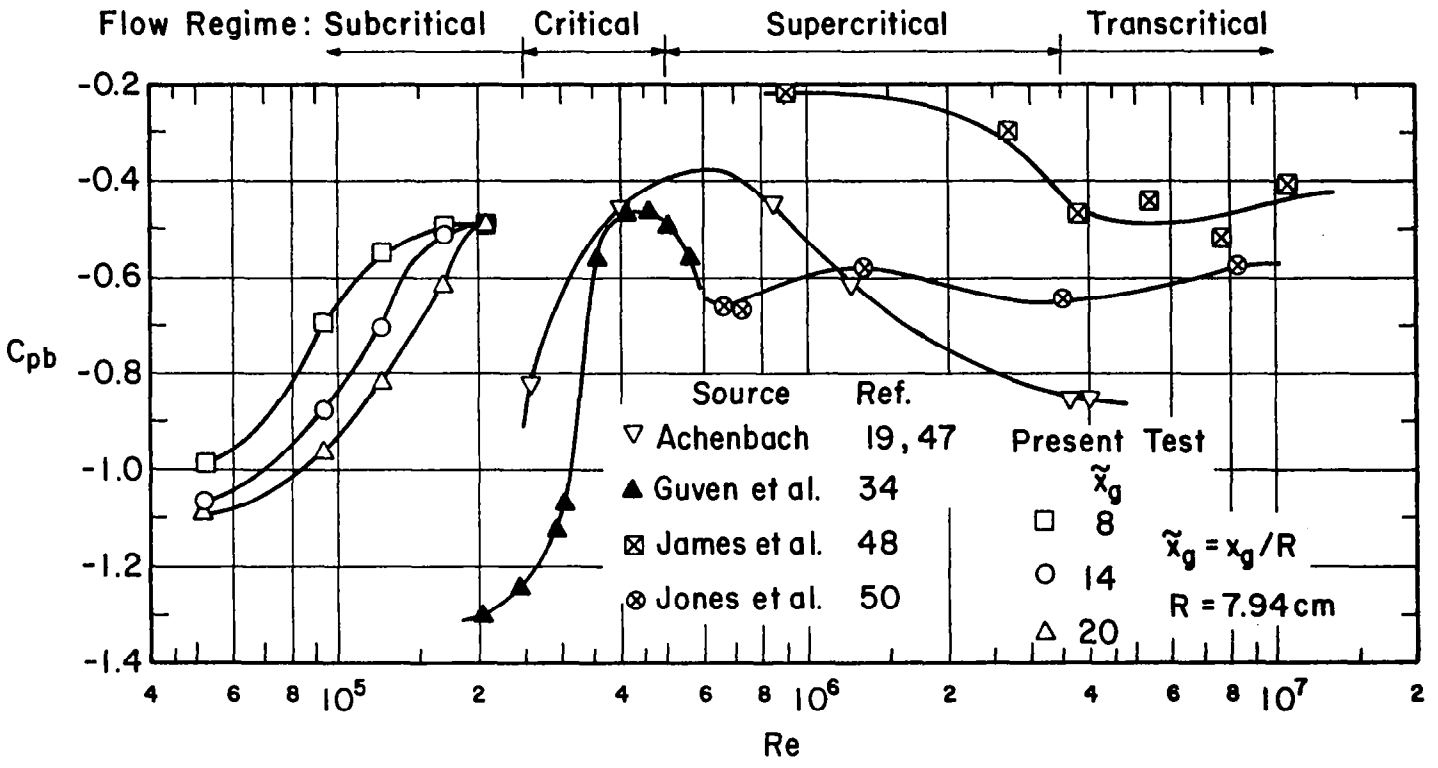

Fig. 6.39 Base pressure coefficient as function of Reynolds number.

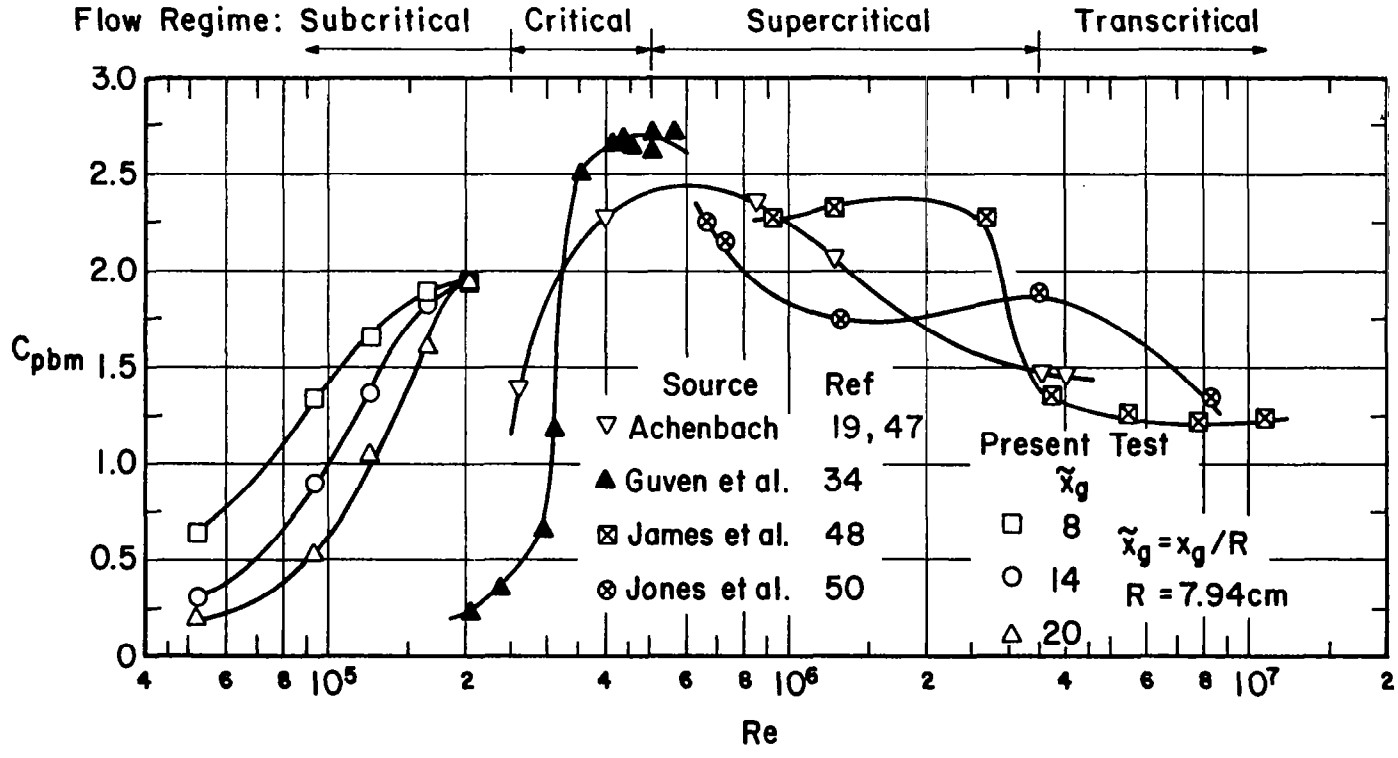

Fig. 6.40 Pressure rise coefficient as function of Reynolds number.

APPENDIX I

SURFACE PRESSURE COEFFICIENT IN TURBULENT INCIDENT FLOW

Generally, the surface pressure coefficient C_p is given by Eq. (3.1) which is rewritten below for convenience. Thus,

$$C_p = (p(\theta) - p_\infty)/\tfrac{1}{2}\rho U_\infty^2 , \qquad (A.I.1)$$

in which $p(\theta)$ is measured surface (or wall) static pressure at any azimuthal angle θ, p_∞ and U_∞ are the freestream static pressure and uniform velocity, respectively, and ρ stands for the density of air in consistent units. This equation can be expressed in terms of the freestream stagnation pressure p_o by

$$C_p = (p(\theta) - p_o)/\tfrac{1}{2}\rho U_\infty^2 + 1 , \qquad (A.I.2)$$

using Bernoulli equation. The freestream conditions were measured in this experiment in the uniform flow upwind of the turbulence-generating grid in order to prevent any turbulence effects upon the reading of the reference Pitot-static tube. As a result, the foregoing equation cannot be applied in the case of a turbulent incident flow without accounting for the losses in the stagnation pressure induced by the grid.

In a turbulent incident flow, the surface mean pressure coefficient C_p' is given in terms of the freestream stagnation pressure p_o' and velocity U_∞' downstream of the grid by

$$C_p' = (p(\theta) - p_o')/\tfrac{1}{2}\rho U_\infty'^2 + 1 . \qquad (A.I.3)$$

The surface pressure $p(\theta)$ according to Eq. (A.I.2) is

$$p(\theta) = \tfrac{1}{2}\rho U_\infty^2 (C_p - 1) + p_o , \qquad (A.I.4)$$

while based on Eq. (A.I.3) is

$$p(\theta) = \tfrac{1}{2}\rho U_\infty'^2 (C_p' - 1) + p_o' . \qquad (A.I.5)$$

Since the surface pressure $p(\theta)$ is independent of where the freestream conditions are monitored, one can equate the foregoing two equations and, therefore,

$$C_p' - 1 = (U_\infty/U_\infty')^2(C_p - 1) + (p_o - p_o')/\tfrac{1}{2}\rho U_\infty'^2 \ . \qquad \text{(A.I.6)}$$

The freestream velocity far downstream of the grid is equal to that upwind of it by continuity condition since the wind-tunnel cross section is the same, i.e., $U_\infty' = U_\infty$. Then the loss in the stagnation pressure $(p_o - p_o')$ is equal to the difference in the static pressure across the grid $(p_\infty - p_\infty')$ according to Bernoulli equation, viz., $p_o - p_o' = p_\infty - p_\infty'$, where p_∞' is the freestream static pressure downwind of the grid. Consequently, Eq. (A.I.6) reduces to

$$C_p' = C_p + \Delta p_\infty/\tfrac{1}{2}\rho U_\infty^2 \ , \qquad \text{(A.I.7)}$$

where C_p is given by Eq. (A.I.1) and $\Delta p_\infty = p_\infty - p_\infty'$. This equation is exactly Eq. (3.2) in Sect. 3.3.

APPENDIX II

BLOCKAGE CORRECTION

The blockage correction for the freestream velocity U_∞ and the drag coefficient C_D introduced by Allen & Vincenti (ref. 20, Eq. (94), p. 177) for the flow of an incompressible fluid are:

$$U_\infty^*/U_\infty = 1 + \tau C_D + \Lambda\sigma \ , \qquad \text{(A.II.1)}$$

and

$$C_D^*/C_D = 1 - 2\tau C_D - 3\Lambda\sigma \ , \qquad \text{(A.II.2)}$$

where the asterisk denotes corrected values. In the foregoing two equations, Λ designates the body shape factor, and σ and τ are two blockage parameters given by

$$\sigma = (\pi^2/48)(D/h)^2 \ , \qquad \text{(A.II.3)}$$

and

$$\tau = \tfrac{1}{4}(D/h) \ , \qquad \text{(A.II.4)}$$

in which D/h is the blockage coefficient, where D denotes the cylinder diameter and h is the height (or width) of the wind-tunnel cross section. The body shape factor Λ for a circular cylinder is equal to 4 according to the values given in Ref. 20 (Table I, p. 183). Substitution of the values of Λ, σ and τ in Eqs. (A.II.1) and (A.II.2) leads to the following correction relationships:

$$U_\infty^*/U_\infty = 1 + 0.25C_D\,(D/h) + 0.82(D/h)^2 \ , \qquad \text{(A.II.5)}$$

and

$$C_D^*/C_D = 1 - 0.50C_D(D/h) - 2.467(D/h)^2 \ . \qquad \text{(A.II.6)}$$

These are exactly Eqs. (3.4) and (3.5) given in Sect. 3.4. The correction for the Reynolds number is identical to that for the freestream velocity since $R\mathring{e}/Re = U_\infty^*/U_\infty$ for a given cylinder.

In addition to correcting the freestream velocity, the Reynolds number and the drag coefficient, it is necessary to correct the pressure coefficient. The measured (uncorrected)

pressure coefficient C_p is given by Eq. (3.1) or in terms of the stagnation pressure by Eq. (A.I.2) which is written below in the form

$$C_p - 1 = (p(\theta) - p_o)/\tfrac{1}{2}\rho U_\infty^2 \ . \qquad \text{(A.II.7)}$$

In the case of unrestricted flow, the pressure coefficient is given by exactly the same equation as the foregoing one provided that the corrected values for the surface pressure $p^*(\theta)$, the stagnation pressure p_o^* and the freestream velocity U_∞^* are used. Thus, the pressure coefficient for unconfined flow is

$$C_p^* - 1 = (p^*(\theta) - p_o^*)/\tfrac{1}{2}\rho U_\infty^{*2} \ . \qquad \text{(A.II.8)}$$

Under the condition that the difference between the wall pressure and the stagnation pressure is the same in both unconfined and confined flow-i.e., $(p^*(\theta)-p_o^*)=(p(\theta)-p_o)$-one can obtain a relationship for the corrected pressure coefficient by means of Eqs. (A.II.7) and (A.II.8). This equation is

$$(C_p^* - 1)/(C_p - 1) = (U_\infty^*/U_\infty)^{-2} \ . \qquad \text{(A.II.9)}$$

As a result, the corrected pressure coefficient depends solely on the corrected freestream velocity. The foregoing equation is Eq. (3.6) in Sect. (3.4).

APPENDIX III

FLOW PARAMETERS DATA

This experiment was conducted at five different cylinder-diameter subcritical Reynolds numbers Re ranging from 5.2×10^4 to 2.09×10^5 (based on freestream velocity U_∞ and cylinder diameter D; air at 20°C (68°F) kinematic viscosity $\nu = 1.48 \times 10^{-5}$ m^2/s (1.59×10^{-4} ft^2/s)). The corresponding uniform freestream velocity U_∞, for the particular cylinder of diameter D = 15.88 cm used here, varied from 4.9 to 19.5 m/s. All the five Reynolds numbers and corresponding freestream velocities are tabulated in Table A.III.1 below. Corrected values of the uniform freestream velocities U_∞ were computed using the Allen-Vincenti method according to Eq. (3.4) (see Sect. 3.4 & App. II) when the blockage coefficient of the cylinder D/h = 0.087 (see Sect. 2.2). In computing the corrected freestream velocity, the measured drag coefficient in smooth (or laminar) incident flow $C_{D\ell}$ was employed. The corrected uniform freestream velocities U_∞^*, along with their corresponding corrected Reynolds numbers $R\overset{*}{e}$, are summarized in Table A.III.1. All the Reynolds numbers in this table are rounded to two or three significant digits.

The thickness of the laminar boundary layer at stagnation point δ_ℓ and the neutral scale of the stagnation flow λ_o (vid., Eqs. (2.1) & (2.2)), based on the measured (uncorrected) Reynolds number, are listed in Table A.III.2 below. Their dimensionless values defined in terms of the cylinder radius R (7.94 cm (3-1/8 in))-viz., $\tilde{\delta}_\ell = \delta_\ell/R$ and $\tilde{\lambda}_o = \lambda_o/R$-are also tabulated in this table.

The corrected values of the uniform freestream velocity and Reynolds number according to the Maskell method (M), $U_{\infty M}^*$ and $R\overset{*}{e}_M$, are given in Table A.III.3 below. They were computed using Eq. (3.7) when the corrected base pressure parameter k^{*2} was obtained at each Reynolds number by means of Eq. (3.8) within five iterations at the most (see Sect. 3.4). The measured base pressure coefficient C_{pb} and base pressure parameter $k^2 = 1 - C_{pb}$ are listed in this table for convenience's sake. In addition, the ratio of the corrected uniform freestream velocities computed by the Maskell and Allen-Vincenti methods-viz., $U_{\infty M}^*/U_\infty^*$-is also tabulated in Table A.III.3 for illustration's sake.

TABLE A.III.1. FLOW PARAMETERS MEASURED AND CORRECTED BY ALLEN-VINCENTI METHOD

Re ($\times 10^{-4}$)	U_∞ (m/s)	U_∞ (ft/s)	$C_{D\ell}$	U^*_∞/U_∞	U^*_∞ (m/s)	U^*_∞ (ft/s)	Re^* ($\times 10^{-4}$)
5.2	4.9	16.0	1.07	1.029	5.0	16.5	5.4
9.4	8.8	28.8	1.06	1.029	9.0	29.6	9.7
12.5	11.7	38.4	1.05	1.029	12.0	39.5	12.9
16.7	15.6	51.2	0.97	1.027	16.0	52.6	17.2
20.9	19.5	64.0	0.93	1.026	20.0	65.7	21.4

TABLE A.III.2. BOUNDARY-LAYER THICKNESS AND NEUTRAL SCALE

Re ($\times 10^{-4}$)	δ_ℓ (mm)	δ_ℓ (mils)	$\tilde{\delta}_\ell$	λ_o (mm)	λ_o (mils)	$\tilde{\lambda}_o$
5.2	0.836	33	0.0105	2.19	86	0.028
9.4	0.622	24	0.0078	1.63	64	0.020
12.5	0.539	21	0.0068	1.41	55	0.018
16.7	0.466	18	0.0059	1.22	48	0.015
20.9	0.417	16	0.0052	1.09	43	0.014

TABLE A.III.3. FLOW PARAMETERS MEASURED AND CORRECTED BY MASKELL METHOD

Re ($\times 10^{-4}$)	U_∞ (m/s)	$C_{D\ell}$	C_{pb}	k^2	k^{*2}	k/k^*	$U^*_{\infty M}$ (m/s)	Re^*_M ($\times 10^{-4}$)	$U^*_{\infty M}/U^*_\infty$
5.2	4.9	1.07	-0.986	1.986	1.775	1.058	5.2	5.5	1.040
9.4	8.8	1.06	-0.954	1.954	1.740	1.060	9.3	10.0	1.033
12.5	11.7	1.05	-0.939	1.939	1.724	1.061	12.4	13.3	1.033
16.7	15.6	0.97	-0.824	1.824	1.600	1.068	16.7	17.8	1.044
20.9	19.5	0.93	-0.774	1.774	1.547	1.071	20.9	22.4	1.045

APPENDIX IV

SURFACE PRESSURE DISTRIBUTION IN SMOOTH INCIDENT FLOW

The surface pressure coefficients C_p (vid., Eq. (3.1)) measured in smooth incident flow at 18 stations over half of the cylinder circumference-i.e., from $\theta = 0$ to 180°-are listed in Table A.IV.1 below at each of the five subcritical Reynolds numbers. Both the measured and corrected Reynolds numbers (Re and $\mathring{R}e$) are given in this table. The corrected pressure coefficient C_p^* according to the Allen-Vincenti method (vid., Eq. (3.6) and App. II), along with those corrected by means of Maskell scheme C_{pM}^* (vid., Eq. (3.7)), are tabulated in this table. Note that the distributions of the corrected pressure coefficient by Allen-Vincenti method are shown in Figs. 5.1 to 5.4. In order to indicate the degree to which the Allen-Vincenti and Maskell blockage correction methods affect the values of the pressure coefficient and to underscore the differences in the estimates obtained by means of those two correction schemes, the following ratios are given in this table: (1) the pressure coefficient corrected by Allen-Vincenti method to its measured counterpart C_p^*/C_p; (2) the pressure coefficient corrected by Maskell scheme to its corresponding measured value C_{pM}^*/C_p; and (3) the pressure coefficient corrected by Maskell scheme to its counterpart corrected by Allen-Vincenti method C_{pM}^*/C_p^*.

TABLE A.IV.1. SMOOTH INCIDENT FLOW

SURFACE PRESSURE COEFFICIENT DISTRIBUTION

$Rex10^{-4}$				5.2						9.4			
$R\overset{*}{e}x10^{-4}$				5.4						9.7			
θ (deg)	C_p	C_p^*	C_p^*/C_p	C_{pM}^*	C_{pM}^*/C_p	C_{pM}^*/C_p^*	C_p	C_p^*	C_p^*/C_p	C_{pM}^*	C_{pM}^*/C_p	C_{pM}^*/C_p^*
0	1.000	1.000	1.000	1.000	1.000	1.000	1.000	1.000	1.000	1.000	1.000	1.000
5	0.990	0.991	1.001	0.991	1.001	1.000	0.992	0.992	1.000	0.993	1.001	1.001
10	0.929	0.933	1.004	0.936	1.007	1.003	0.947	0.950	1.003	0.953	1.006	1.003
15	0.828	0.838	1.012	0.846	1.022	1.010	0.836	0.845	1.011	0.854	1.022	1.011
20	0.662	0.681	1.029	0.698	1.054	1.025	0.691	0.708	1.025	0.725	1.049	1.024
25	0.486	0.515	1.060	0.541	1.113	1.050	0.496	0.524	1.056	0.551	1.111	1.052
30	0.266	0.307	1.154	0.344	1.293	1.121	0.279	0.319	1.143	0.358	1.283	1.122
40	-0.253	-0.183	0.723	-0.120	0.474	0.656	-0.266	-0.195	0.737	-0.127	0.477	0.651
50	-0.672	-0.578	0.862	-0.494	0.735	0.853	-0.706	-0.611	0.865	-0.519	0.735	0.849
60	-1.060	-0.944	0.892	-0.841	0.793	0.890	-1.040	-0.926	0.893	-0.818	0.787	0.883
70	-1.150	-1.030	0.896	-0.922	0.802	0.895	-1.140	-1.020	0.895	-0.905	0.794	0.887
80	-0.949	-0.840	0.885	-0.742	0.782	0.883	-0.920	-0.813	0.884	-0.709	0.771	0.872
90	-0.953	-0.844	0.886	-0.745	0.782	0.883	-0.939	-0.831	0.885	-0.726	0.773	0.874
100	-0.953	-0.844	0.886	-0.745	0.782	0.883	-0.939	-0.831	0.885	-0.726	0.773	0.874
120	-0.949	-0.840	0.885	-0.742	0.782	0.883	-0.954	-0.845	0.887	-0.740	0.776	0.876
140	-0.959	-0.849	0.885	-0.751	0.783	0.885	-0.954	-0.845	0.887	-0.740	0.776	0.876
160	-0.986	-0.874	0.887	-0.775	0.786	0.887	-0.962	-0.853	0.887	-0.747	0.777	0.876
180	-0.986	-0.874	0.887	-0.775	0.786	0.887	-0.954	-0.846	0.887	-0.740	0.776	0.876

$Rex10^{-4}$				12.5						16.7			
$R\overset{*}{e}x10^{-4}$				12.9						17.2			
θ (deg)	C_p	C_p^*	C_p^*/C_p	C_{pM}^*	C_{pM}^*/C_p	C_{pM}^*/C_p^*	C_p	C_p^*	C_p^*/C_p	C_{pM}^*	C_{pM}^*/C_p	C_{pM}^*/C_p^*
0	1.000	1.000	1.000	1.000	1.000	1.000	1.000	1.000	1.000	1.000	1.000	1.000
5	0.994	0.994	1.000	0.995	1.001	1.001	0.990	0.991	1.001	0.991	1.001	1.000
10	0.951	0.954	1.003	0.956	1.005	1.002	0.932	0.936	1.004	0.940	1.009	1.004
15	0.848	0.856	1.009	0.865	1.020	1.011	0.834	0.843	1.011	0.854	1.024	1.013
20	0.695	0.712	1.024	0.729	1.049	1.024	0.687	0.703	1.023	0.725	1.055	1.031
25	0.509	0.536	1.053	0.563	1.106	1.050	0.502	0.528	1.052	0.563	1.122	1.066
30	0.288	0.327	1.135	0.367	1.274	1.122	0.283	0.321	1.131	0.371	1.311	1.156
40	-0.271	-0.201	0.742	-0.130	0.480	0.647	-0.237	-0.172	0.726	-0.085	0.359	0.494
50	-0.689	-0.595	0.865	-0.502	0.729	0.844	-0.632	-0.546	0.866	-0.431	0.682	0.789
60	-1.070	-0.955	0.893	-0.841	0.786	0.881	-0.967	-0.864	0.893	-0.725	0.750	0.839
70	-1.130	-1.010	0.894	-0.894	0.791	0.885	-1.000	-0.895	0.896	-0.754	0.754	0.842
80	-0.945	-0.837	0.887	-0.729	0.771	0.871	-0.866	-0.768	0.888	-0.637	0.736	0.829
90	-0.933	-0.826	0.885	-0.719	0.771	0.870	-0.840	-0.744	0.886	-0.614	0.731	0.829
100	-0.939	-0.831	0.886	-0.724	0.771	0.871	-0.863	-0.765	0.888	-0.634	0.735	0.829
120	-0.945	-0.837	0.887	-0.729	0.771	0.871	-0.857	-0.760	0.887	-0.629	0.734	0.828
140	-0.951	-0.843	0.886	-0.735	0.773	0.872	-0.840	-0.744	0.886	-0.614	0.731	0.825
160	-0.939	-0.831	0.886	-0.724	0.771	0.871	-0.840	-0.744	0.886	-0.614	0.731	0.825
180	-0.939	-0.831	0.886	-0.724	0.771	0.871	-0.824	-0.728	0.885	-0.600	0.728	0.824

$Rex10^{-4}$				20.9		
$R\overset{*}{e}x10^{-4}$				21.4		
θ (deg)	C_p	C_p^*	C_p^*/C_p	C_{pM}^*	C_{pM}^*/C_p	C_{pM}^*/C_p^*
0	1.000	1.000	1.000	1.000	1.000	1.000
5	0.976	0.977	1.001	0.979	1.003	1.002
10	0.929	0.933	1.004	0.938	1.010	1.005
15	0.823	0.832	1.011	0.846	1.028	1.017
20	0.675	0.691	1.024	0.717	1.062	1.038
25	0.509	0.534	1.049	0.572	1.124	1.071
30	0.293	0.329	1.123	0.383	1.307	1.164
40	-0.220	-0.158	0.718	-0.064	0.291	0.405
50	-0.590	-0.510	0.864	-0.387	0.656	0.759
60	-0.906	-0.810	0.894	-0.662	0.731	0.817
70	-0.940	-0.842	0.896	-0.692	0.736	0.822
80	-0.808	-0.716	0.887	-0.577	0.714	0.806
90	-0.814	-0.722	0.887	-0.582	0.715	0.806
100	-0.810	-0.718	0.888	-0.579	0.715	0.806
120	-0.791	-0.700	0.886	-0.562	0.710	0.803
140	-0.769	-0.680	0.884	-0.543	0.706	0.799
160	-0.784	-0.694	0.885	-0.556	0.709	0.801
180	-0.774	-0.684	0.884	-0.547	0.707	0.800

APPENDIX V

DRAG COEFFICIENT IN SMOOTH INCIDENT FLOW

The cylinder drag coefficient $C_{D\ell}$ in smooth (or laminar) incident flow was computed at each of the five sub-critical Reynolds numbers by integrating the corresponding measured pressure distribution according to Eq. (3.3). All the five measured Reynolds numbers Re and corresponding drag coefficients $C_{D\ell}$ are listed in Table A.V.I below. The blockage-corrected values of the Reynolds number $R\overset{*}{e}$ and drag coefficient $C^*_{D\ell}$ obtained by the Allen-Vincenti method (vid., Eqs. (3.4) & (3.5)) are also tabulated in this table. In addition, the drag coefficients corrected for blockage according to the Maskell scheme $C^*_{D\ell M}$ (vid., Eq. (3.7)) are summarized in Table A.V.1 below for comparison's sake. In order to demonstrate the extent to which each blockage correction method affects the value of the drag coefficient and to facilitate comparison of the two correction techniques, the following ratios are given in Table A.V.1: (1) the drag coefficient corrected by Allen-Vincenti method to its measured counterpart $C^*_{D\ell}/C_{D\ell}$; (2) the drag coefficient corrected by Maskell scheme to its corresponding measured value $C^*_{D\ell M}/C_{D\ell}$; and, (3) the drag coefficient corrected by Maskell scheme to its counterpart corrected by Allen-Vincenti method $C^*_{D\ell M}/C^*_{D\ell}$.

TABLE A.V.1. SMOOTH INCIDENT FLOW

DRAG COEFFICIENT

Re ($\times 10^{-4}$)	$C_{D\ell}$	$R\overset{*}{e}$ ($\times 10^{-4}$)	$C^*_{D\ell}$	$C^*_{D\ell}/C_{D\ell}$	$C^*_{D\ell M}$	$C^*_{D\ell M}/C_{D\ell}$	$C^*_{D\ell M}/C^*_{D\ell}$
5.2	1.07	5.4	1.00	0.935	0.95	0.888	0.950
9.4	1.06	9.7	0.99	0.934	0.93	0.877	0.939
12.5	1.05	12.9	0.98	0.933	0.92	0.876	0.939
16.7	0.97	17.2	0.91	0.938	0.85	0.876	0.934
20.9	0.93	21.4	0.87	0.935	0.81	0.871	0.931

APPENDIX VI

TURBULENCE DATA AND SURFACE PRESSURE DISTRIBUTION IN TURBULENT INCIDENT FLOW

The mean surface pressure coefficients C_p' measured in turbulent incident flow at 23 stations over half of the cylinder circumference, along with its ratio to the measured (uncorrected) pressure coefficient C_p at the same azimuthal angle θ in smooth incident flow C_p'/C_p, are listed in Table A.VI.1 below at each of the five subcritical Reynolds numbers Re and each grid position $\tilde{x}_g$. In addition, the following data at each Reynolds number is tabulated in this table:

(1) the grid position $\tilde{x}_g$ ($x_g = \tilde{x}_g/R$, R = 7.94 cm);

(2) the background turbulence intensity Tu_b at each test position (vid., Fig. 6.1);

(3) the background turbulence longitudinal integral scale referred to the cylinder diameter Λ_b/D at each test position (D = 15.88 cm, vid., Fig. 6.2);

(4) the background turbulence longitudinal integral scale referred to the neutral scale of the stagnation flow Λ_b/λ_o at each test position (vid., Fig. 6.3);

(5) the critical turbulence intensity Tu_c (vid., Fig. 6.4);

(6) the position upwind of the cylinder $\tilde{x}_{min}$ ($\tilde{x}_{min} = x_{min}/R$) where the critical turbulence intensity was monitored (vid., Fig. 6.4);

The distributions of the pressure coefficient are shown in Figs. 6.5 to 6.9.

The following data in turbulent incident flow is further compiled at each Reynolds number and grid position in Table A.VI.2 below:

(1) the angular position of minimum pressure coefficient θ_m' (vid., Fig. 6.12);

(2) the separation angle (or the starting point of the base region) θ_s' (vid., Fig. 6.20);

(3) the angular extent of the adverse pressure gradient region θ'_{sm} (vid., Fig. 6.13);

(4) the angular extent of the base region θ'_{bs} (vid., Fig. 6.14);

(5) the minimum pressure coefficient C'_{pm} and its ratio to the minimum pressure coefficient in smooth incident flow C'_{pm}/C_{pm} (vid., Figs. 6.10 & 6.11);

(6) the base pressure coefficient C'_{pb} and its ratio to the base pressure coefficient in smooth incident flow C'_{pb}/C_{pb} (vid., Figs. 6.15 & 6.16);

(7) the pressure rise coefficient across the adverse pressure gradient region C'_{pbm} and its ratio to the pressure rise coefficient in smooth incident flow C'_{pbm}/C_{pbm} (vid., Figs. 6.18 & 6.19).

(8) the average adverse pressure gradient across the adverse pressure gradient region C'_{pbm}/θ'_{sm} (vid., Fig. 6.30);

(9) the separation coefficient C'_{pbm}/θ'_{s} (vid., Fig. 6.31);

(10) the turbulence parameter based on background turbulence intensity at the test position Tu_b^2Re (vid., Figs. 6.25 & 6.26);

(11) the turbulence parameter based on the critical turbulence intensity Tu_c^2Re (vid., Figs. 6.25 & 6.26);

(12) the turbulence separation parameter $(\Lambda_b/\pi D)Tu_bRe^{\frac{1}{2}}$ (vid., Figs. 6.27, 6.28, 6.29, 6.30 & 6.31);

(13) the turbulent drag coefficient C_{Dt} and its ratio to the corresponding measured (uncorrected) laminar drag coefficent $C_{Dt}/C_{D\ell}$ (vid., Figs. 6.32 & 6.33).

Note that data in turbulent incident flow is denoted by a prime. In addition, the angular position of minimum pressure coefficient (θ_m), the separation angle (θ_s), the angular extents of the adverse pressure gradient region and base region (θ_{sm} and θ_{bs}), the measured (uncorrected) minimum, base and pressure rise coefficients (C_{pm}, C_{pb} and C_{pbm}),

and the measured (uncorrected) drag coefficient ($C_{D\ell}$) at each Reynolds number in smooth incident flow are summarized in Table A.VI.3 below for convenience's sake.

TABLE A.VI.1. TURBULENT INCIDENT FLOW

TURBULENCE DATA AND MEAN SURFACE PRESSURE COEFFICIENT DISTRIBUTION

Re(x10^{-4})	5.2						9.4					
$\tilde{x}_g$	8		14		20		8		14		20	
Tu_b (%)	4.1		2.7		2.15		3.7		2.6		2.12	
Λ_b/D	0.124		0.168		0.208		0.138		0.182		0.224	
Λ_b/Λ_o	9.0		12.19		15.10		13.47		17.76		21.86	
Tu_c (%)	7		4.8		3.5		6.9		4.7		3.2	
$\tilde{x}_{min}$	1.6		2.2		2.5		1.6		2.2		2.5	
θ (deg)	C'_p	C'_p/C_p	C'_p	C'_p/C_p	C'_p	C'_p/C_p	C'_p	C'_p/C_p	C'_p	C'_p/C_p	C'_p	C'_p/C_p
0	1.000	1.000	1.000	1.000	1.000	1.000	1.000	1.000	1.000	1.000	1.000	1.000
5	0.998	1.008	0.990	1.000	0.990	1.000	0.998	1.006	0.996	1.004	0.990	0.998
10	0.940	1.012	0.959	1.032	0.951	1.024	0.952	1.005	0.945	0.998	0.938	0.990
15	0.841	1.016	0.857	1.035	0.848	1.024	0.837	1.001	0.845	1.011	0.841	1.006
20	0.671	1.014	0.688	1.039	0.670	1.012	0.652	0.944	0.670	0.970	0.667	0.965
25	0.470	0.967	0.499	1.027	0.480	0.988	0.443	0.893	0.466	0.940	0.468	0.944
30	0.218	0.820	0.258	0.970	0.248	0.932	0.193	0.692	0.221	0.792	0.235	0.342
40	-0.359	1.419	-0.303	1.198	-0.306	1.209	-0.456	1.714	-0.382	1.436	-0.337	1.267
50	-0.853	1.269	-0.787	1.171	-0.754	1.122	-1.000	1.416	-0.887	1.256	-0.802	1.136
60	-1.350	1.274	-1.200	1.132	-1.160	1.094	-1.550	1.488	-1.370	1.315	-1.210	1.161
70	-1.595	1.387	-1.361	1.183	-1.288	1.120	-1.890	1.658	-1.692	1.484	-1.420	1.246
80	-1.521	1.603	-1.190	1.254	-1.140	1.201	-2.030	2.207	-1.630	1.772	-1.230	1.337
90	-1.355	1.422	-1.120	1.175	-1.050	1.102	-1.800	1.917	-1.505	1.603	-1.160	1.235
100	-1.272	1.339	-1.110	1.168	-1.055	1.111	-1.630	1.736	-1.340	1.427	-1.133	1.207
105	-1.070	1.126	-1.080	1.137	-1.070	1.126	-1.370	1.459	-1.230	1.310	-1.100	1.171
110	-1.050	1.105	-1.080	1.137	-1.100	1.158	-1.100	1.159	-1.120	1.180	-1.070	1.128
115	-1.030	1.084	-1.070	1.126	-1.120	1.179	-0.912	0.961	-1.070	1.128	-1.040	1.096
120	-1.030	1.084	-1.090	1.147	-1.100	1.158	-0.830	0.870	-1.000	1.048	-1.016	1.065
125	-1.010	1.063	-1.090	1.147	-1.090	1.147	-0.774	0.811	-0.997	1.045	-1.040	1.090
130	-0.986	1.038	-1.100	1.158	-1.100	1.158	-0.748	0.784	-0.978	1.025	-1.020	1.069
140	-0.998	1.041	-1.087	1.133	-1.076	1.122	-0.722	0.757	-0.924	0.969	-0.990	1.038
160	-1.005	1.019	-1.072	1.087	-1.064	1.079	-0.711	0.739	-0.919	0.955	-0.978	1.017
180	-0.990	1.004	-1.070	1.085	-1.090	1.105	-0.693	0.726	-0.878	0.920	-0.966	1.013

Re(x10^{-4})	12.5						16.7					
$\tilde{x}_g$	8		14		20		8		14		20	
Tu_b (%)	3.6		2.55		2.1		3.55		2.55		2.1	
Λ_b/D	0.147		0.190		0.233		0.158		0.202		0.246	
Λ_b/Λ_o	16.54		21.38		26.22		20.55		26.28		32.00	
Tu_c (%)	6.8		4.6		3.0		6.8		4.5		2.8	
$\tilde{x}_{min}$	1.6		2.2		2.5		1.6		2.2		2.5	
θ (deg)	C'_p	C'_p/C_p	C'_p	C'_p/C_p	C'_p	C'_p/C_p	C'_p	C'_p/C_p	C'_p	C'_p/C_p	C'_p	C'_p/C_p
0	1.000	1.000	1.000	1.000	1.000	1.000	1.000	1.000	1.000	1.000	1.000	1.000
5	0.991	0.997	0.971	0.977	0.985	0.991	0.989	0.999	0.986	0.996	0.989	0.999
10	0.930	0.978	0.899	0.945	0.935	0.983	0.934	1.002	0.920	0.987	0.917	0.984
15	0.825	0.973	0.782	0.922	0.819	0.966	0.824	0.988	0.815	0.977	0.806	0.966
20	0.633	0.911	0.588	0.846	0.640	0.921	0.637	0.927	0.623	0.907	0.613	0.892
25	0.419	0.823	0.365	0.717	0.440	0.864	0.414	0.825	0.404	0.805	0.401	0.799
30	0.155	0.538	0.101	0.351	0.188	0.653	0.146	0.516	0.139	0.491	0.131	0.463
40	-0.506	1.867	-0.561	2.070	-0.447	1.649	-0.541	2.283	-0.544	2.295	-0.537	2.266
50	-1.060	1.538	-1.109	1.610	-0.956	1.388	-1.120	1.772	-1.120	1.772	-1.090	1.725
60	-1.640	1.533	-1.650	1.542	-1.460	1.346	-1.710	1.768	-1.710	1.768	-1.680	1.737
70	-2.060	1.823	-2.008	1.777	-1.740	1.540	-2.169	2.169	-2.141	2.141	-2.080	2.080
80	-2.220	2.349	-2.077	2.198	-1.760	1.862	-2.384	2.753	-2.357	2.722	-2.220	2.564
90	-2.150	2.304	-1.868	2.002	-1.560	1.672	-2.318	2.760	-2.257	2.687	-2.050	2.440
100	-1.910	2.034	-1.708	1.819	-1.430	1.523	-2.049	2.374	-2.014	2.334	-1.890	2.190
105	-1.730	1.840	-1.497	1.593	-1.370	1.457	-1.819	2.115	-1.863	2.166	-1.680	1.953
110	-1.230	1.309	-1.286	1.368	-1.260	1.340	-1.234	1.437	-1.326	1.544	-1.220	1.420
115	-0.876	0.932	-1.075	1.144	-1.090	1.160	-0.837	0.976	-0.886	1.033	-0.919	1.071
120	-0.718	0.760	-0.865	0.915	-1.010	1.069	-0.659	0.769	-0.684	0.798	-0.788	0.919
125	-0.627	0.662	-0.820	0.866	-0.940	0.993	-0.577	0.679	-0.606	0.713	-0.713	0.839
130	-0.597	0.629	-0.774	0.816	-0.949	1.000	-0.552	0.653	-0.559	0.662	-0.684	0.809
140	-0.548	0.576	-0.757	0.796	-0.896	0.942	-0.522	0.621	-0.525	0.625	-0.664	0.790
160	-0.567	0.604	-0.756	0.805	-0.853	0.908	-0.518	0.617	-0.532	0.633	-0.658	0.783
180	-0.548	0.584	-0.711	0.757	-0.820	0.873	-0.488	0.592	-0.504	0.612	-0.619	0.751

Table A.VI.1 (continued)

$Re(x10^{-4})$	20.9					
$\tilde{x}_g$	8		14		20	
Tu_b (%)	3.5		2.5		2.05	
Λ_b/D	0.172		0.216		0.261	
Λ_b/Λ_o	25.03		31.43		37.98	
Tu_c (%)	6.7		2.5		2.5	
$\tilde{x}_{min}$	1.6		2.2		2.5	
θ (deg)	C'_p	C'_p/C_p	C'_p	C'_p/C_p	C'_p	C'_p/C_p
0	1.000	1.000	1.000	1.000	1.000	1.000
5	0.997	1.022	0.991	1.015	0.983	1.007
10	0.929	1.000	0.920	0.990	0.903	0.972
15	0.818	0.994	0.807	0.981	0.797	0.968
20	0.632	0.936	0.612	0.907	0.602	0.892
25	0.411	0.807	0.397	0.780	0.387	0.760
30	0.144	0.491	0.126	0.430	0.115	0.392
40	-0.538	2.445	-0.568	2.582	-0.569	2.586
50	-1.110	1.881	-1.140	1.932	-1.140	1.932
60	-1.737	1.917	-1.745	1.926	-1.757	1.939
70	-2.189	2.329	-2.155	2.293	-2.214	2.355
80	-2.453	3.036	-2.447	3.028	-2.439	3.019
90	-2.330	2.862	-2.307	2.834	-2.354	2.892
100	-2.042	2.521	-2.058	2.541	-2.129	2.628
105	-1.746	2.156	-1.760	2.173	-1.817	2.243
110	-1.198	1.479	-1.207	1.490	-1.246	1.538
115	-0.857	1.071	-0.863	1.079	-0.886	1.108
120	-0.632	0.799	-0.639	0.808	-0.661	0.836
125	-0.584	0.739	-0.565	0.715	-0.593	0.751
130	-0.548	0.703	-0.538	0.690	-0.567	0.727
140	-0.517	0.672	-0.510	0.663	-0.514	0.668
160	-0.525	0.670	-0.521	0.665	-0.518	0.661
180	-0.484	0.625	-0.492	0.636	-0.490	0.633

TABLE A.VI.2. TURBULENT INCIDENT FLOW

PRESSURE DISTRIBUTION CHARACTERISTICS, INCIDENT TURBULENCE CHARACTERISTICS, DRAG COEFFICIENT

$\tilde{x}_g$	Re $(x10^{-4})$	θ'_m (deg)	θ'_s (deg)	θ'_{sm} (deg)	θ'_{bs} (deg)	C'_{pm}	C'_{pm}/C_{pm}	C'_{pb}	C'_{pb}/C_{pb}	C'_{pbm}	C'_{pbm}/C_{pbm}
8	5.2	76	105	29	75	-1.620*	1.41	-0.990	1.004	0.630	3.841
	9.4	80	125	45	55	-2.030	1.78	-0.693	0.726	1.337	7.188
	12.5	80	130	50	50	-2.220	1.96	-0.548	0.584	1.642	8.754
	16.7	80	130	50	50	-2.384	2.38	-0.488	0.592	1.896	10.773
	20.9	80	130	50	50	-2.453	2.61	-0.484	0.625	1.969	11.861
14	5.2	73	95	22	85	-1.380*	1.20	-1.070	1.085	0.310	1.890
	9.4	78	120	42	60	-1.780*	1.56	-0.878	0.920	0.902	4.849
	12.5	80	128	48	52	-2.077	1.84	-0.711	0.757	1.366	7.152
	16.7	80	130	50	50	-2.357	2.36	-0.504	0.612	1.853	10.528
	20.9	80	130	50	50	-2.447	2.61	-0.492	0.636	1.955	11.777
20	5.2	70	85	15	95	-1.288	1.12	-1.090	1.105	0.198	1.207
	9.4	75	110	35	70	-1.480*	1.30	-0.966	1.013	0.514	2.763
	12.5	78	122	44	58	-1.850*	1.64	-0.820	0.873	1.030	5.393
	16.7	80	128	48	52	-2.220	2.22	-0.619	0.751	1.601	9.097
	20.9	80	130	50	50	-2.439	2.60	-0.490	0.633	1.949	11.741

$\tilde{x}_g$	Re $(x10^{-4})$	C'_{pbm}/θ'_{sm}	C'_{pbm}/θ'_s	Tu_b^2Re	Tu_c^2Re	$(\Lambda_b/\pi D)Tu_bRe^{1/2}$	C_{Dt}	C_{Dt}/C_{Df}
8	5.2	1.245	0.344	87	252	0.369	1.00	0.93
	9.4	1.703	0.613	128	441	0.497	0.68	0.64
	12.5	1.915	0.737	162	525	0.595	0.52	0.50
	16.7	2.172	0.836	210	770	0.278	0.45	0.46
	20.9	2.255	0.868	256	949	0.876	0.44	0.47
14	5.2	0.807	0.187	38	122	0.329	1.13	1.06
	9.4	1.231	0.431	63	204	0.461	0.93	0.88
	12.5	1.630	0.611	81	265	0.455	0.65	0.62
	16.7	2.123	0.817	108	344	0.669	0.46	0.48
	20.9	2.239	0.862	130	397	0.785	0.43	0.46
20	5.2	0.756	0.133	24	64	0.325	1.14	1.07
	9.4	0.841	0.268	43	96	0.463	1.03	0.97
	12.5	1.341	0.484	58	112	0.550	0.85	0.81
	16.7	1.911	0.717	74	127	0.671	0.58	0.60
	20.9	2.233	0.859	92	133	0.778	0.43	0.46

*Deduced by interpolation.

TABLE A.VI.3. SMOOTH INCIDENT FLOW

PRESSURE DISTRIBUTION CHARACTERISTICS AND DRAG COEFFICIENT

Re ($\times 10^{-4}$)	θ_m (deg)	θ_s (deg)	θ_{sm} (deg)	θ_{bs} (deg)	C_{pm}	C_{pb}	C_{pbm}	$C_{D\ell}$
5.2	70	80	10	100	-1.15	-0.986	0.164	1.07
9.4	70	80	10	100	-1.14	-0.954	0.186	1.06
12.5	70	80	10	100	-1.13	-0.939	0.191	1.05
16.7	70	80	10	100	-1.00	-0.824	0.176	0.97
20.9	70	80	10	100	-0.94	-0.774	0.166	0.93

APPENDIX A

LIST OF SYMBOLS

C_D	drag coefficient
C_p	pressure coefficient
C_{pb}	base pressure coefficient
C_{pbm}	pressure rise coefficient
C_{pm}	minimum pressure coefficient
C_{po}	stagnation pressure coefficient
C'_{pbm}/θ'_{sm}	average adverse pressure gradient
C'_{pbm}/θ'_{s}	separation coefficient
D	cylinder diameter
D/h	blockage coefficient
D/S	cylinder slenderness
d	rod diameter in turbulence generating-grid
d_w	wake width
E(n)	one-dimensional energy spectrum
h	wind-tunnel cross-section height (or width)
k	roughness height; base pressure parameter in Sect. 3.4
k/D	relative surface roughness
M	mesh of turbulence-generating grid; Mach number in Sect. 7
n	frequency
$p(\theta)$	surface static pressure
p_∞	freestream static pressure
p_b	base pressure
p_m	minimum pressure

p_o	stagnation pressure
R	cylinder radius
Re	cylinder-diameter Reynolds number
S	cylinder span; Strouhal number in Sect. 2.3
Tu	turbulence intensity
Tu_∞	freestream turbulence intensity
Tu_b	background turbulence intensity
Tu_c	critical turbulence intensity
Tu^2Re	turbulence parameter
U_∞	freestream velocity
$\overline{U}_b$	background mean velocity
u'	rms value of axial turbulent velocity
$\overline{u^2}$	mean-square value of axial turbulent velocity
u_b'	rms value of background axial turbulent velocity
$\overline{u_b^2}$	mean-square value of background axial turbulent velocity
x,y,z	Cartesian coordinates
x_g	turbulence-generating grid position
x_{min}	position of critical turbulence intensity
δ_ℓ	laminar boundary-layer thickness
θ	azimuthal (or peripheral) angle
θ_b	base point
θ_{bs}	base region angular extent
θ_m	minimum pressure angular position
θ_s	separation angle
θ_{sm}	adverse pressure gradient region angular extent

Λ	body shape factor in App. II
Λ_b	longitudinal integral scale of background turbulence
λ_0	neutral scale (or wavelength)
λ_s	Strouhal scale
μ	dynamic viscosity
ν	kinematic viscosity
ρ	density
σ	turbulence-generating grid solidity; blockage parameter in App. II
τ	blockage parameter in App. II

Superscripts

'	means 'turbulent incident flow'
*	means 'blockage corrected'
~	means 'dimensionless'
-	time averaged

Subscripts

ℓ	laminar
M	Maskell blockage correction method
min	minimum
t	turbulent

The International System (SI) of measurement was used throughout this work. Conversion from SI units to U.S. customary units was carried out to approximately two to three significant digits.

1. Report No.	2. Government Accession No.	3. Recipient's Catalog No.
NASA CR-3622		

4. Title and Subtitle	5. Report Date
TURBULENCE EFFECT ON CROSSFLOW AROUND A CIRCULAR CYLINDER AT SUBCRITICAL REYNOLDS NUMBERS	November 1982
	6. Performing Organization Code

7. Author(s)	8. Performing Organization Report No.
Willy Z. Sadeh and Daniel B. Saharon	CER 81-82 WZS-DBS51
	10. Work Unit No.

9. Performing Organization Name and Address	11. Contract or Grant No.
Colorado State University Fluid Mechanics and Wind Engineering Program Department of Civil Engineering Fort Collins, Colorado 80523	NSG-3127
	13. Type of Report and Period Covered
12. Sponsoring Agency Name and Address	Contractor Report
National Aeronautics and Space Administration Washington, D. C. 20546	14. Sponsoring Agency Code 505-36-12 (E-1341)

15. Supplementary Notes
Final report. Project Manager, Peter M. Sockol, Fluid Mechanics and Acoustics Division, NASA Lewis Research Center, Cleveland, Ohio 44135.

16. Abstract

An investigation of the effect of freestream turbulence on the flow around a smooth circular cylinder at subcritical Reynolds numbers from 5.2×10^4 to 2.09×10^5 was conducted. Measurements show that the interaction of incident turbulence with the initial laminar boundary layer: (1) modifies the characteristics of the mean surface pressure distribution; (2) induces an aft shift in the separation point ranging from 5 to 50^o beyond the laminar separation angle of 80^o; and, (3) reduces the mean drag coefficient to values between 97 and 46% of its nearly constant laminar counterpart. The extent of these changes depends on the particular Reynolds number-background turbulence combination. These results demonstrate that a boundary-layer flow similar to that found in critical, supercritical and/or transcritical flow regimes is induced by turbulence at subcritical Reynolds numbers and, hence, the effect of turbulence is equivalent to an effective increase in the Reynolds number. The change in the nature and properties of the boundary layer in the subcritical regime, consequent upon the penetration of turbulence into it, is in agreement with the model proposed by the vorticity-amplification theory.

17. Key Words (Suggested by Author(s))	18. Distribution Statement
Stagnation flow; Turbulent flow about a bluff body; Vorticity amplification; Turbulence amplification; Turbulent boundary layer; Laminar boundary layer; Flow visualization	Unclassified - unlimited STAR Category 34

19. Security Classif. (of this report)	20. Security Classif. (of this page)	21. No. of Pages	22. Price*
Unclassified	Unclassified	152	A08

* For sale by the National Technical Information Service, Springfield, Virginia 22161

NASA-Langley, 1982